A CONTRIBUTION TO THE UNDERSTANDING OF COMPRESSION AFTER IMPACT OF COMPOSITE LAMINATES

Yi Liv

Doctoral Thesis

A contribution to the understanding of compression after impact of composite laminates

Yi Liv

2017

Universitat de Girona

Doctoral Thesis

A contribution to the understanding of compression after impact of composite laminates

Yi Liv

2017

Doctoral Programme in Technology

Supervised by: Dr. Josep Costa Balanzat
Dr. Emilio Vicente González Juan

Thesis submitted to the University of Girona in partial fulfillment for the degree of Doctor of Philosophy

Yi Liv

A contribution to the understanding of compression after impact of composite laminates

Doctoral Thesis, 2017

Supervisors: Dr. Josep Costa Balanzat and Dr. Emilio Vicente González Juan

University of Girona

AMADE Research Group

Escola Politècnica Superior

Department of Mechanical Engineering and Industrial Construction

Carrer Universitat de Girona, 4

17003, Girona

Acknowledgment

I would like to acknowledge the Generalitat de Catalunya for the FI-DGR pre-doctoral grant (2015FI-B1 00144) and the Spanish Ministerio de Ciencia e Innovación the financial support of under the project MAT2015-69491-C3-1-R (MINECO/FEDER, UE).

I would like to express my sincere appreciation to my two supervisors, Prof. Josep Costa and Dr. Emilio González, who have compassionately and tirelessly guided and kept me on the track of my academic roller coaster. Their altruistic supervision has a deep touch on me and helps me realize that developing characters is part of the PhD. I owe a very deep gratitude to Josep who has skillfully and patiently taught me to be concise and brief in scientific communication, not to mention many other kinds of support.

I would also extend my gratitude to some senior researchers of AMADE: Dr. Jordi Renart for his fatigueless guidance through my master thesis and tirelessly encouraging me to improve it for publication; Dr. Marta Baena who took the courage I did not have to tell Josep on my behalf that I had had the urge to do a PhD; Dr. Albert Turon and Pere Maimí who never turn their back to me whenever I need help.

Over the entire course of my PhD, there are many other individuals to whom I am really grateful for their kindest support: Gerard Guillamet, Albert Soto, Adriá Otega, Jordi LLobet, Juan David, Aravind, and Adria Quintana who have always kindly shared and discussed about countless things; Daniel Piedrafita, Ivan Recio, Junior Batista, and Tiina who have helped me accomplish my experimental test campaign at the AMADE laboratory; Magdalena for an unforgettable stay with her family in Malloca; Santi for his great contribution to μCT images; Laura for a beautiful lunch at her family's; and the rest of AMADE members for creating a very comfortable and enjoyable atmosphere for everyone.

My deepest gratitude goes to the compassion and lovingkindness of my two stepsisters and my father who–despite their misfortune of not being able to finish our country's elementary school–have never discouraged me on my journey to fulfill my thirst for knowledge, and of my late stepmother who had to leave this beautiful world. Above all, words cannot precisely express my gratitude for gratitude is better felt!

Publications

Peer-reviewed journals

1. Yi Liv, G. Guillamet, J. Costa, E.V. González, L. Marín, J.A. Mayugo, ”Experimental study into compression after impact strength of laminates with conventional and nonconventional ply orientations,” *Composites Part B: Engineering*, Vol. 126, pp. 133–142, 2017.

   ISSN: 1359-8368, Impact factor: 4.727, ranked 2/25 in category *Materials Science, Composites*, Q1.[1]

Conference proceedings

1. Yi Liv, G. Guillamet, E.V. González, J.A. Mayugo, and J. Costa, ”Experimental study of compression after impact strength of tailored non-conventional laminates,” *7th International Conference on Composites Testing and Model Identification (CompTest 2015)*, Madrid, 8-10 April 2015.

2. Y. Liv, J. Renart, J. Costa, J. A. Mayugo, ”Experimental determination of R-curve of unidirectional carbon-fibre reinforced composite laminates based on end-notched flexure test,” *XIII Meeting of the group of polymers on the Spanish royal chemistry and royal physics societies (GEP 2014)*, Girona, Spain, 7-10 September 2014.

3. G. Guillamet, Y. Liv, A. Turon, L. Marín, J. Costa, J.A. Mayugo, ”Design of non-conventional CFRP laminates for improved damage resistance and damage tolerance,” *16th European Conference on Composite Materials, ECCM 2014*, Seville, Spain, 22-26 June 2014.

[1] According to the *2016 Journal Citation Reports (JCR)*

Manuscripts under preparation

1. Yi Liv, J. Renart, J. Costa, E.V. González, ”A critical review on end-notched exure (ENF) test for determining mode II fracture toughness.”

2. Yi Liv, S.M. García-Rodríguez, J. Costa, E.V. González, J.A. Mayugo,”Damage development of laminates with conventional and nonconventional ply orientations under quasi-static indentation.”

3. Yi Liv, E.V. González, J. Costa, J.A. Mayugo, ”Numerical study of compressive strength of laminates with one embedded delamination: Effects of through-the-thickness position.”

Universitat de Girona

Dr. Josep Costa Balanzat, Full Prof. at the University of Girona

and

Dr. Emilio Vicente González Juan, Lecturer at the University of Girona

hereby CERTIFY that:

The thesis entitled *A contribution to the understanding of compression after impact of composite laminates*, submitted for the degree of Doctor of Philosophy by Yi Liv, was conducted under our supervision.

Dr. Josep Costa Balanzat
Full Prof. at University of Girona

Dr. Emilio Vicente González Juan
Lecturer at University of Girona

Girona, September 25, 2017

Nomenclature

Symbols

F_d	Delamination threshold load
E_{dis}	Dissipated energy
E_{app}	Applied energy
A_{pro}	Projected delamination area
F_{max}	Peak/maximum impact load
F_{bk}^{s}	Sublaminate buckling load
F_{bk}	Buckling load
G_{Ic}	Mode I interlaminar fracture toughness
G_{IIc}	Mode II interlaminar fracture toughness
δ_{ind}	Indentation depth
σ_{CAI}	Compression after impact strength

Acronyms

LBA	Laminate/layup used as baseline
LTP	Laminate/layup made of thick-ply (blocked-ply or ply clustering)
LNC	Laminate/layup made of nonconventional ply orientations
MMA	Mismatch angle (difference in the fibre orientations of adjacent plies)
BVID	Barely visible impact damage
LVI	Low velocity impact
QSI	Quasi-static indentation
DR	Damage resistance
DT	Damage tolerance
FE	Finite element
CAI	Compression after impact
ERR	Energy release rate
CZM	Cohesive zone model
VCCT	Virtual crack closure technique
CFRP	Carbon fibre-reinforced polymer
IDM	Impact damage morphology
μCT	Micro-focused X-ray computed tomography

List of Figures

List of Tables

Contents

Abstract

The threat of impact on laminated composite structures has been a serious concern in the aerospace industry and scientific community because the compression load-carrying capacity of the structures, namely Compression After Impact (CAI) strength, is severely impaired. The CAI strength reduction can reach as high as 60% for a typical advanced composite made of unidirectional carbon fibre laminae.

The starting hypothesis of this thesis is that it is possible to improve the CAI strength by properly designing their layup, known as stacking sequence. Due to the complex impact damage morphology, little is known about how to tailor such a stacking sequence. Contributing to this research line is the single aim of this PhD thesis, which has the following pillar objectives.

First, the study begins with the experimental validation of the hypothesis that the stacking sequence of a nonconventional laminate can be tailored to predetermine the through-the-thickness location of delaminations created during a low velocity impact, and finding out whether the consequent CAI strength can be improved in comparison to conventional laminates.

Second, the damage development in these laminates is experimentally studied with quasi-static indentation tests, C-Scan and X-ray computed tomography. The results elucidate the sequence of damage mechanisms and provide a more detailed morphology than that observed in impact tests.

Finally, a numerical study is conducted on three groups of layups containing an embedded circular delamination. The objective is to examine the sensitivity of compressive strength to delamination size, location, and loading directions. This investigation has resulted in: (i) a reasonable explanation of the differences in CAI strength of conventional and nonconconventional laminates observed in the first study, and (ii) suggestions for the design of more damage tolerant conventional and nonconventional layups.

Resum

Els impactes de baixa velocitat en estructures de materials compostos representen una greu amenaça per a la indústria aeroespacial i un tema d'interès per a la comunitat científica pel fet que deterioren la resistència a compressió (CAI). La reducció de resistència pot arribar fins al 60% per a un material compost avançat típic de làmines unidireccionals de fibra de carboni.

La hipòtesi que dóna peu a aquesta tesi és que és possible millorar la resistència a compressió després d'impacte dissenyant adequadament la seqüència d'apilament. A causa de la complexa morfologia del dany per impacte, se sap poc sobre com definir tal seqüència. Contribuir a aquesta línia d'investigació és l'únic objectiu d'aquesta tesi doctoral, el desenvolupament de la qual ha implicat perseguir els següents objectius.

L'estudi comença amb la validació experimental de la hipòtesi que la seqüència d'apilament d'un laminat no-convencional pot definir-se de tal manera que es predetermini la ubicació a través del gruix de les delaminaciones creades durant un impacte de baixa velocitat, i, al seu torn, esbrinar si la consegüent resistència a compressió (CAI) pot millorar-se en comparació amb la dels laminats convencionals.

A continuació s'aborda un estudi experimental de la seqüència de dany en els laminats anteriors, mitjançant assajos d'indentació quasi-estàtica, C-Scan i tomografia computeritzada de raigs X. Els resultats de l'estudi diluciden la seqüència de mecanismes de dany i proporcionen una descripció de la seva morfologia més detallada que l'observada en les proves d'impacte.

Finalment, es realitza un estudi numèric sobre tres grups de laminats que contenen una delaminació circular. L'objectiu és examinar la sensibilitat de la resistència a compressió a la ubicació de la delaminació i la direcció de càrrega. Aquesta investigació ha resultat en: (i) una explicació raonada de les diferències en la resistència a compressió (CAI) dels laminats convencionals i no-convencionals observats en el primer estudi, i (ii) la possibilitat de suggerir criteris per al disseny de laminats convencionals i no-convencionals amb un comportament millorat.

Resumen

Los impactos de baja velocidad en estructuras de materiales compuestos representan una grave amenaza para la industria aeroespacial y un tema de interés para la comunidad científica debido a que deterioran la resistencia a compresión (CAI). La reducción de resistencia puede llegar hasta el 60% para un material compuesto avanzado típico de láminas unidireccionales de fibra de carbono.

La hipótesis que da pie a esta tesis es que es posible mejorar la resistencia a compresión después de impacto diseñando adecuadamente la secuencia de apilamiento. Debido a la compleja morfología del daño por impacto, se sabe poco sobre cómo definir tal secuencia. Contribuir a esta línea de investigación es el único objetivo de esta tesis doctoral, cuyo desarrollo ha implicado perseguir los siguientes objetivos.

El estudio comienza con la validación experimental de la hipótesis de que la secuencia de apilamiento de un laminado no-convencional puede definirse de tal manera que se predetermine la ubicación a través del espesor de las delaminaciones creadas durante un impacto de baja velocidad, y, a su vez, averiguar si la consiguiente resistencia a compresión (CAI) puede mejorarse en comparación con la de los laminados convencionales.

A continuación se aborda un estudio experimental de la secuencia de daño en los laminados anteriores, mediante ensayos de indentación cuasi-estática, C-Scan y tomografía computarizada de rayos X. Los resultados del estudio dilucidan la secuencia de mecanismos de daño y proporcionan una descripción de su morfología más detallada que la observada en las pruebas de impacto.

Por último, se realiza un estudio numérico sobre tres grupos de laminados que contienen una delaminación circular. El objetivo es examinar la sensibilidad de la resistencia a compresión al tamaño de la delaminación, ubicación y dirección de carga. Esta investigación ha resultado en: (i) una explicación razonada de las diferencias en la resistencia a compresión (CAI) de los laminados convencionales y no-convencionales observados en el primer estudio, y (ii) la posibilidad de sugerir criterios para el diseño de laminados convencionales y no-convencionales con un comportamiento mejorado.

Part I

Introduction and Literature Review

1 Introduction

> *Scientific results that aren't reported might as well not exist. They're like the sound of one hand clapping. For scientists, communication isn't only a responsibility, it's our chief pleasure.*
>
> **— Robert O. Becker, 1923-2008**

1.1 Background

The merits of laminated composites over traditional metals are high specific stiffness and strength, good corrosion resistance, long fatigue life, and freedom to tailor stiffness and strength according to preferred loading directions. These advantages have made them well suited for the aerospace industry, and increasingly attractive for other areas such as automotive, sports equipment and civil engineering. Unfortunately, they are susceptible to damage caused by Low Velocity Impact (LVI), and exhibit a severe reduction in terms of the Compression After Impact (CAI) strength. For composite laminates based on carbon/epoxy unidirectional prepreg tapes, the LVI damage modes comprise of matrix cracks, delamination and eventually fibre breakage for relatively high impact energy [1–6]. Impact-induced delaminations are generally considered to be the most critical damage mode as they are the main cause of the CAI strength reduction [7–10]. The magnitude of the strength reduction can reach as high as 60% in a typical aerospace fibre-resin system [11]. The strength reduction may become even higher, considering the effect of environmental factors such as moisture on the composite material properties, e.g. [12–14].

1.2 Motivation

The quest for improved CAI strength of laminated composites in the context of the stacking sequence design has resulted in dispersed ply laminates [15–18]. A dispersed ply laminate, unlike its conventional counterparts, has ply orientations not limited to the conventional 0, ± 45 and 90° orientations, and hereafter is referred to as a nonconventional laminate (LNC) for our convenience. The experimental study of two LNCs by Lopes et al. [15] suggested that more efforts should be put to control

the size of impact-induced delaminations as well as their through-the-thickness locations.

Sebaey et al. [18] explored the possibility to enhance the CAI strength by controlling the mistmach angle (MMA) between two adjacent plies. They devised the ply sequences of two LNCs: one with small MMAs between 10 and 30°, and the other between 55 and 80°. Their experimental results showed that the CAI strength of the LNC with small MMAs were superior when compared to those of the baseline laminate, and of the LNC with large MMAs. The enhancement of the CAI strength with the LNC could reach up to 30% in some cases. The CAI improvement in the small-MMA NLC was attributed to the thicker sublaminates which increase the buckling load and thus its residual strength. Fewer thicker sublaminates in the small-MMA NLC were the consequence of a smaller number of delaminations being controlled by small MMAs.

Indeed, controlling MMAs is not the only way to control the thickness of the impact-induced sublaminates. Blocking plies to form thicker plies has also been reported to reduce the number of delaminations and thus form thicker sublaminates [19–21]. Nonetheless, whether the CAI strength of the thick-ply laminate is in fact reduced or not remains unclear when these experimental results are closely examined.

During their service life, composite aircraft structures are inevitably exposed to hygrothermal environment that can degrade the composite material properties. Whilst there have been concerns over the influence of temperature and moisture on the general performance of laminated composites, little is known about the influence of either of the two environmental factors. According to a brief literature survey (see Section 2.7), no information is available regarding a comparative study of the influence of moisture alone on the CAI strength of different laminate layups, i.e. those made of thick-plies and nonconventional orientations. This highlights the need to produce experimental data on this topic.

In summary, there are possibilities to be explored in order to enhance the CAI strength by tailoring nonconventional ply sequences, issues to be reexamined regarding the ply-thickness effect, scopes for conducting experimental study into the moisture influence on the CAI strength, and the influence of the through-the-thickness location of a single delamination on the laminate compressive failure load. Furthermore, understanding the damage mechanisms taking place during an LVI event from the initiation point to propagation is crucial to achieve composite laminates with higher CAI strength. This is because, as will be elaborated in Section 2.3, impact damage morphology (IDM) and the CAI strength are strongly linked.

1.3 Objectives

Following the gaps identified in the preceding Section 1.2, the objectives of this thesis can be summarised as follows:

1. Validate the hypothesis that the ply sequence of an LNC can be tailored to predetermine the through-the-thickness location of impact-induced delaminations, and that its CAI strength is expected to be improved.

2. Investigate the damage occurrence focusing on the indentation displacements corresponding to laminate damage initiation and delaminations propagation.

3. Study the influence of the through-the-thickness location of an embedded delamination on the failure load of conventional and nonconventional laminates.

4. Revisit the effect of blocking plies on the laminate response under out-of-plane and CAI loading.

5. Examine the influence of moisture on the laminate response under out-of-plane and CAI loading.

The five preceding objectives are primary in this thesis with regards to its single aim to contribute to the improvement of the CAI strength through layup design. The first objective was stimulated by the possibility to enhance the CAI strength as demonstrated in the past studies [15–18]. The difference between the approach considered in this thesis and those in previous studies lies in the predetermination of the locations of small and large MMAs through the thickness direction with the aim to control the delamination size. The second objective was motivated by the experimental observation that there exists an inextricable link between IDM and the CAI strength. Therefore, it is essential to understand how different damage mechanisms initiate and propagate in different layups so that IDM can be better controlled and its relationship with the CAI strength can be studied. The third objective stems from the aim to understand the effect of the through-the-thickness location of a single delamination on the compressive failure load, i.e. the maximum load-carrying capacity. The purpose of revisiting the effect of ply thickness was to clarify the influence of blocking plies on the CAI strength. The motivation behind investigating moisture effects was due to the concerns over the environmental factors affecting the CAI strength, and the scarcity of the experimental data in the literature (see Section 2.7).

It is worth remarking that the pronounced improvement of the CAI strength in the LNCs, as reported in [17, 18], is very promising because it involves only layup design. This is an approach that can be considered to be very cost-effective and simple from the manufacturing standpoint. The method has resulted in the enhancement level

which has even surpassed many others based on a so-called material design approach (see Section 2.6 of Chapter 2).

1.4 Thesis Overview

In what follows, the thesis begins with the literature review in **Chapter 2**, giving credits to the efforts by many researchers to bring insights into the field of low velocity impact, compression after impact and compressive behaviour of laminates with artificial damage. **Chapter 3** describes the methods and materials used to conduct the study, whereas the results and discussions that fulfill the objectives listed in Section 1.3 are provided in **Chapters 4, 5 and 6**. Finally, **Chapters 7** and **8** present the conclusions and recommendations for future work, respectively.

Literature review

2

> *If I have seen further than others, it is by standing upon the shoulders of giants.*
>
> **— Isaac Newton, 1643-1727**

2.1 Impact damage: modes and morphology

Impact damage modes and morphology are affected various factors. Unless otherwise specified this review focuses on the unidirectional prepreg-based laminated composites under low velocity impact.

Post-impact observations have documented the following damage modes: matrix crack, delamination, fibre fracture/breakage, permanent indentation, matrix-fibre interface debonding, perforation. The first four failure modes are commonly observed in low velocity/energy impact. Fig. 2.1 shows the three most commonly observed types of impact-induced damage. In an attempt to capture the full spectrum of impact-induced damage, researchers have made use of several techniques: X-ray radiography, ultrasonic C-Scan, thermal deply, optical microscopy, scanning electron microscopy, ultrasonic infrared thermography, and computed tomography and acoustic emission [22–29].

Particular limitations are inherent in these damage inspection methods. X-ray radiography is used for observing matrix cracking and delamination, but does not clearly show the location of fibre fracture. The C-scan is normally used to locate the area of damage and obtain an integrated picture of the damage (delaminations in particular), but cannot distinguish between the various fracture modes incurred. Optical microscopy, Scanning electron microscopy and thermal deplying yield the greatest information about the impact process, but they are destructive damage detection techniques.

Among the aforementioned inspection techniques, computed tomography has recently gained a lot of attention. Three different computed tomography techniques have recently been exploited to inspect impact damage [30]: microfocus laboratory computed tomography (μCT), synchrotron radiation computed tomography (SRCT), and synchrotron radiation computed laminography (SRCL). For more information related to specific technicalities of various nondestructive inspection methods com-

monly used for detecting in-situ defects of composite structures, the review article of Garnier et al. [31] is recommended.

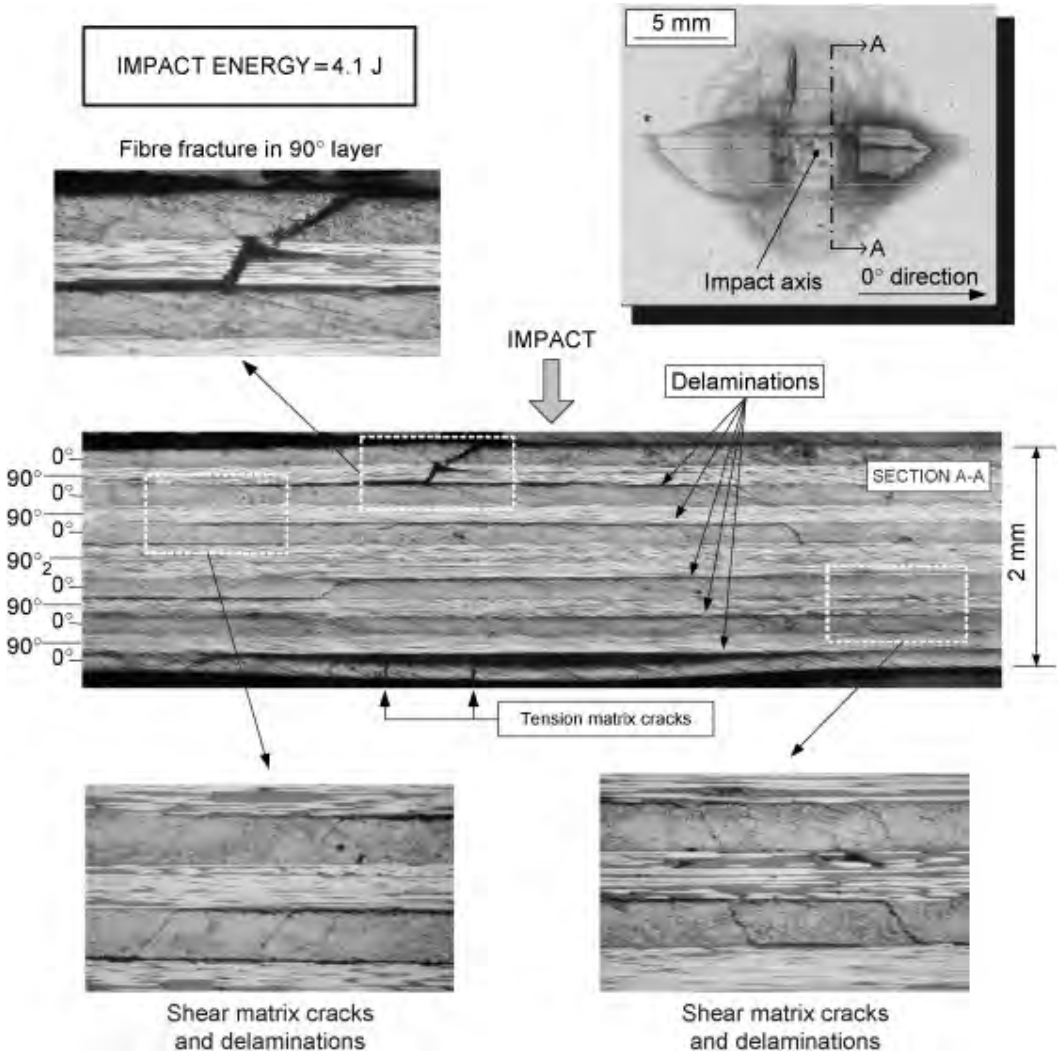

Fig. 2.1: Micrographs of impact damage in $[0/90]_{3s}$ laminate [32].

2.1.1 Matrix cracks

Two types of matrix cracks have been reported in the literature: shear stress-induced matrix cracks and tensile stress-induced matrix cracks (Fig. 2.2a). The former appear within plies near the front/impacted face and orientate approximately $45°$ with respect to the through-the-thickness direction of laminates [34]. The latter appears within plies near the back/non-impacted face due to high local tensile bending, and orientate vertically [35].

Both forms of cracks distribute through the thickness of laminates and together form a cone-shape morphology in which little damage is observed, and hereafter is referred to as undamaged cone (Fig. 2.2a). Depending on the laminate thickness,

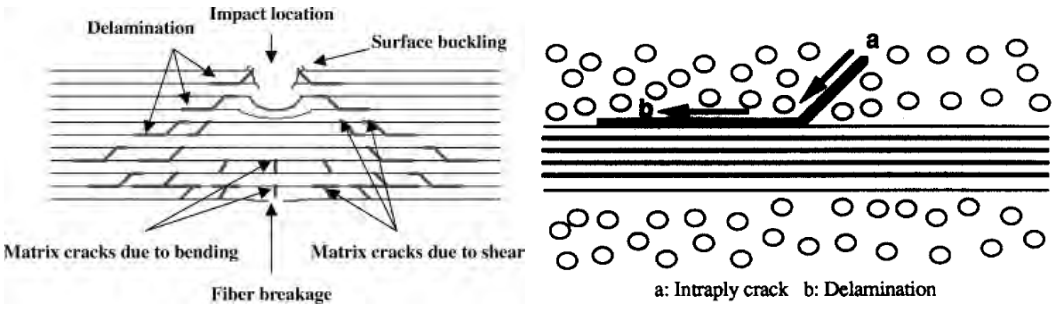

(a) Impact damage modes **(b)** Matrix crack-induced delamination

Fig. 2.2: (a) Cross-sectional schematic showing typical impact damage modes and morphology for laminate composites [33]; (b) schematic illustrating a matrix crack reaching at the interlaminar interface, deviating and giving rise to delamination [24].

this morphology of matrix cracks appears in two forms: pine tree for thick laminates (Fig. 2.3 left), and reversed pine tree for thin ones (Fig. 2.3 right). Such distribution patterns have been associated with Hertzian's contact stresses exerted upon the laminate by the impactor [36].

A matrix crack may occur in form of either cracking through the matrix itself or debonding of the fibre from the matrix [37]. Talreja [38] noted that it is difficult to know whether fiber/matrix debonding occurs by itself, or is triggered by cavitation-induced brittle failure of the matrix close to the fiber surface. However, Asp et al. [39, 40] suggested strongly that the latter is the case at least for the three epoxies examined because cavitation-induced cracks occurs earlier than the matrix yielding. More interestingly, the authors demonstrated that increasing the thickness of the interphase layer, and the Poisson's ratio of the interphases could delay the strain that causes this failure.

Matrix cracking has been regarded as the first impact-induced damage mode [36]. Matrix cracks occur only within the intralaminar regions and extend along the fibre direction, and does not dramatically affect the bending stiffness of the test coupon [41]. However, Wagih et al. [5] recently conducted an experimental study demonstrating that matrix cracking could cause load drop once the delamination threshold load was reached, and thus contributed to a pronounced loss of the laminate bending stiffness.

2.1.2 Delamination

Delamination results from the damage of interface between two adjacent laminae of different fibre orientations. This failure is one of the most critical damage modes under low velocity impact, for it is internal and thus undetectable by visual inspection. More importantly, delaminations result in projected delamination areas that have been correlated with the reduction in compression after impact (CAI) strength for

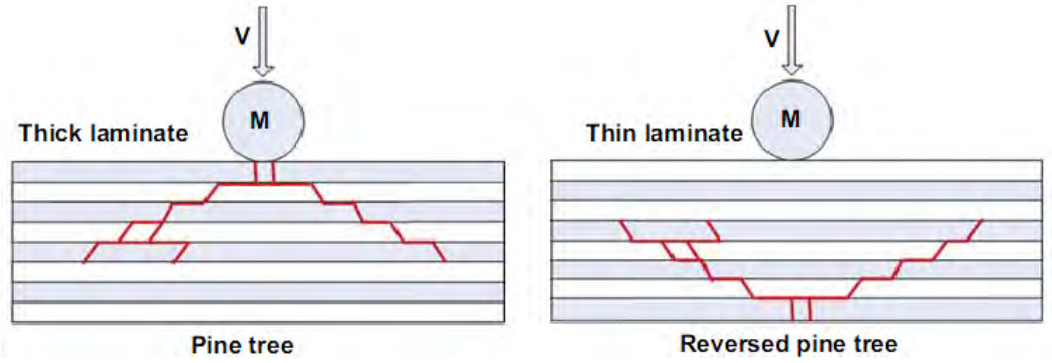

Fig. 2.3: Through-the-thickness distribution of matrix cracks, adapted from [42]. In thick laminates, high localized contact stresses cause matrix cracks on the impacted surface of the laminate. Damage progresses downward and makes a pine-tree pattern. For thin laminates, due to bending stresses, matrix cracking starts in the lowest layer, and intra-ply cracks and interface delaminations propagate from the lowest surface up toward the impacted surface, giving a reverse pine-tree pattern.

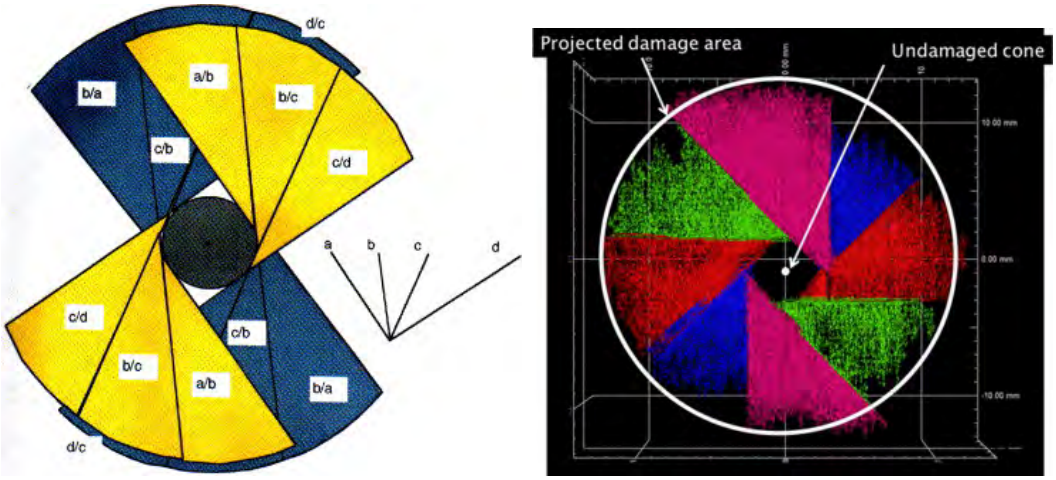

(a) General symmetric layup **(b)** Quasi-isotropic layup $[45/0/\text{-}45/90]_{3S}$

Fig. 2.4: In-plane projected delamination morphology for a symmetric laminate (...a/b/c/d//d/c/b/a...) proposed by Renault 1994, as cited in [43] (a), and as observed through the micro-focus computed tomography in [10].

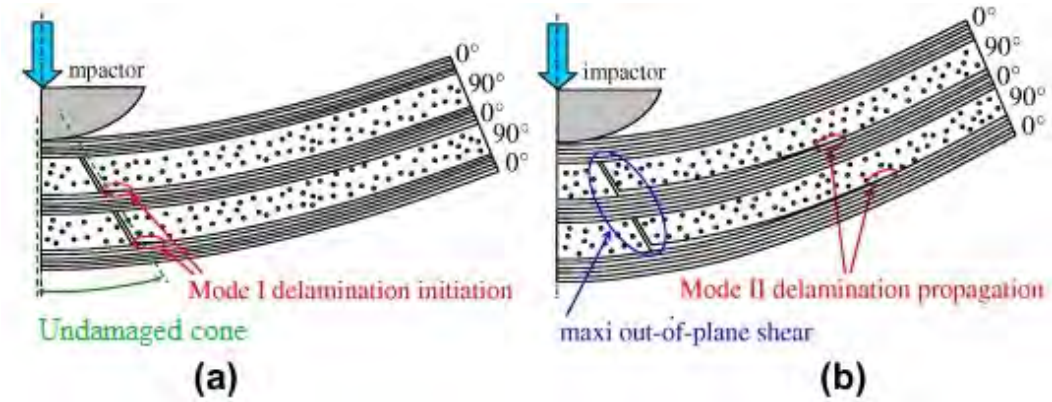

Fig. 2.5: Schematic illustrating delamination initiation in mode I (a) and propagation in mode II (b) [44].

a given layup and/or composite system [45]. In delaminated regions, the transfer of loads between adjacent plies is inhibited, thus severe reductions in strength and stiffness of the laminate are anticipated [46]. As the impact-induced delaminations are known to impair the compressive strength, past studies have made a lot of efforts to gain insights into this failure.

Hong and Liu [47] found the delamination extent on each interface to be correlated with the mismatch of bending stiffness, which is directly derived from the mismatch angle (MMA) in fibre orientations of two adjacent laminae. Using the de-ply technique, Hitchen and Kemp [48] reported that delaminations occurred at almost every interface with non-zero MMA. They also observed that the elongation of each delamination tends to be parallel to the fibre direction of the lower ply i.e. ply locating further from the impacted face. Fig. 2.4 shows the representative in-plane projected delamination morphology, typically reported in literature [10, 43]. The 2D projection of Fig. 2.1.2 was indeed inferred from ultrasonic C-Scan images where Fig. 2.4b was obtained X-ray computed tomography. Interestingly, both studies reported the presence of the undamaged cone due to high compressive stress under the impact zone. The peanut-shaped and 45° segment delaminations are the most commonly reported delamination shapes. Indeed, this is often the case of conventional layups of constant MMA of 45° or 90.

It is widely accepted that delamination is initiated by matrix cracking, and the explanation is as follows. Once a transverse matrix crack in a ply reaches the interlaminar interfaces of non-zero MMA, it is arrested by the fibres in its neighbouring plies and consequently deviates into the interlaminar interface (Fig. 2.2a), giving rise to delamination at that interface [24, 49]. Some past studies [44, 50] demonstrated that mode I fracture dominates during the initiation of the delamination whereas mode II fracture does during the propagation.

2.1.3 Fibre breakage

Under impact or quasi-static indentation loading, fibre breakage generally occurs much later than matrix cracking and delamination. Under the impacted site, fibre fracture may be seen due to locally high stresses and indentation effects (mainly governed by shear forces) and on the non-impacted face due to high bending stresses [35]. It was noted that fibre failure in thin laminates generally affects more plies than in thick laminates, indicating the importance of membrane stresses in formation of fibre fracture [51].

2.1.4 Permanent indentation

Right under the impacted location, impactor foot print results in permanent indentation, usually visible on the impacted face. Due to material relaxation, indentation gradually decreases over time [52]. This may be the reason why standard test methods recommend the indentation depth be measured shortly after the impact test.

According to Petit et al. [53], the indentation depth seems to be a good indicator of CAI strength in the aerospace industrial context. In addition, its measurement allows the relationship between the dent depth and the damaged area to be established [54], which is practical for maintenance routines of aerospace structures. In the field of aeronautics, it has been demonstrated that a permanent indentation between 0.25 and 0.5 mm is detectable during detailed visual inspection with a probability greater than 99% [44].

2.2 Compression after impact

A review of research in the area of damage tolerance critically exposes the need to identify basic damage mechanisms–as well as any additional contribution to damage tolerance–in order to develop more damage-tolerant materials and structures [24]. On the other hand, understanding the sequence of these damage events leading to ultimate failure helps develop not only more damage tolerant composite systems and structures but also more reliable numerical and analytical models to predict the progressive structural failures.

In light of the important implication of insights into CAI damage mechanisms, researchers have tried various techniques to instrument CAI to monitor in real time the response of the impacted laminate. Placing LVDT sensors on the impact locations of both impacted and unimpacted faces is a commonly-used method to characterize local buckling modes (Fig. 2.6). Some research teams [9, 55–58] have used 3D digital image correlation (DIC). With DIC, researchers [55, 56] were able to detect singularities of the strain field and impact-induced crack advances on both sides of the impacted specimen. Kim et al. [55] were even able to obtain a fairly good estimate of the stiffness reduction in the damaged area based on the assumption of linear through-thickness displacement distribution. Rivallant et al. [9] exploited DIC-based data to validate their numerical model.

Acoustic emission (AE) has recently emerged as another alternative for instrumenting CAI [59–61]. It is a promising method that can possibly characterize various failure modes. Arumugam et al. [60] suggested five ranges of peak frequency content such as 80–130, 155–170, 170–220, and 250–350 kHz that may be possibly related to the

matrix cracking, delamination, fiber–matrix debonding and fiber microbuckling/fiber failure damage modes, respectively.

2.2.1 Failure mechanisms

Under CAI loading, different failure mechanisms have been reported to be involved in the process that leads to the ultimate failure: local buckling of sublaminates, and propagation of impact-induced matrix cracks, delaminations, and fibre breakage. Nonetheless, whatever failure mechanisms operate in the failure process, care must be taken to ensure that the test coupons fail due to compression, rather than coupon buckling, so that the CAI data is valid and can used for damage tolerance design purpose.

According to Sanchez et al. [62], for the compression failure to occur, a CAI test must be carried out in a device that avoids global buckling of the impacted specimens, so that failure comes as the delamination progresses with the local buckling of the sublaminates produced in impact. The concept of failure agrees with the buckling modes suggested in earlier studies [49, 63].

Reis and Freita [49] studied the damage growth under the CAI loading, and suggested three possible local buckling modes (see Fig. 2.6). Referring to the figure, the authors also reported that more than 50% and about 35% of their specimens failed under models (a) and (b), respectively. They attributed the failure according to model (a) to the permanent indentation created on the impacted face. A subsequent study of the same authors [63] reported only models (a) and (b), and concluded that these two local failure mechanisms are influenced more by the delamination area than by the stacking sequence.

Experimentally, delamination propagation under CAI loading can be observed based on ex-situ approaches such as C-Scanning [49, 63] and cross-sectional observation using SEM or X-ray computed tomography [10]. Another way to observe this damage mode is the virtual testing [9, 64, 65]. Using C-Scan after CAI tests, Feitas and Reis [63] reported that impact-induced delaminations at all interfaces grow in the width and length directions of the test coupons. On the contrary, the experimental investigation into the delamination growth near failure by Bull et al. [10] revealed that delamination growth does not occur outside the projected delamination envelope. As cited by [43], an earlier study also observed the limited growth of impact-induced delaminations at almost failure level (Fig. 2.9). As already mentioned, the observation of delamination growth in [63] was made postmortem using C-Scan, thus the evolution of delamination propagation could not be captured as in the interrupted CAI tests of [10, 43].

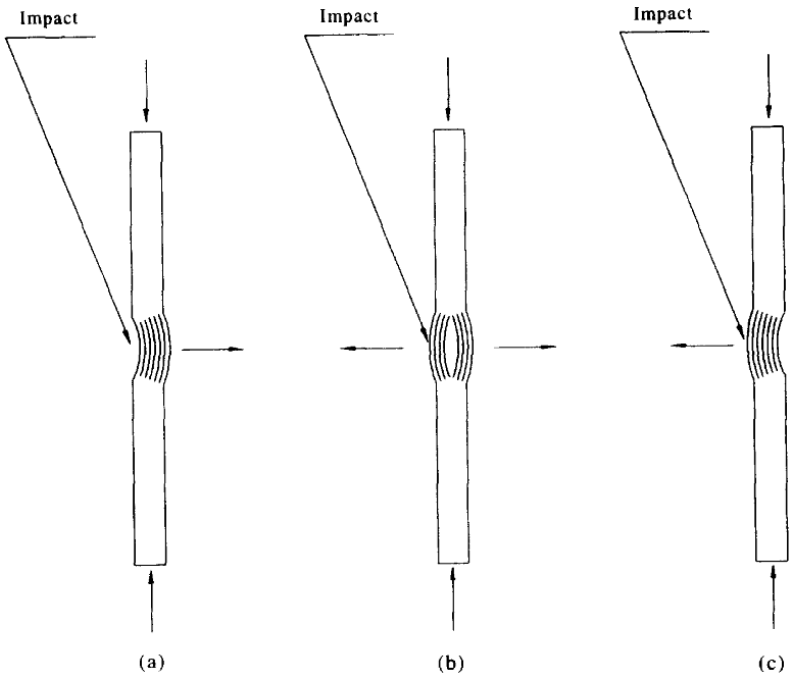

Fig. 2.6: Delamination buckling models: (a) both impacted and unimpacted surfaces move in the direction of impact displacement, (b) both impacted and unimpacted surfaces move in the opposite directions causing the opening sublaminates, and (c) opposite of model (a), take from [49].

Fibre fracture mode has been reported to occur in the investigations that exploited different instrumentation techniques such as 3D DIC [9, 56], non-destructive X-ray radiography [66], micro-focused X-ray tomography [10], or acoustic emission [59, 60]. The evidence of fibre fracture propagation was clearly observed in two studies [10, 56]. Fig. 2.7 shows the propagation starting from the tips of the impact-induced cracks in the 0°-plies.

Last but not least, the evolution of intralaminar matrix damage is possible only through FE analysis. Tan et al. [65] reported that this damage mode initiated from the two outer edges due to free-edge effects and propagated towards the impacted zone, see Fig. 2.8.

2.2.2 Failure sequences

There is still a lot to do to understand the sequence of failure modes that leads to the final failure although the CAI strength has been recognized as one of the most important parameters in selecting and/or developing composite systems for impact-threat applications. This failure sequence is still under the quest because underlying the process is the complex interaction between different failure mechanisms resulted from both material and structural properties of laminated composites.

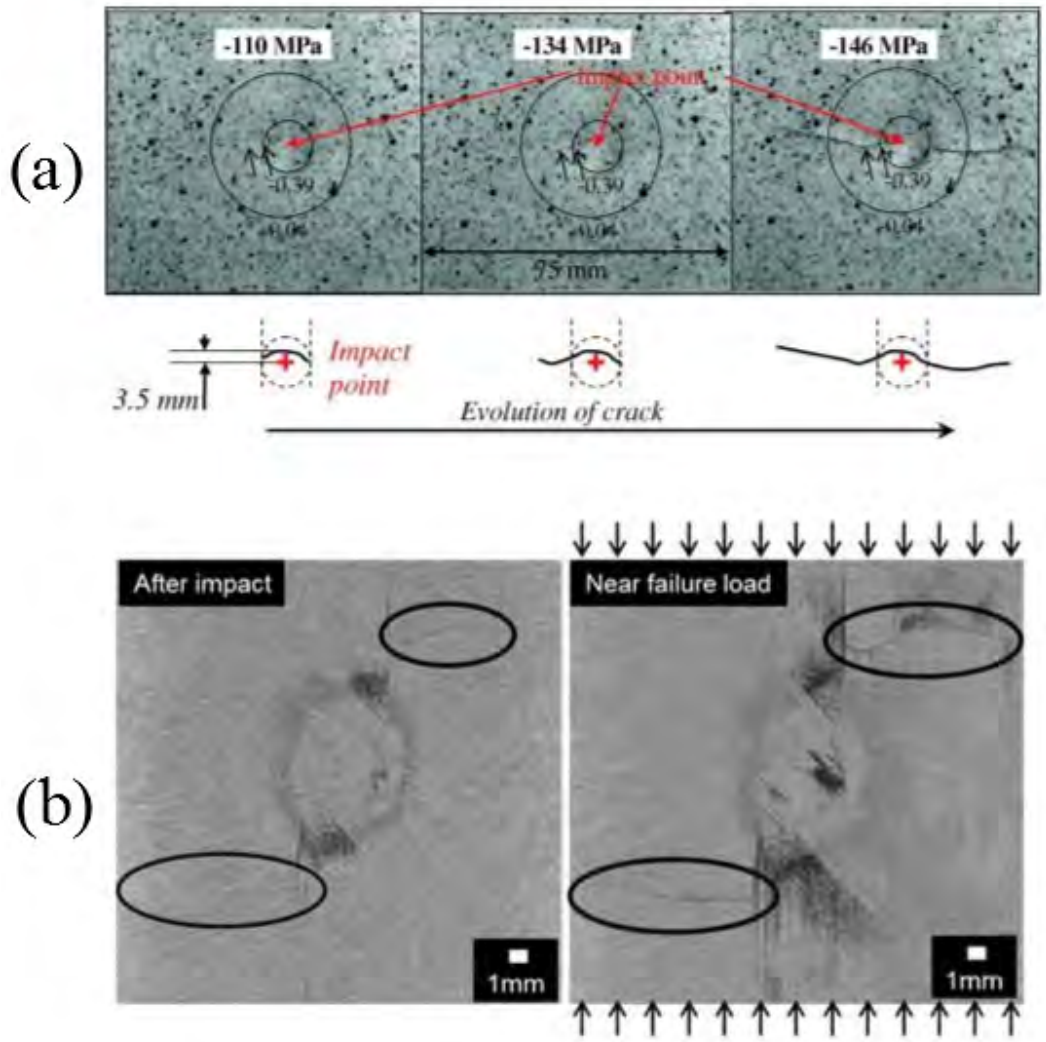

Fig. 2.7: Fibre fracture propagation process, (a) from 0° ply of the impacted face in [56] (material: G30-500/RTM6, layup: $[0_2/45_2/90_2/-45_2]_s$, thickness: 4.16 mm), and (b) sixth 0° ply from impacted face in [10] (material: not revealed, layup: $[45/0/\text{-}45/90]_{3s}$, thickness: 4.6 mm).

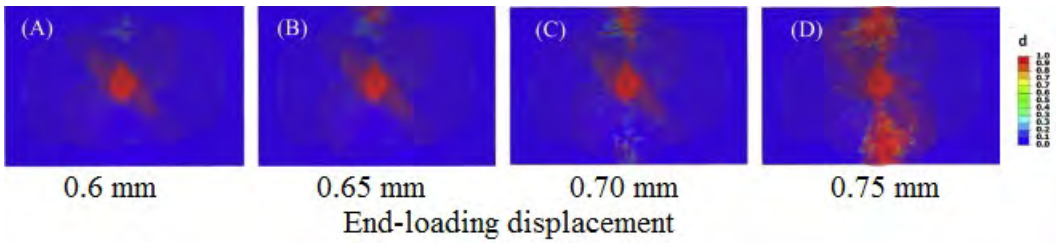

Fig. 2.8: A sequence of superimposed intralaminar matrix damage maps at different displacement, obtained from the virtual CAI test on the panel impacted with 29.5 J, taken from [65].

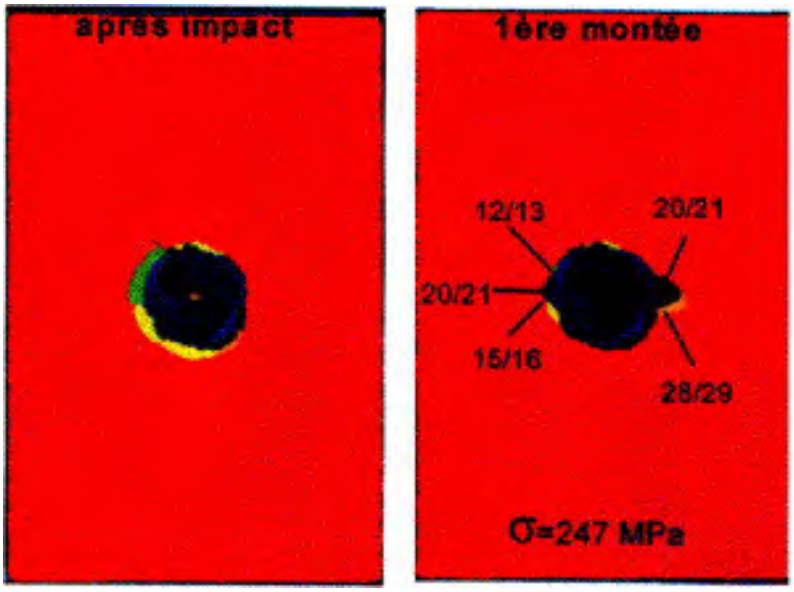

Fig. 2.9: C-Scan indicating delaminations propagation detected after interrupted test at 247 MPa on an impacted sample (final failure load: 278 MPa), taken from [43].

Many researchers have agreed that the local buckling of impacted-induced delaminations within the impacted zone plays a key role in the compression failure of CAI coupons [62, 67]. Nonetheless, this phenomenon is not informative enough to explain the final failure because delaminations are observed to not always propagate over the entire width of the test coupons in most cases, and the ultimate failure is due to the sudden propagation of different impact-induced damage modes [56].

Early findings

Earlier research findings in the literature suggested three scenarios of failure sequences as summarized in [10] and references therein.

1. *Sublaminate buckling leads to a sudden growth of damage extending laterally, leading to a sudden failure of the coupon* [49, 68, 69].

2. *Sublaminate buckling leads to a load redistribution resulting in compressive fibre fracture* [70–72]

3. *Sublaminate buckling leads to a combination of bending and compressive loads in the remaining undelaminated regions and the final failure is believed to occur when these stresses exceed the maximum compressive stress in the* 0° *plies* [73]

In [68], the impact damage growth during CAI loading was mainly delamination propagation normal to the loading direction. The propagation was observed to start at a relatively low speed and accelerate into a smooth and rapid delamination growth. The delamination growth speed was estimated to be 850 m/s, and claimed to be influenced by the strain level. In [49], delamination propagation in width-wise

direction is more extensive than the lengthwise direction. In [69], woven composites were studied and the investigation was conducted on FEM models without intralaminar damage model.

Recent findings

Attempting to better understand the failure sequence, researchers have fine-tuned both experimental test instrumentation [10, 56] and finite element models [9, 65]. The following is a summary of recent contributions to the CAI failure process.

Rivallant et al. [9] used an FE model developed with the focus on improving accuracy of fibre fracture prediction in order to understand the role of this damage mode in CAI failure. They summarized the CAI failure process as follows: (1) CAI stress increases until buckling appears, and (2) when there is enough deflection due to the local buckling of damage area or enough stress concentration to lead to strain failure at the tip of the surface 0° ply crack, this crack propagates until the coupon fails. Therefore, the failure in CAI is due to a coupling between the buckling and the 0° ply crack on the impacted surface. Another study of Rivallant et al. [56] used 3D DIC to make detailed analyses of plates during CAI tests. They also observed the coupling between the buckling and 0° surface ply crack and concluded that the link between the two phenomena is not obvious from a purely experimental analysis.

Bull et al. [10] used ex-situ micro-focus CT to observe damage development at incremental loads during CAI tests. They found the following CAI failure process: (1) during CAI loading up to near failure load, delamination grew into the undamaged cone under the impacted site (Fig. 2.10), but no delamination growth outside the envelope of the projected delamination area was observed, and (2) the growth is driven by the sublaminate out-of-plane deflection and consequently, increasing the unsupported length (Fig. 2.11), and (3) pre-existing 0° ply fibre fracture also propagates along width-wise direction.

Tan et al. [65] developed a 3D composite damage model and implemented it as a user material subroutine in ABAQUS/Explicit to simulate both LVI and CAI response. Although CAI failure sequences were not addressed in the study, considering the CAI prediction accuracy (Fig. 2.12), the contribution of failure mechanisms to CAI failure is appreciated. According to Fig. 2.13a, the rapid increase in fibre-dominated damage–associated with the highest level of energy dissipation–causes a sudden load drop and is accompanied by propagation of delamination and intralaminar matrix damage as well as moderate increases in ply-to-ply friction. Fig. 2.13b indicates that both delamination and intralaminar matrix damage propagate from the impact-induced damage area, and that fibre damage is very localized and primarily observed in the top and bottom plies.

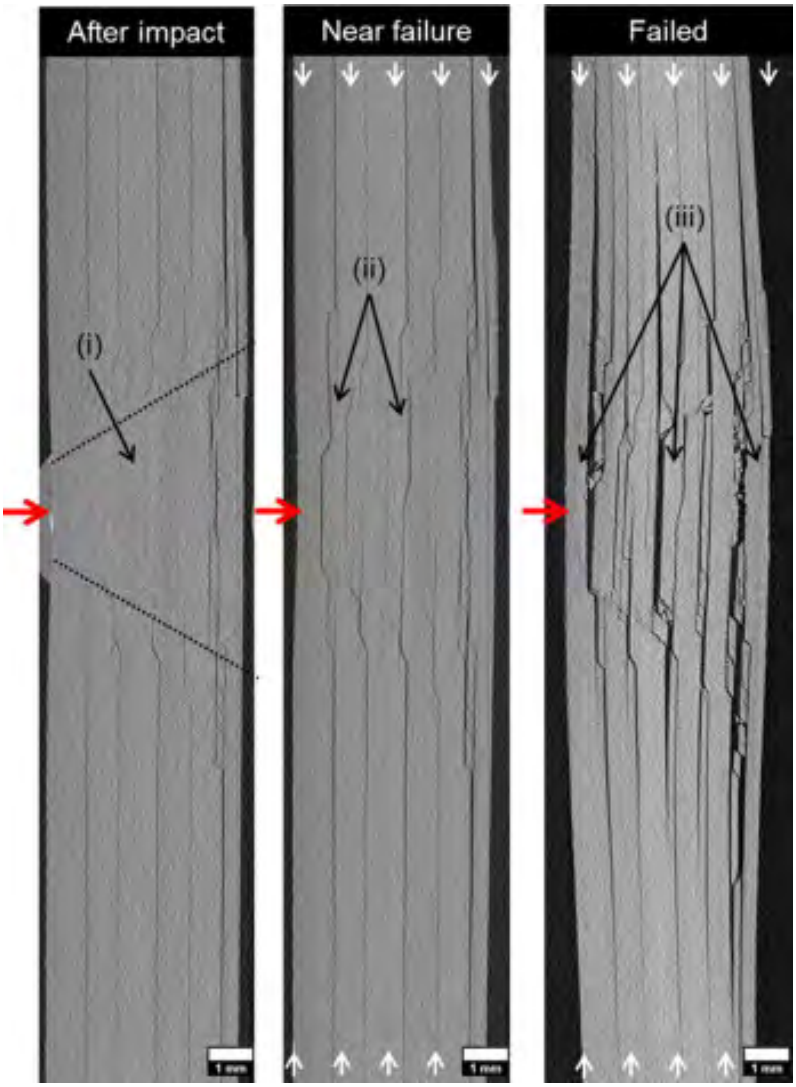

Fig. 2.10: μCT cross-section at the impact site, red arrow indicating impact location, and white arrows indicating CAI loading direction. (i) Undamaged cone, (ii) delamination growth into the undamaged cone and (iii) sublaminate buckling; taken from [10].

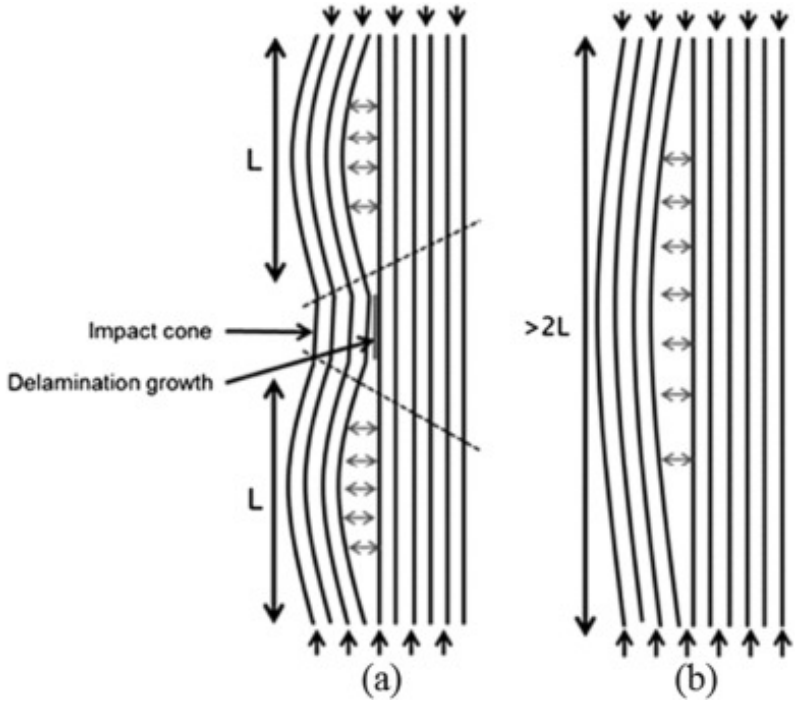

Fig. 2.11: Schematic showing (a) the unsupported length of the sublaminate L and delamination growth into the impact cone and (b) more than doubling of the unsupported length due to delamination growth explaining the great reduction in the residual compressive strength of a damaged laminate; taken from [10].

Summary and implication

From the above contributions, the current state-of-the-art knowledge about the CAI failure can be summarized as follows:

1. There are two distinguished regimes of the damage propagation before the ultimate failure of impacted specimens: pre-buckling and post-buckling of the sublaminates.

2. The pre-buckling of the sublaminate consists of delamination propagation into the undamaged cone under the impacted zone.

3. The post-buckling of the sublaminate constitutes the sudden propagation of intralaminar matrix cracks, delaminations and pre-exiting 0° ply fibre fracture.

4. The sublaminate buckling appears to remain the cause of instability, after the post-buckling regime starts, leading to ultimate failure.

The observation that sublaminate buckling drives delamination propagation into the undamaged cone and followed by sudden CAI failure provides a mechanistic explanation for the role of toughness in determining the CAI strength. Delaying this delamination propagation, by developing tougher resin, may delay the sublaminate

buckling-induced instability. As a result, the CAI is expected to increase as reported by [10, 74].

2.3 Inextricable link between DR and DT

2.3.1 Damage resistance (DR) and Damage tolerance (DT)

In the literature, damage resistance to low velocity impact is often described with the following parameters:

- Damage threshold load F_d, a sudden load drop or a decrease of slope due to specimen stiffness loss [75]. It can be identified on either the load-time or load-displacement curves. F_d is well known as as delamination threshold in low velocity impact analysis.
- Peak impact load F_{max}, the maximum load either on load-time or load-displacement curves.
- Dissipated energy E_{dis}, the amount of energy consumed by different failure mechanisms, mainly those described in Section 2.1.
- Indentation depth δ_{ind}, the foot print left behind by the impactor. It can be measured using dent depth gauge just after the impact test.
- Projected damage area A_{pro}, the total damage area envelope in which matrix cracking, indentation, and fibre breakage also exist in addition to extensive delamination being the main failure mode. A_{pro} is well known as projected delamination area. It can be measured using ultrasonic C-scan, or some methods described in the beginning Section 2.1.

Although A_{pro} is often used to characterize the damage resistance, the approach is questionable when used to compare different layups. The reason behind is that how much one can see delaminated areas through C-Scan depends on MMAs through the thickness direction, which is layup-dependent. A reasonable way to compare damage resistance based on delamination areas across different layups would be to measure the total delamination areas. Chen et al. [76] suggested that F_{max} be used to characterize the damage resistance of laminated composites. However, the remaining parameters should not be ruled out as an indicator of damage resistance.

Damage tolerance in the context of compression after impact is defined as the maximum compressive load divided by the cross section of the test coupon, giving what is commonly known as CAI strength σ_{CAI}. The CAI strength is normally plotted

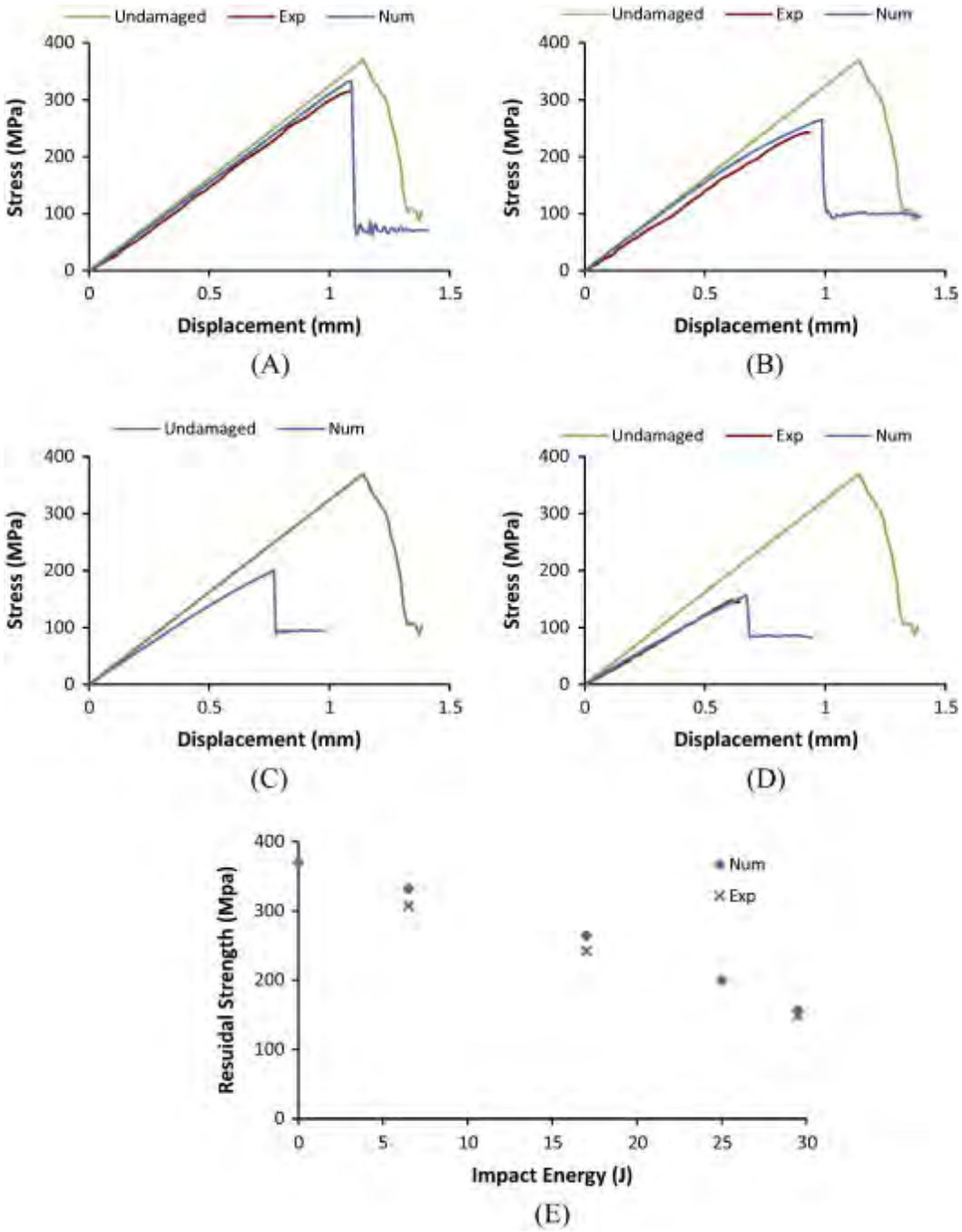

Fig. 2.12: CAI stress–displacement curves: (A) 6.5 J, (B) 17 J, (C) 25 J, (D) 29.5 J and (E), taken from [65]. Compared to experimental results, the ultimate stresses were predicted to within 10% of experiment results.

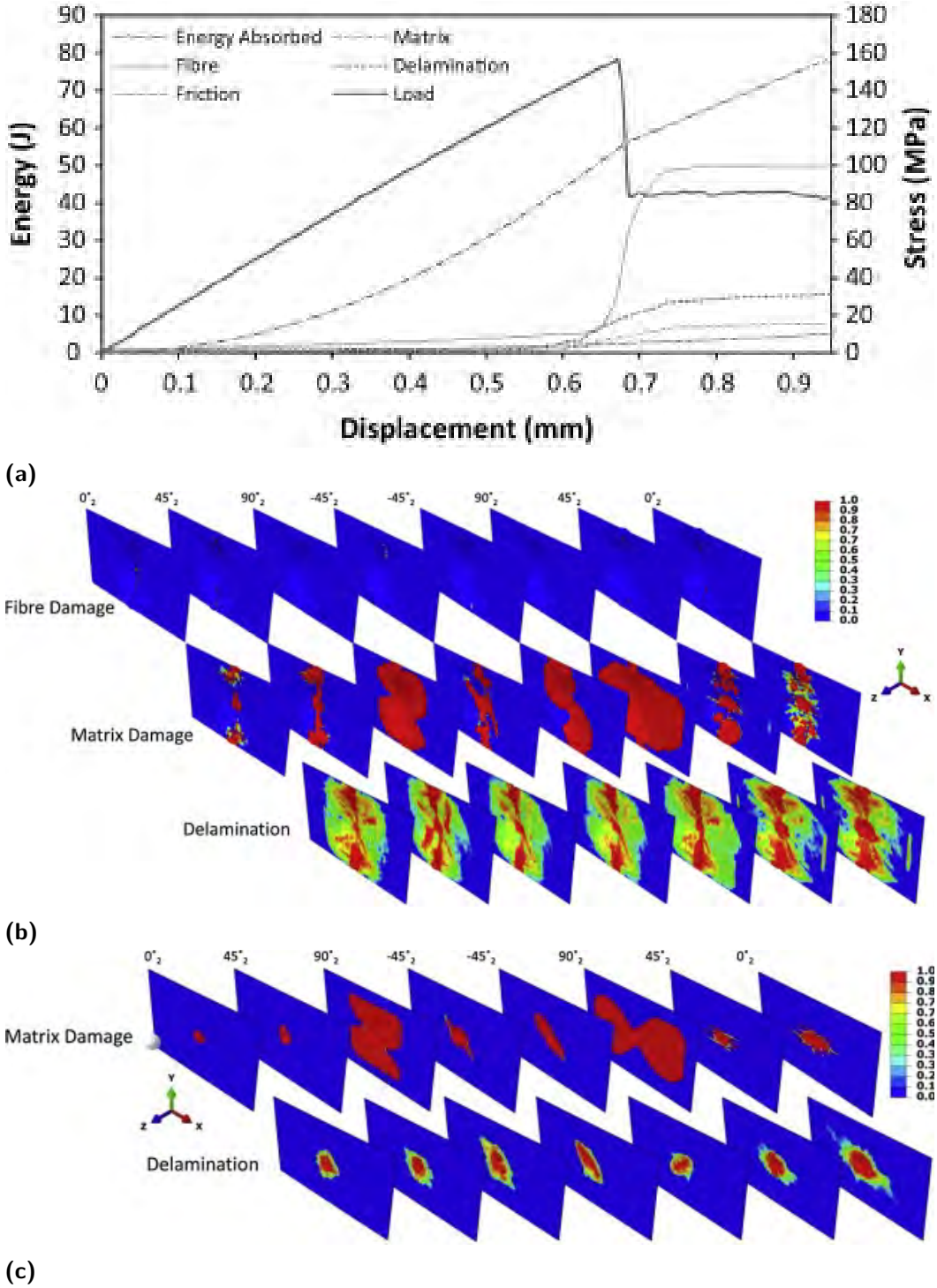

Fig. 2.13: Simulation results CAI for 29.5 J impact case: (a) energy dissipation consumed by different damage modes, (b) damage contours of different damage modes, and (c) damage contours of damage modes included for comparison to case (b), adapted from [65].

against a damage resistance indicator, as earlier mentioned. The following section presents the correlation between damage resistance and damage tolerance.

2.3.2 Correlation between DR and DT

In an attempt to offer a fast and cheap technique without resort to complex and expensive CAI tests, researchers have tried to correlate damage resistance parameters to find out whether they can be used as an alternative to assess damage tolerance. In other words, by looking at any of the damage resistance parameters of laminates with different layups and/or made of different composite systems, is it possible for one to tell which laminate is more damage tolerant?

CAI strength and projected damage area
In the work of Bull et al. [10], for the same damage area, particle-toughened systems demonstrated up to 30% improvement in failure stress when compared to untoughened systems, suggesting that the link between σ_{CAI} and the size of A_{pro} is not straightforward. In fact, even for laminates comprising only differences in layups but made of the same composite system, Sebaey et al. [17, 18] demonstrated that assessing the damage tolerance by comparing the size of A_{pro} can be misleading, for the dispersed/nonconventional laminates are more damage tolerant although they have larger A_{pro} in comparison to the baseline laminate (Fig. 2.14).

CAI strength VS damage threshold load, and VS impact peak load
Following the work of Cartié and Irving [74], for laminates of the same layup and fibre but different resins, composite laminates with higher F_d resulted in better CAI strength. Conversely, in the experimental study by Sebaey et al. [18], this phenomena could not be observed for laminates made of the same composite systems but different layups. Their nonconventional layup was found to have σ_{CAI} 30.7% higher than the baseline layup although F_d of the nonconventional laminate was lower by 19%. Similarly, for the relationship between σ_{CAI} and F_{max}, Sebaey et al. [17] reported that although the impact peak load F_{max} of their nonconventional laminate was up to around 20% lower than that of the the baseline layup, its CAI strength σ_{CAI} was up 30%.

CAI strength and impact dissipated energy
To the knowledge of the author, the relationship σ_{CAI} between E_{dis} is barely discussed. This is perhaps because very little have been observed for different laminates as in the case reported in [17], see Fig. 2.14. Indeed, the plot of σ_{CAI} against impact energy is usually preferred.

CAI strength and indentation depth
Some researchers [53] considered the indentation depth a good indicator of the residual CAI strength. Nonetheless, a closer look into the experimental data docu-

mented in [17] reveals that it can not be possibly used to compare damage tolerance of different layups. Sabaey et al. [17] noted that the nonconventional layup offered 30.7% increase in σ_{CAI} despite having deeper indentation of around 25% in comparison to the baseline. **Summary**

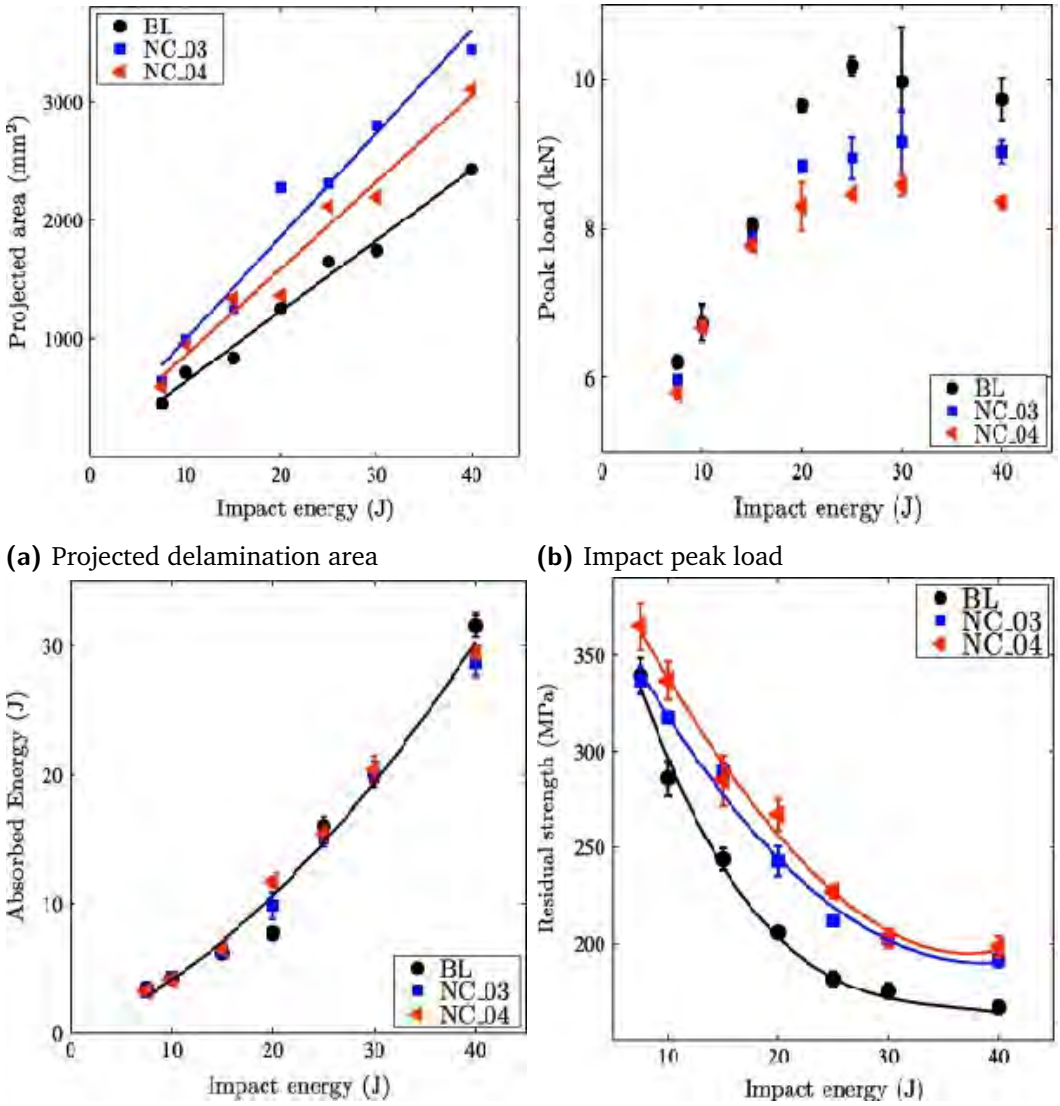

(a) Projected delamination area

(b) Impact peak load

(c) Dissipated energy

(d) CAI strength

Fig. 2.14: (a) Projected delamination area, (b) Impact peak load, (c) Dissipated energy, and (d) CAI strength, [17].

We have seen damage resistance and damage tolerance are not necessarily correlated when the CAI strength of different layups made of the same composite system is compared. Indeed, impact-induced damage is distributed through the thickness of the laminate. Considering delamination, its associated parameters consists of not only out-of-plane position but also three other attributes: orientation, shape and size. This suggests that impact damage morphology, rather than the damage resistance parameters, is inextricably linked to the CAI strength.

2.4 CAI strength–predictive models

Predicting CAI strength is a very challenging task due to the complex impact damage morphology formed by the presence of different failure modes which may compete and interact during the CAI failure process. Predictive models thus should attempt to consider the inextricable link between CAI strength and impact damage morphology.

2.4.1 Analytical models

Elliptical soft inclusion method

Xiong et al. [77] presented an analytical method to predict σ_{CAI}. They modelled the impact damage detected by the ultrasonic time-of-flight C-scan technique as an elliptical soft inclusion. Degrading the material elastic moduli in the inclusion was made with the sublaminate buckling analysis. To estimate σ_{CAI}, they used the complex potential method to determine the stress distribution, and the resulting stress in conjunction with three failure criteria (point stress/average stress, maximum stress and Tsai-Wu). They also proposed finite width correction in order to eliminate the need for FE calculations. Validating the analytical method with experimental data shows good agreements (material: T800H/3900, layup: $[45/0/\text{-}45/90]_{3s}$). They also noted that the out-of-plane deformation and the reduction in bending moduli of the sublaminate due to asymmetric lay-up influence the sublaminate buckling σ_{BK}. Ignoring σ_{BK} leads to the overestimation of σ_{CAI}. The complex potential method can be found in [78] whereas the semi-empirical point stress criterion in [79].

Circular soft inclusion method

To predict σ_{CAI}, Qi and Herszberg [80] presented a semi-empirical method which modelled the impact damage as a soft inclusion with an exponentially reduced stiffness. The in-plane stress distribution near the damage was determined with the complex variable method, and the failure stress with point stress failure criterion. The method was used to predict σ_{CAI} of the carbon/epoxy woven laminates with reasonable agreement to the experimental data.

Equivalent hole approximation

Many researchers [11, 70, 71, 81] have proposed to approximate σ_{CAI} with an equivalent hole in the same fashion as the open hole compression. This approach may be motivated by two reasons. First, the impact damage distribution is roughly cylindrical and circular in out-of-plane and in-plane view. Second, the similarity of damage growth pattern between open hole and impact damage during compression loading [70]. The differences in the aforementioned references lies in how the compressive failure stress is predicted and/or the whole dimension is estimated.

Soutis and Curtis [11, 70] exploited a CZM to estimate σ_{CAI} by modelling the impact damage zone as an equivalent open hole. The CZM replaces the inelastic deformation near the hole edge with an equivalent crack loaded on its faces by a bridging traction decreasing linearly with the crack closing displacement. The hole diameter can be determined from either X-radiographs or C-Scan images. The model requires two independently measured laminate parameters: plain compressive strength and fracture toughness. The error in the strength prediction was less than 10% in most cases.

In the approach proposed by Puhui et al. [71], they calculated the stress distribution around damage using the complex potential method and classical laminate theory. To estimate σ_{CAI}, Load-Bearing Ply Failure (LBPF) was used. The LBPF is also known as the layup independent failure; the development was presented in [82] and the applicability later scrutinized in [83]. They found that σ_{CAI} depends on the width of damage zone (as observed in other studies [45, 81, 84] which in return is related to many parameters (impact energy, impactor shape and dimension, etc.). The study also presented a technique for determining the equivalent hole shape and size.

Khondker et al. [81], rather than using CZM or LBPF for failure prediction to estimate σ_{CAI}, applied the point stress failure criterion. This requires an experimentally-determined characteristic length. When used to predict knitted composites, the model gives the error of less than 5% in most cases in comparison with experimental σ_{CAI} data. They also noted that, for knitted composites, one characteristic length is applicable for a range of damage geometries and knit architectures. This is not the case with composites made from unidirectional prepreg plies, for their characteristic length depends on the lay-up configuration and hole geometry.

2.4.2 Finite element models

There has been an increasing volume of publications on numerical modelling of LVI. Nonetheless, fewer studies have gone on to simulating CAI tests. Among them, González et al. [64] may be the first to numerically predict CAI strength with a rigorous 3D FE model that considers both interlaminar and intralaminar progressive damage. Rivallant et al. [9] later presented an FE model with the focus on improving fibre failure prediction under LVI and implementing it for CAI test. The FE model presented by Tan el al. [65] considers both inter- and intra-laminar damage modes and yields only 10% discrepancy from experimental data.

The success of numerical approaches to modelling impact damage and CAI strength lies in the correct description of failure under both interlminar and intralaminar modes from the initiation to evolution of the damage. Moreover, the more rigorous the model becomes, the more demanding the computational power becomes. This

constraint still prevents the FE models from being used as a tool to search for better stacking sequences in terms of the CAI strength.

2.5 CAI strength-governing parameters

Although the CAI strength has been an important area of research for decades owing to its role in assessing the damage tolerance of laminated composites, little is known about its controlling factors. Some authors suggested that the matrix is a significant factor influencing tolerance to impact damage [85]. In the literature, researchers have made some efforts to gather information regarding the key factors that govern the CAI strength [86–88].

Greenhalgh and Hiley [86] published a review article on the assessment of novel materials and processes for the impact tolerant design of stiffened composite aerospace structures. They suggested that, through improvements in the critical material parameters, significant increase in the impact tolerance of skin-stringer panels can be achieved. These parameters include Mode I toughness (G_{IC}), Mode II toughness (G_{IIC}), bending (D_{11}) and shear (G_{12}) moduli, and compressive (σ_c) and flexural strength (σ_f). Unfortuately, no data related to the correlations between impact tolerance and any of these parameters were presented in the paper.

Tang et al. [87] surveyed the literature results on the CAI strength and interlaminar fracture toughness. Fig. 2.15 shows that generally, CAI strength of laminates does not have clear relationship with mode I matrix toughness G_{Ic}^{m}, mode I interlaminar toughness G_{Ic}^{c}, and mode II interlaminar toughness G_{IIc}^{c}. Unfortunately, the correlation does not consider other factors such as resin type, fibre type, fibre volume fraction, lay-up configuration, and processing methods. The authors only mentioned that the CAI strength depends on a variety of other properties: stiffness, strength, ductility and fracture toughness of fibres, matrices, and interfaces/interphases.

Nash et al. [88] suggested resin toughness, mode I interlaminar toughness G_{Ic}, compressive modulus and strength are the critical material properties that govern the compressive damage process. This suggestion was justified as follows: when an impact causes a delamination this effectively divides the laminate into sub-laminates that are more susceptible to buckling when loaded in compression; the compressive failure of a laminate involves a combination of global buckling of the laminate, local buckling of any sub-laminates, and micro-buckling of the fibres [57]; micro-buckling causes interlaminar matrix cracking, whereas local buckling promotes the growth of delamination and the failure of 0°-plies in the laminates; and ultimately, the compressive residual strength is determined by the resistance to local buckling of the sub-laminates.

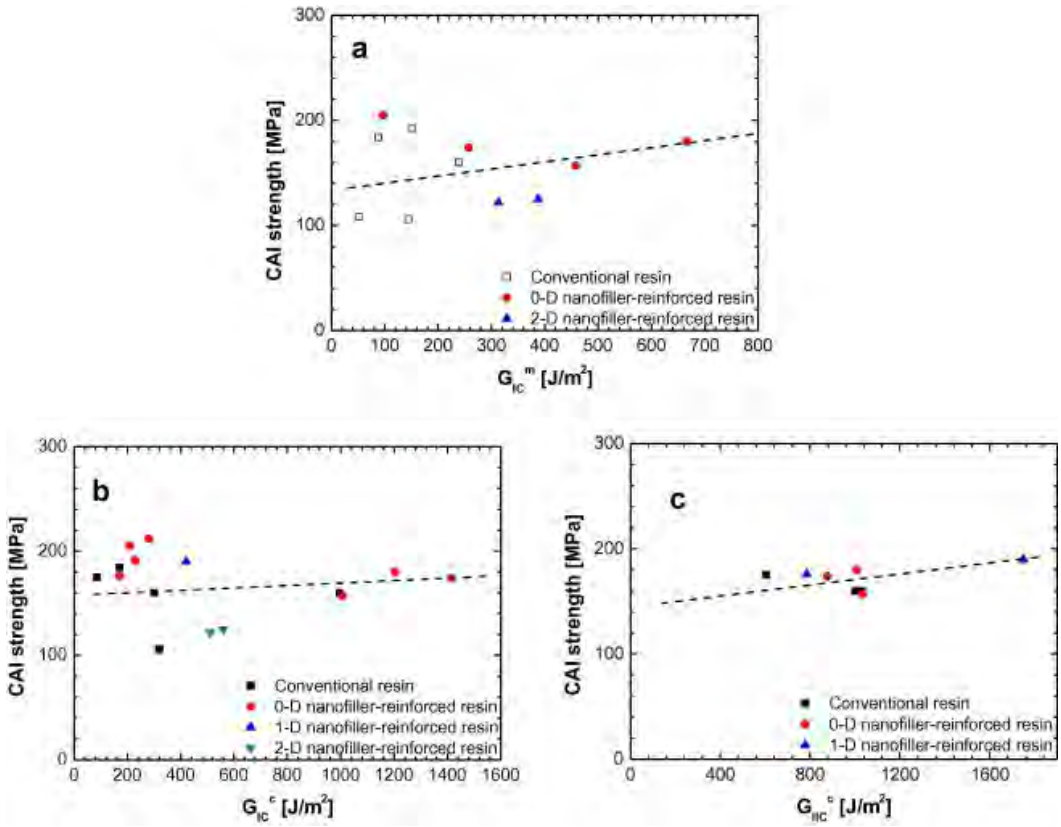

Fig. 2.15: CAI strength with (a) G_{Ic}^{m}, (b) G_{Ic}^{c}, and (c) G_{IIc}^{c} for pristine and nanoparticle-modified resins and their laminates. G_{Ic}^{m}, G_{Ic}^{c}, and G_{IIc}^{c} are mode matrix toughness, mode I interlaminar toughness, and mode II interlaminar toughness.

Tab. 2.1: Properties of the constituents of the pre-pregs used (data supplied by Hexcel), taken from [74]; X_T: tensile strength, X_C: compressive strength; ϵ_T: tensile strain; G_{Ic}: fracture toughness; T_g: glass transition temperature.

Properties	922 (Resin)	914 (Resin)	924 (Resin)	920 (Resin)	HTA (Fibre)	IMS (Fibre)
E (GPa)	4.05	3.9	3.8	3.76	238	295
X_T (MPa)	56	47.7	65	34.9	3400	5400
X_C (MPa)	196	180	175	290		
ϵ_T(%)	1.7	1.4	2.4	8.41	1.4	1.7
ν	0.38	0.41	0.41	0.39		
G_{Ic} (J/m^2)	51	103	150	541		
T_g (°C)		190	190	107		

Tab. 2.2: G_{Ic} and G_{IIc} for selected materials, taken from [74]; %: percentage of scatter in the test data; F_c: damage threshold load, commonly defined as critical threshold load for onset of delamination; F_r: rest load, the load level at the drop just after F_d is reached.

Laminate	F_c (kN) (%)	F_r (kN) (%)	$F_c - F_r$ (kN)	G_{IIc}^{Cal} (J/m^2)	G_{IIc}^{Exp} (J/m^2)
HTA/922	4.05 (6.4)	2.87 (7.4)	1.18	298	-
IMS/922	4.11 (5.2)	2.98 (7.2)	1.13	310	-
HTA/914	5.38 (2.6)	2.36 (9.4)	3.02	482	530±130 (T300/914)
HTA/924	6.53 (2.4)	4.55 (3.2)	1.98	615	-
IMS/924	6.50 (2.7)	4.59 (4.0)	1.91	683	700±50
HTA/920	6.79 (1.9)	6.15 (2.0)	0.64	729	766±9 (T300/920)
IM7/8552	5.62 (13)	4.00 (11)	1.62	777	800±100 (ELS)

Although there have been suggestions related to governing parameters, they are too general for the definitive conclusion to be reached. In what follows, efforts are put on collecting some experimental results to relate the CAI strength improvement with some of the suggested factors.

2.5.1 Effects of resin and fibre

Cartié and Irving [74] investigated the effect of resin and fibre properties (Table. 2.1 and 2.2) on impact and CAI performance of CFRP and concluded that resin toughness rather than fibre strength and stiffness is the major parameter influencing CAI performance in quasi-isotropic CFRP laminates (Fig. 2.16). They also suggested that the major difference in A_{pro} in composites containing different resins is a consequence of changes in F_d owing to the variation of G_{IIc}). Section 2.5.2 further elaborates on the effect of different toughness values.

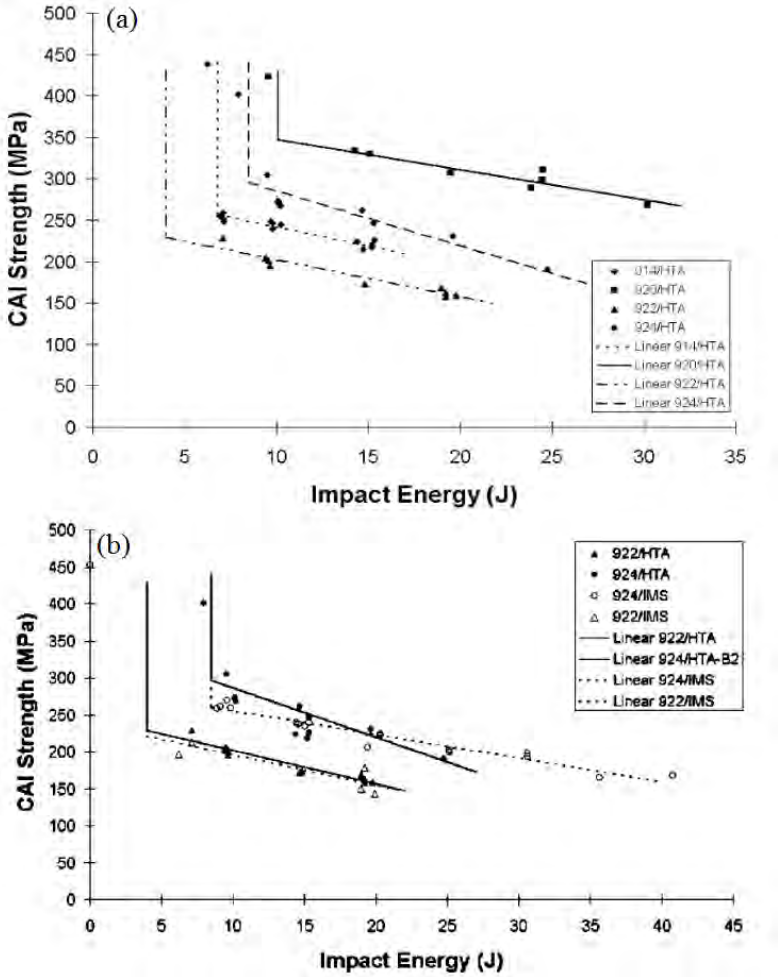

Fig. 2.16: Effect of constituent materials on CAI strength: (a) types of resin matrix and (b) types of fibre, taken from [74].

2.5.2 Effects of toughness

The fracture toughness of both matrix resins G_{mc} and interlaminar interface under mode I G_{Ic} and mode II G_{IIc} have long been correlated to σ_{CAI}. To see the clear effects of toughness, CAI strength reported in [74, 89] were reproduced here. Fig. 2.17 indicates that increasing toughness of either matrix or composite in both mode I and II improves σ_{CAI}. Enhancing G_{IIc} can be done through many ways such as inserting resin-rich interlaminar layers[89] or substituting conventional epoxy with thermoplastic resin [84, 90].

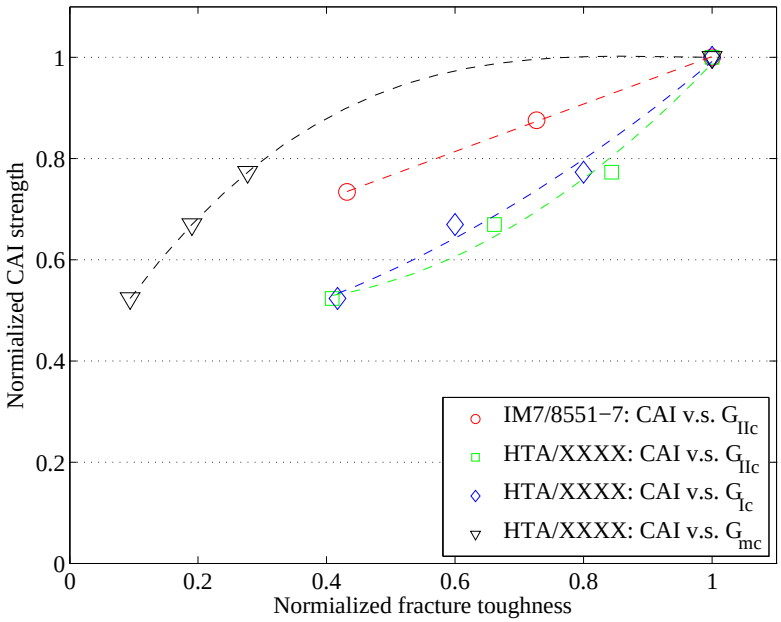

Fig. 2.17: Relationship between toughness; IM7/8551-7, reproduced from [89]; HTA/XXXX, reproduced from [74] for impact energy of rough 15 J; XXXX refers to different resins being ranked from lowest to highest toughness being: 922, 914, 924, and 920 respectively. G_{Ic} of HTA/914 is replaced with that of T300/914.

2.6 Approach to improving CAI strength

2.6.1 Stacking sequence design

The stacking sequence design (SSD) approach exploits the design flexibility of laminate stacking sequences without the need to change the constituent materials or modify their properties, to design a new ply architecture or to use fillers to an existing composite system. Two main techniques have been reported in the literature regarding this design of damage tolerant layups, namely sublaminate buckling-based optimization, and nonconventional/dispersed laminate approach.

Sublaminate buckling-based optimization

This approach has been introduced in a series of works presented by the University of Bath research team [91–96]. It is an extension of 1D-propagation model of an isotropic strut containing a delamination, considered in [97–99], to the case of a 2D-anisotropic plate. The idea is to optimise the compressive strain level at which an embedded circular delamination propgation initiates, namely the threshold strain, given by [95]:

$$\varepsilon_{th} = \varepsilon_c \left(\sqrt{4 + \frac{2G_{Ic}}{\varepsilon_C^2 A_{11}}} - 1 \right) \tag{2.1}$$

where

- ε_c is the compressive strain level at which the sublaminate buckles
- G_{Ic} is the static mode I interlaminar fracture toughness
- A_{11} is the axial stiffness of the sublaminate calculated with classical laminate theory

The development of the model was motivated by the following two observations:

1. Local buckling load of multiple delaminations can be predicted by a single delamination at a critical depth.
2. Only delaminations located at the critical depth of 10–20% of total thickness grow to permit buckling of the delaminated layers.

This first observation was reported in the study of buckling loads of laminates containing through-the-width delamination using FE models based on 2D plane strain [100]. The second observation was made in an experimental study of the compressive fatigue limit for coupons with barely visible impact damage of 0°-ply dominated and quasi-isotropic layups [101]. The authors offered no reason regarding why the depth of 10–20% of total thickness is critical.

This approach is an indirect CAI strength optimization scheme in that σ_{CAI} is anticipated to increase only by maximising ε_{th}. The novelty of this method lies in its close form solution of the threshold strain, which is convenient for variables to be optimised. Unfortunately, determining ε_c represents the main challenge in the optimisation procedure as there is no close form solution for ε_c. In [91–95], obtaining ε_c value has to rely on using buckling program VICONOPT [102]. In VICONOPT, the plate is divided into strips in order for their edges to be constrained by nodes approximating a circular boundary (Fig. 2.18c). Indeed, any general purpose commercial FE software can also be used to determine ε_c; for example, ABAQUS was used in [96].

Some experimental results of layups obtained from the model

Using Equation 2.1 together with Genetic Algorithm, Baker and Bulter [94] reported an increase of 13% in σ_{CAI} of an optimised nonconventional layup in comparison to the baseline. Later, Rhead [95] reported 10% improvement of σ_{CAI}, resulting from this optimisation methodology. In the same study [95], 43% improvement of CAI strength was attained with a layup obtained from semi-optimisation, $[\pm 45_4/(90/0)_4]_S$. The placement of $\pm 45^\circ$ plies was used as one among optimisation constraints, and was based the author's experience to mimic current design philosophy for preventing global buckling [95]. Based on the Equation 2.1, placing 90° as surface ply minimises A_{11}, which in turn maximizes ε_{th}, and thus the enhancement of σ_{CAI} is anticipated to be higher than in other orientations. In fact, such anticipation was noted in an preliminary design study based on the values of ε_{th} predicted by the model [93], prior to the experimental data provided in [95].

A subsequent implementation of the model by Baker et al. [103] to study fully orthotropic laminates found two types of damage tolerant laminates: one without 90° plies and high Poisson's ratio ν_{12}, and the other with one or two 90° plies and low ν_{12}. The authors also observed that non-symmetric layups do not have higher ε_{th} than the anti-symmetric ones, but also do not introduce any significant disadvantage assuming that laminates require only one damage tolerant face. In addition, non-symmetric layups were not outperformed by symmetric layups at any total ply number ranging from 7 to 21 laminae. Last but no least, adding plies may reduce the overall load-carrying capacity.

Basic assumptions of the model

This improvement level revolving around Equation 2.1 alone is still limited. However, the limitation may be the direct consequence of some of the assumptions required to achieve such a simple expression. For completion, summarized below are the assumptions behind the model (discuss Refs: [91–93] for details):

1. The propagation of BVID can be simplified to propagation at a single circular delamination located at a depth of 10-20% from the backface.

2. The impacted test coupons fail by delamination buckling leading to propagation of damage away from the original site.

3. The sublaminate is so thin that has the effect of allowing no energy to be released from the thicker unbuckled sublaminate, (Figs. 2.18a and b.).

4. The circular perimeter of the delamination (Fig. 2.18c) is assumed to be clamped.

5. The diameter of the circular delamination has to be chosen from a suitable through-the-thickness delamination distribution model.

The first assumption was justified by two studies previously mentioned [100, 101]. The model is not applicable to problems where the initial mechanism of failure is via kink banding or buckling of the full laminate due to the second assumption. The consequence of the third assumption makes the model practical for problems involving compression failure that is governed by propagation delamination under mode I fracture. The fourth assumption implies that no buckling displacement or rotation is allowed at the delamination boundary. The last assumption makes the model depend on experimentally observed out-of-plane delamination distribution. Consequently, it is difficult to implement this in the optimisation procedure of dispersed laminates because there is insufficient experimental data as in the case of conventional quasi-isotropic layups.

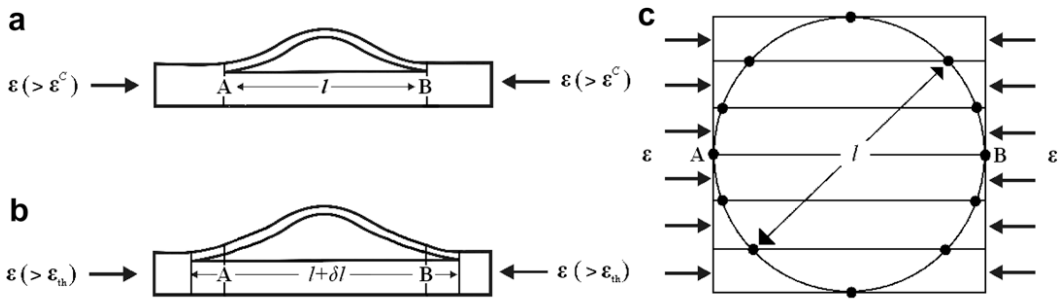

Fig. 2.18: Thin film model showing: (a) post-buckled central section through AB; (b) propagated central section and (c) plan view of circular delaminated plate of diameter l with nodes and strips to illustrate VICONOPT discretisation, taken from [93].

Nonconventional/dispersed laminate approach

In this approach, the ply angles with respect to the loading direction are not limited to 0, $\pm$45, and 90°. These the conventional ply orientations have been widely used in the current industrial practice. The only challenge in this method is to design a nonconventional layup that has the engineering constants as close as possible to those of the conventional baseline layup. As the method has the freedom to use all possible ply orientations, the design space is greatly enlarged. As a result, manual selection would be a daunting task, and optimization algorithms such as Genetic or Ant Colony are needed [16].

Relatively recent experimental campaigns have shown some advantages of using non-conventional ply orientations to enhancing CAI strength. Lopes et al. [15] suggested that exploiting the delamination parameters selecting proper MMAs between plies could result in dispersed laminates with enhanced CAI strength. The idea was later investigated by Sebaey et al. [17, 18], demonstrating that up to 30% improvement in CAI strength was realized by considering nonconventional ply orientations.

2.6.2 Material development approach

The material development approach (MDA) involves the need to change the constituent materials, or introduce new ply architectures or add extra phase(s) to an existing composite system.

Z-pinned laminates
Zhang et al. [104] reported an approximately 45% higher CAI strength in pinned specimens than that of the unpinned counterparts. Such improvement was found to be relatively independent of specimen thickness and impact energy, and dependent on the magnitude of z-fibre traction force that in turn is a function of the pinning parameters. They also noted that all the pinned specimens had higher failure strains than the unpinned specimens, suggesting that the use of z-fibres could increase the design strain limit for aircraft structures by about 50%. A mechanistic interpretation of pinned composites, in comparison to 3D woven and stitched laminates in terms of in-plane mechanical properties, was offered by Mouritz and Cox [105].

Stitched laminates
Tan et al. [106] reported that stitched specimens have noticeably higher CAI strength of 60% more than unstitched laminate. The improvement depends on stitch density and thread thickness; high density offers promising enhancement, 50% in some cases, of CAI strength [32, 107–110] whereas low density provides only marginal or no increase in the residual strength [111–114]. A closer look into the two factors by Tan et al. [106] revealed the following: (1) at low impact energy level, CAI strength is highly dependent on stitch density in which stitch spacing should be sufficiently small to ensure stitches become effective in inhibiting sublaminate buckling and resist delamination growth, and (2) at high impact energy level, CAI strength is intimately related to both stitch density and stitch thread thickness, since stitch fibre bridging is apparent when the impact-induced delamination area is sufficiently large.

Interply hybrid laminates
This type of laminate has two types of UD prepreg, each containing distinct fibre; for example, glass fibre prepreg and carbon fibre prepreg. The enhancement of 30% of CAI strength was long ago reported by Cantwell et al. [115]. A very recent study [116] demonstrated an increases in structural efficiency of 41-51% in comparison to the most damage tolerant layup reported in their preceding study [95]. Other advantages of such laminates include cost saving and light weight structure [117, 118].

Interlaminar particle-reinforced laminates
Compared to untoughened systems, particle-toughened systems demonstrated up to 30% improvement to failure stress for a given damage area [10].

CNT-integrated laminates

While the interlaminar fracture toughness of a composite can be considerably improved by adding CNTs, the effect of these improvements on the CAI strength is less pronounced [119]. Kostopoulos et al. [120] reported the increase in the CAI strength of the CNT modified CFRPs was around of 12–15% for impact energy levels between 8 and 20J. The improvements were attributed to CNT pull-out, CNT breakage and crack bridging as additional energy dissipation effects. They also suggested that the CNTs perform better at higher strain rates.

Thin-ply based laminates

Saito et al. [121] reported that thin-ply laminates showed 23% higher CAI strength than standard-ply laminates (thin-ply thickness: 0.038 mm, and standard-ply thickness: 0.147 mm). They observed that the thin laminates experience few and localized transverse cracks and delamination was largely propagated in the mid-plane.

Thick- and thin-ply based hybrid laminates

The results of mixing thick and thin plies to improve CAI strength has recently been reported by Sebaey et al. [122], where thin-ply thickness of 0.085 mm and thick-ply thickness of 0.330 mm were considered. The authors considered two layup architectures: one with thick plies in bottom and top sublaminates surrounding a block of thin-plies at the mid-plane, and the other with each thick ply surrounded by two thin plies. The latter was found to enhance the CAI strength by 15%. A different degree of CAI strength enhancement would have been expected if the study had considered unidirectional prepreg tapes in this their study.

Interleaved laminates

Recognizing that the presence of impact-induced delaminations can impair the CAI strength, researchers have attempted to reduce the delamination size by inserting into the interlaminar interface a thin interlayer, commonly known as the interleaf. Xu et al. [123], using nano-hybrid films as an interleaf to reinforce the interlaminar interfaces, has achieved an increase in the CAI strength by 33%. More reticently, García-Rodríguez et al.[124] has explored the advantage of non-woven veils to enhance the CAI strength and reported an a noticeable improvement of 22%.

2.7 Environmental effect

Another great concern in the aerospace industry is the influence of environmental conditions such as moisture and temperature on the composite performance as these factors have been reported to affect the behaviour of the composite materials in various loading conditions. Ogi et al. [12] reported that moisture causes volumetric changes, reduces glass transition temperature (T_g), and increases the critical stresses for transverse cracking and delamination by reducing residual stresses. Single-fibre

fragmentation tests [13, 14] recently revealed that moisture is detrimental to the fibre/matrix interface shear strength. Kafodya et al. [125] experimentally observed that the presence of moisture results in pronounced degradation in short beam shear strength, and less or negligible effects on the tensile strength and modulus.

Regarding moisture effects on impact behaviour and CAI strength, only few experimental studies have been found in the literature [126–128]. Among them, only two were carried out to examine the compression after impact strength with results limited to only one impact energy level for laminates made of carbon/epoxy UD prepreg tapes [127], or to woven glass/epoxy composites [126]. This clearly suggests that more efforts should be put to understand the influence of environmental factors.

2.8 Compression of artificially-damaged laminate

We have seen that low velocity impact leaves laminated composites with a complicated damage morphology that results from the interaction between different failure mechanisms. During CAI loading, these failure mechanisms may interact and result in a failure process that is challenging to discern, as already reviewed. To comprehend the complex phenomenology underlying the CAI behaviour, researchers have been interested in studying compressive behaviour of laminates with artificial impact damage, a simplification of the realistic impact damage morphology. Whether a single failure or multiple mechanisms should be investigated is still an open question. Nonetheless, delamination is considered to be the dominant damage mode causing failure under compression for relatively thick laminates in particular [129].

2.8.1 Delamination and the attributes

The studies of the compressive behaviour of delaminated laminates have considered many parameters associated with delaminations, namely their attributes. Fig. 2.19 illustrates a single delamination and its many attributes. On the top are the two types of delamniations: through-the-width delamination (TWD) and embedded delamination (EMD), see Fig. 2.19a. A single delamination may be of different shapes and sizes, depending on the level of simplification and/or experimental observation (Fig. 2.19b). Each delamination may align in a particular orientation (Fig. 2.19c). In addition, when modelling a single delamination, the thickness-wise position has to be considered. Finally, to model multiple delaminations, one has to confront with several possible patterns of through-the-thickness distributions, Fig. 2.20.

Owing to the aforementioned delamination attributes, the number of publications on the compressive behaviour of laminates with artificial impact damage has become increasingly large. In addition, the approaches to addressing the problem may be

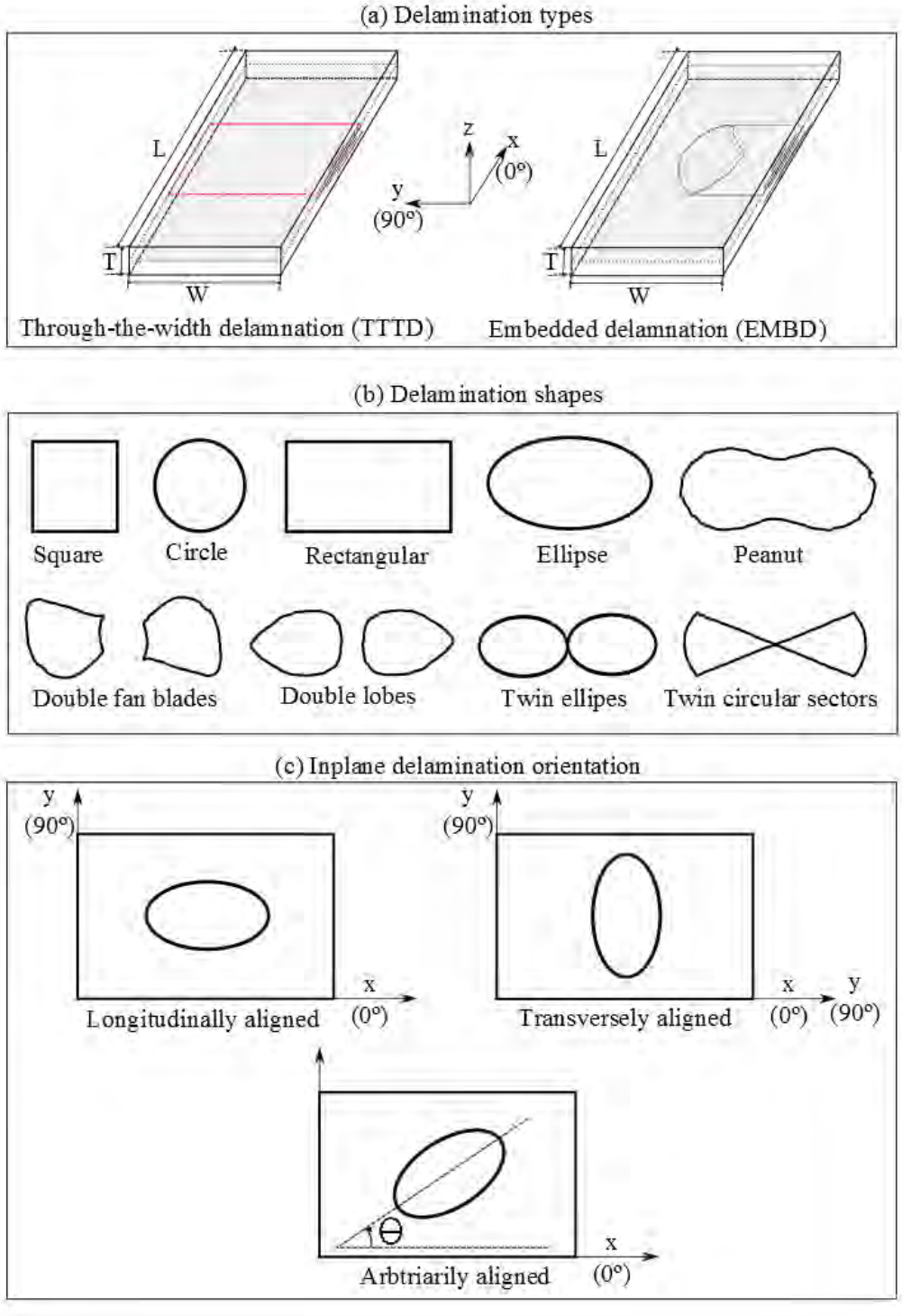

Fig. 2.19: Some features delaminations: (a) Two delamination types–through-the-width delamination and embedded delamination irregular shape; (b) Distribution shapes studied and/or suggested in the literature to simplify impact-induced delamination; (c) Inplane orientations of an elliptic delamination.

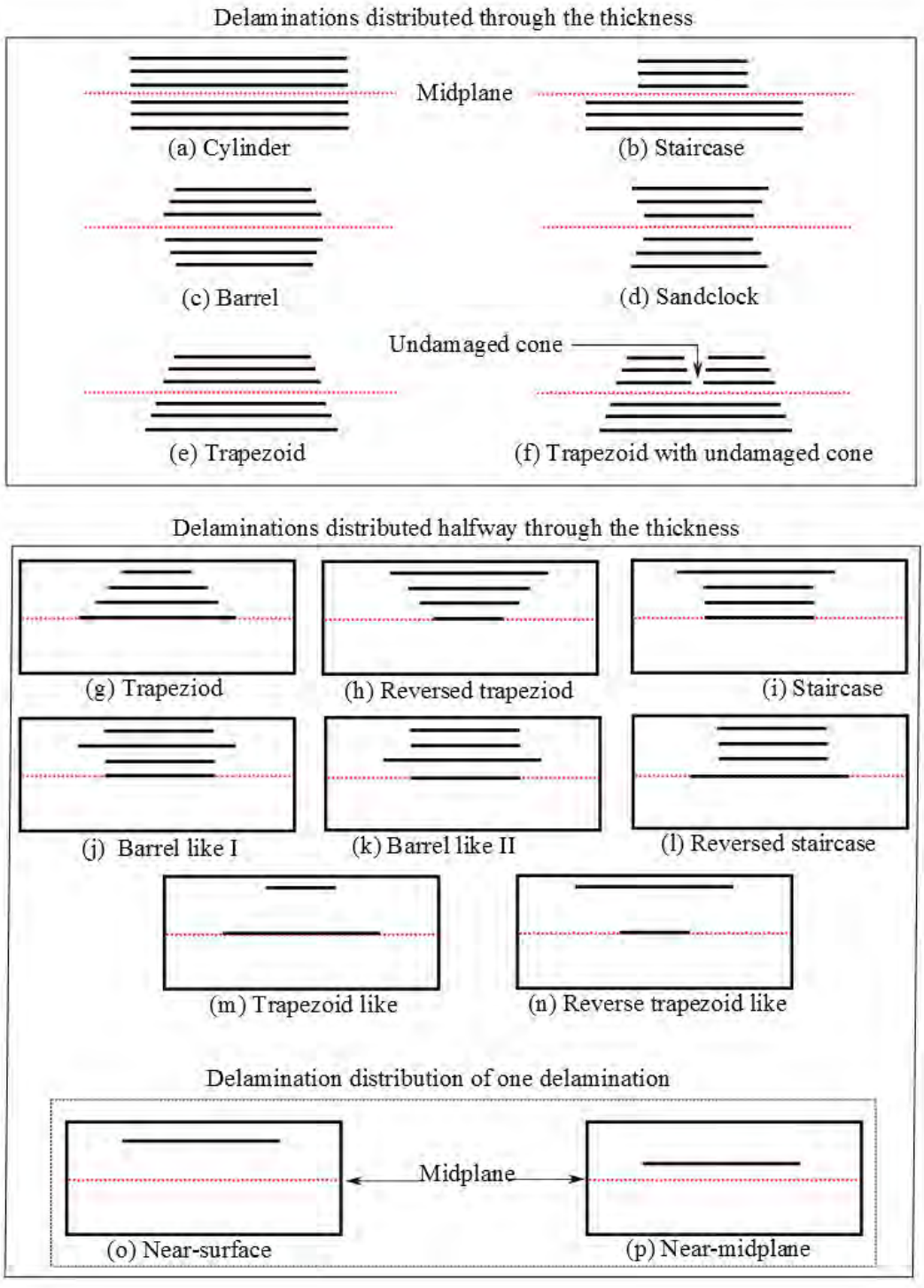

Fig. 2.20: Delamination distributions of single and multiple delmainations positioned through the thickness and only halfway through the thickness to simplify impact-induced delamination distribution patterns.

of purely analytical or numerical in nature or even a mix between the two. On top of this, the fact that the laminate behaviour also depends on layups may hinder the generalization of the conclusions from one study to another. Consequently, categorizing all the findings on this particular topic into well-structured subtopics without overlap to some extent turns out to be a challenge, not to mention the influence of boundary conditions and specimen sizes on the compressive behaviour. Notwithstanding these numerous factors, the research interest in delaminated plates mostly centres on the following:

- analysing the buckling modes
- determining the buckling loads F_{bk}
- comprehending the post-buckling behaviours

2.8.2 Buckling modes and shapes

The buckling modes and their associated shapes, according to [130], are depicted in Fig. 2.21 for laminates with a single through-the-width delamination. There exist three buckling modes: global, local and mixed ones. Among them, the local buckling can occur in only one U-shape. These behaviours have generally been observed for the case of laminates being not too slender. For a TWD, buckling modes are influenced by the ratio of the delamination length to the laminate length (a/L). Increasing the ratio a/L may alter the buckling modes from global to mixed and local buckling. For an embedded delamination, the laminate buckling modes and shapes cannot be simply illustrated as in Fig. 2.21, for the buckled shape in the delaminated region is a 3D surface in nature.

2.8.3 Buckling loads

Generally speaking, the following factors are considered to influence the buckling loads:

- Delamination size
- Delamination depth (through-the-thickness position)
- Delamination shape (embedded delamination case)
- Delamination orientation (embedded rectangular or elliptic delamination)
- Delamination number and distribution (multiple delaminations)
- Layups, boundary conditions and specimen dimensions

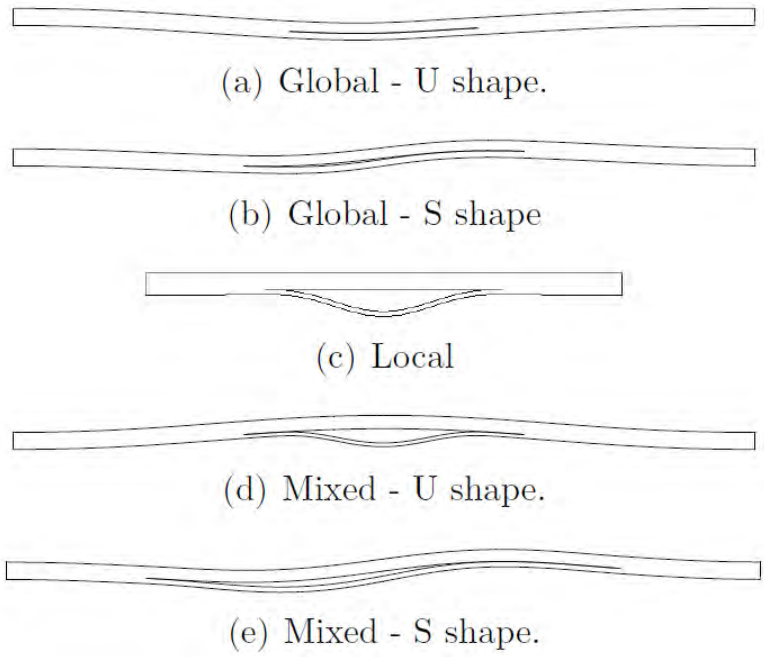

Fig. 2.21: Buckling modes and associated shapes for a single through-the-width delamination, taken from [130].

Delamination size and depth

Following [130], the way in which these two factors affect the buckling load can be best pictured with Fig. 2.22. The thin-film model assumes that only the sublaminate buckles where the general model does not. These influences have been reported in several studies [131–138]. The range of a/L that does not affect the buckling is generally known as the critical delamination length. As the delamination gets deeper (high ratio h/H), the buckling load tends to increase.

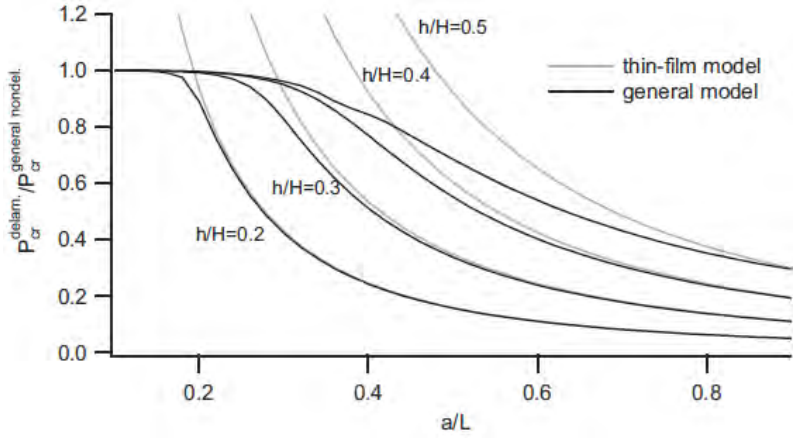

Fig. 2.22: Influence of the delamination size and depth for the case of through-the-width delamination; h/H: the ratio of delamination depth (h) to the laminate thickness (H); a/L: the ratio of delamination length (h) to the laminate length (L); taken from [130].

Delamination shape

Obdržalék and Vrbka [138] considered three delamination shapes: circular, elliptic and extremely irregular delaminations. The first two cases were included to assess their applicability to the irregular one. In most cases, they found that the ellipse better represents the irregular shape than the circle one does, with the worst case scenario resulting in slightly more than 20% discrepancy of buckling loads (more 50% for circle).

Delamination orientation

Yeh et al. [132] studied one delamination of elliptic shape with different sizes, through-the-thickness positions and orientations changing from 0° to 90°. They reported that the sublaminate buckling mode changes from global to mixed type as the elliptic delamination major axis is rotated (from 0° to 90°). Hu et al. [134] examined one delamination of elliptic and circular shape located at the interface between the first and second plies from the laminate surface and found that transversely-aligned elliptical delamination affected F_{bk}^{s} more than both longitudinally-aligned elliptical and circular ones do. Tafreshi et al. [139] investigated one delamination of elliptic and rectangular shape located at the midplane and noted the same observations as reported in [132, 134]. Obdrzalek and Vrbka [136] observed the decrease in $F_{bk,l}$ of an elliptic delamination becomes more and more sensitive to changing orientation from 0° to 90° as its through-the-thickness position is located away from the midplane (orientation < 30%, position > 50%). They also suggested that for the prediction to be accurate, delamination orientation should match that of the fibre in the lower ply of an interface.

Delamination number and distribution

It seems to be intuitive that more delaminations can cause greater reduction in the buckling loads, but this is not always true and the situation may alter when the distribution type is involved. Let's take, as an example, an FE study of Hwang et al. [100] who studied the situations as shown in Fig. 2.23. For Type I, Near-surface longest delamination controls buckling behaviour regardless the configuration of the remaining delaminations; the buckling loads of single and multiple delaminations are almost the same. For Type II, moving the longest delamination to the midplane increases the buckling load (and also causes the buckling mode to change). Their subsequent experimental study Type IA and IC confirmed their FE finding [140].

Layups, boundary conditions and specimen dimensions

The sublaminate buckling loads under the influence of boundary conditions, geometric parameters and layups have been reported by Park and Lee [141]. The authors considered a four-ply laminated plate with an embedded rectangular delamination between first and second laminae. The boundary conditions (BC) were simply supported and clamped. Three types of aspect ratios were analysed: delamination length to plate length D/L, plate length to plate width L/W, and plate length to

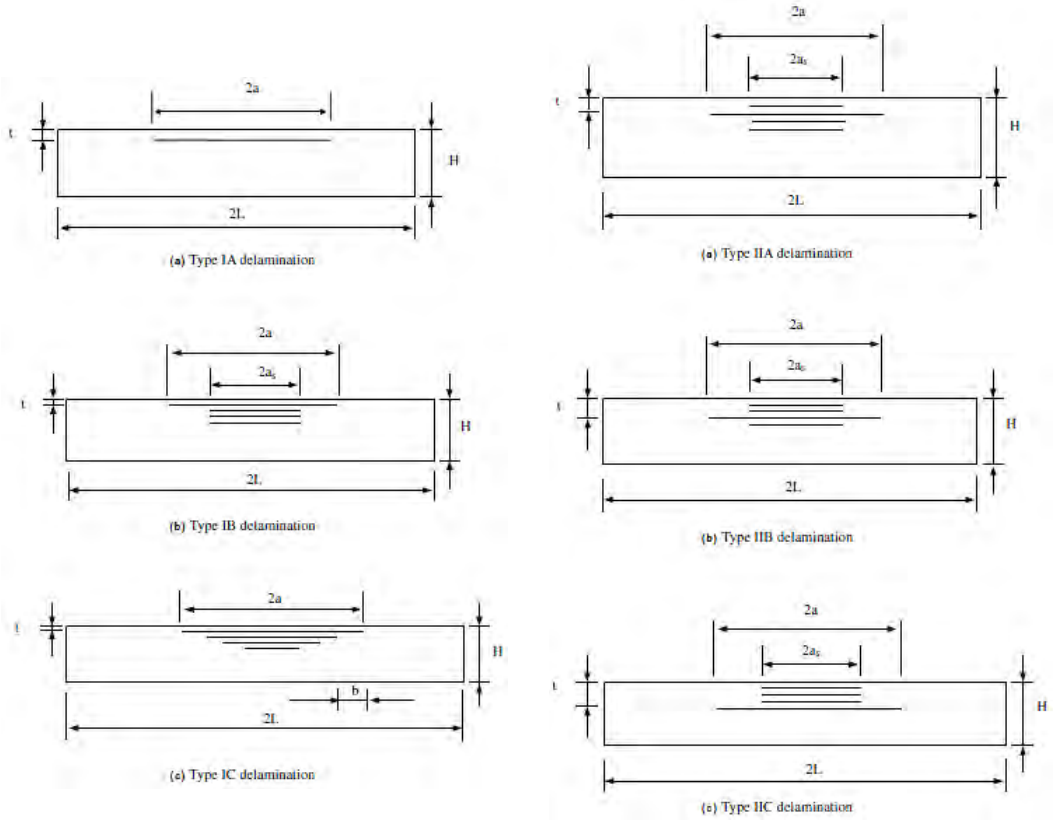

Fig. 2.23: Number and distribution types delaminations in the study by Hwang et al. [100].

plate thickness L/T. The chosen layups were: unidirectional, cross-ply, and symmetric and anti-symmetric angle ply laminates. Their results can be summarized as follows:

- F_{BK} of clamped BC are higher for $D/L \leq 0.6$ in unidirectional laminate, $D/L \leq 0.6$ in cross-ply laminate, and $D/L \leq 0.3$ in symmetric ± 45 laminate.
- F_{BK} decreases substantially for $L/W \leq 2$, $W/T = 10$ and $0.4 \leq D/L \leq 0.8$.
- F_{BK} is not affected in the range $10 \leq L/T \leq 100$ and $D/L \leq 0.2$.
- F_{BK}, for $D/L > 0.2$, decreases drastically with increasing L/T.
- Angle-ply laminates of MMA=60° results in the highest F_{BK}.
- For both BCs, increasing D/L changes buckling modes from global to mixed to local ones.

The influence of layup on the buckling loads was also observed in many other studies [131, 137, 139, 142].

2.8.4 Post-buckling behaviour

The research works on post-buckling responses, i.e. the behaviour right after the buckling to the collapsing moments, may often involve the compressive behaviour from the delamination growth onset to laminate failure. The first studies to analyse post-buckling responses with the main focus on delamination growth are those reported between the early 1980s and 1990s [97, 143–148]. Only through-the-width delamination was considered in [97, 143, 144]. The shapes of the embedded delaminations are of square and rectangular for [146], and circle and ellipse for [145, 147]. Matrix cracking and fiber breakage were also analysed in [148]. Their findings can be summarized as follows:

1. The growth of the delamination may be stable, unstable or an unstable growth followed by a stable growth [97].

2. Calculated G_I and G_{II} are very sensitive to delamination length, delamination depth, and load level [143].

3. A large increase in G_{Ic} results in a moderate increase in critical load for delamination growth for short delaminations [144].

4. Large increase in G_{IIc} results in a substantial increase in critical load for delamination growth for long delaminations [144].

5. Besides the delamination depth, the fracture energy and elastic properties of both sublaminates also control the delamination growth behaviour [145].

6. The total ERR varies significantly along the delamination front; hence, no self-similar growth is expected [146].

7. The growth direction, parallel or perpendicular to the loading direction, is influenced by three factors: the delamination size, the applied strain level, or the position along delamination front [146].

8. The delamination grows under mixed-mode behaviour with negligible contribution from mode III; either G_I or G_{II} can dominate the growth behaviour [147].

9. The locations of maximum G_I, and G_{II} depend on the delamination shape and the applied strain [147].

10. Parts of the delamination will overlap if contact constraints at delaminated interface the are included in FE model [147].

11. In addition to delamination growth, the post-buckling deformation can lead to matrix cracking and fiber breakage [148].

Subsequent studies by other authors also supported the above findings and noted some other interesting findings. Lee et al. [149] reported that the bending stiffness of the sublaminate in the delamination zone governed the delamination growth. They also noted that a lower bending stiffness in the loading direction would produce greater ERR and thus promoted the delamination growth at the crack front. Tafreshi et al. [139] investigated one embedded delamination of elliptic and rectangular shape located at the midplane and suggested there existed layups more resistant to delamination growth. Obdržalék and Vrbka [138] reported the influence of circular, elltiptic and irregular shapes on propagation direction at delamination growth onset, the magnitude of different modes of ERR.

2.8.5 More on a single delamination

Many past studies on a single delamination have also gone beyond the buckling loads, modes and growth onset. Gaudenzi et al. [135] highlighted it is important to model delamination growth in the postbuckling behavior. Using VCCT, Riccio et al. [150] reported the tendency of delaminations around mid-plane to propagate unstably; Wang and Zhang [151, 152] demonstrated that mode I ERR is greater than mode II ERR before buckling and became smaller after buckling.

A recent CZM-based study based [142] has added some more insights. Delaminations around the mid-plane of the laminate does not only propagate unstably but also decrease the laminate stiffness significantly and accelerate ultimate failure. Near-surface delaminations propagate stably despite being the cause of the reduction in local buckling of sub-laminates. Some unsymmetric stacking sequences exhibit almost the same compressive behaviour in comparision to symmetric layups. The authors also suggested that FE models ignoring delamination growth might not be reliable.

When both inter- and intra-laminar damage are included in the study of laminates with through-the-width delaminations, the laminate failure loads have been shown to be considerably higher than the sublaminate buckling loads [153–155]. In [155], it was reported, for a through-the-width delamination, that compressive failure loads are 50% higher than the delamination propagation onset loads, and 500% higher than the sublaminate buckling loads. Riccio et al. [156] found that laminate failure loads with a single circular delamination can be more accurately predicted with the consideration of matrix cracking and fiber fracture based on Hashin's failure criterion and the instantaneous stiffness reduction.

2.8.6 More on multiple delaminations

The problem of multiple delaminations get more complicated as one has to consider the types of distribution associated to them, not to mention the attributes of each delamination. For multiple delaminations, sublaminate buckling load F_{bk}^{s} may decrease appreciably or inappreciably. Regardless of the distribution types, studies [100, 131, 140, 157, 158] found that multiple delaminations have nearly the same F_{bk}^{s} as that of a single delmaination with its length being equal to the longest delamination of multiple delaminations. In contrast, Aslan and colleagues [159, 160] reported a noticeable reduction in F_{bk}^{s} when shorter delaminations are placed underneath a long near-surface delamination.

Suemasu et al. [161] modeled the impact damage including both matrix cracks and delaminations. The delamination shapes were of twin circular sectors distributed through the laminate thickness. They found that there was no significant delamination growth prior to laminate failure under global buckling. A followup study by the same authors [8] used cohesive elements. This study considered three cases of FE models: one, three and four circular delaminations. For the first case, the delamination was placed at the laminate midplane. In the other two cases, delaminations were placed at equal distance along the laminate thickness. They found that, shortly after the delamination propagation onset, the applied load slightly increased and then dropped. They concluded that the compressive strength was governed by the delamination growth.

2.8.7 Quasi-realistic impact damage

While there have been considerable research on multiple delaminations, some studies have put a deal of efforts to have a model that reflects a realistic impact damage morphology so that the results are more meaningful.

Pavier and Clarke [162] conducted an FE study taking into matrix cracks, delaminations, and fibre cracks. The damage morphology resulted from LVI test obtained with the de-ply technique was used to idealize delamination as a rectangular and fractured fibres as a line. To predict the ultimate failure, the laminate was assumed to fail when the stress level along the loading direction reached the experimentally-measured compressive strength of the pristine laminate. Their FE model was based on stress analysis and showed good agreement between experimental failure loads and numerically predicted ones.

Craven et al. [129] developed an FE model that was able to take into account multiple delaminations. Each delamination could have circular, elliptic or peanut shape (Fig. 2.19b). Two types of delamination distribution were possible: trapezoidal and cylindrical (Fig. 2.20a and e). Fibre fracture cracks were also modelled with the

idealized forms of line, star and random. However, not included damage evolution of the embedded failure mechanisms. This is a very rigorous FE model with damage morphology almost the same as impact damage. The model was used to study only delamination buckling. A whole of insights would have been gained if such a model had been validated with experimental as it enables the impact damage modes to be studied separately or collectively.

2.9 Summary

The literature review has so far shown that the complexity of impact damage morphology (IDM) and CAI failure mechanisms and sequences poses a great challenge to the understanding of the CAI behaviour. Consequently, little is known about how to design a stacking sequence that best tolerates the impact damage.

There have been suggestions related to the parameters that may influence the CAI strength but they are too general to obtain a working model for better damage tolerant layups. Specific parameters have been investigated, but they are related to the material development approach (e.g. interlaminar fracture toughness and different types of resin and fibre).

The analytical models for predicting CAI still depend on IDM from the experiment in order to determine the damage diameter. Since the IDM is a function of the stacking sequence in a given composite system the models cannot be used for layup design. The FE model relies on not only the accurate interlaminar and intralaminar damage modelling, but also requires a full set of well-characterized material properties, not to mention the intensive computational resource needed.

Regarding the artificial impact damage, most published papers have focused on predicting the buckling load of the laminates rather than failure loads. Moreover, the influence of the through-the-thickness location of a single delamination on the failure load of the laminate is still needed so as to have an idea about which interfaces delaminations should be promoted or suppressed.

The most appealing approach to improving the CAI strength has been identified to be the stacking sequence design through stiffness tailoring. However, it requires a more systematic strategy regarding the deployment of the MMAs in order to promote the delamination through the thickness.

Above all, the literature has justified the objectives stated in Section 1.3 that mainly support the aim of understanding the compression after impact of the laminated composites for designing better damage tolerant laminates.

Part II

Methodology

Methodology

3

3.1 Material and specimens

Unidirectional prepreg tape with a nominal cured ply thickness of 0.184 mm was used to produce all the three laminates described in the experimental test campaign of this thesis. The material is T800S/M21, a carbon/epoxy composite of intermediate modulus, high tensile strength fibre preimpregnated in high-performance toughened matrix. The elastic properties of the ply are summarized in Table 3.1. The full set of material properties along with their methods of characterization can be found in [163] and references therein. The prepreg tape was supplied by Hexcel®. All laminates were manufactured according to standard autoclave procedures.

All the laminates were cut into test coupons of 150 mm in length and 100 mm in width. The cut was made such that the 0° ply orientation is aligned with the specimen length. Fig. 3.1a shows the schematic of ply orientations aligned with respect to the specimen geometry. These configuration were used throughout all experimental tests including the low velocity impact, quasi-static indentation and compression after impact.

To prepare the specimens for the tests, a total number of 12 measurements were made on each specimen: six thicknesses close to impact location (T1-T6), three lengths (L1-L3) and three widths (W1-W3), Fig. 3.1b. For all the measurements, a Mitutoyo digital caliper capable of extending up to 250 mm was used, see Fig. 3.1c.

3.2 Experimental tests

Tab. 3.1: Elastic properties of T800S/M21 unidirectional ply [163]

Property	Unit	Value	Description
E_{11}	GPa	152.8	Longitudinal Young's modulus
$E_{22} = E_{33}$	GPa	8.7	Transverse Young's moduli
$\nu_{12} = \nu_{13}$	-	0.335	Poisson ratio in planes 1-2 and 1-3
ν_{23}	-	0.380	Poisson ratio in plane 2-3
$G_{12} = G_{13}$	GPa	4.2	Shear moduli in planes 1-2 and 1-3
G_{23}	GPa	3.15	Shear modulus in plane and 2-3

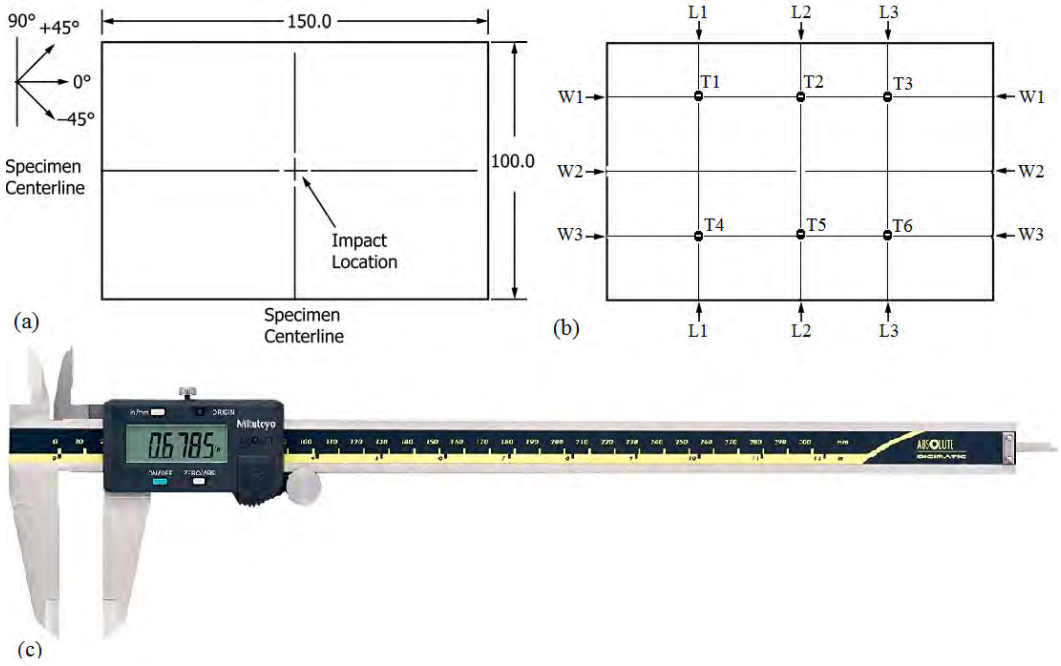

Fig. 3.1: (a) specimen dimensions in millimeters and fibre directions with respect to the specimen geometry, and (b) locations of dimension measurements of six thicknesses close to impact location (T1-T6), three lengths (L1-L3) and three widths (W1-W3)., and (c) Representative photograph of the digital caliper used in specimen measurements.

3.2.1 Low velocity impact tests

Test standard ASTM D7136 [164] was followed for the low velocity impact. Impact tests were performed with a CEAST Fractovis Plus drop-weight impact test machine. The whole testing facilities comprised of the test machine, built-in software and the acquisition system which together allowed the desired impact test data to be captured automatically. The impact velocity v inputted into the software was calculated according Equation 3.1, where m is the impact mass and E the desired impact velocity. Throughout the test campaign, a mass of 5 kg was used. The recorded data included impactor contact force, time, velocity, displacement and kinetic energy. The obtained data was processed to assess impact-induced damage resistance based on three parameters: threshold load F_d, peak impact load F_{max}, dissipated energy E_{dis}. Fig. 3.2 is an example of a representative recorded load-time history of the impactor where F_d and F_{max} can be easily identified.

$$v = \sqrt{\frac{2E}{m}} \tag{3.1}$$

Fig. 3.3 shows a photograph featuring the main components of the impact testing facilities. The impact tower houses important components such as the anti-rebound catcher device that prevents repeated impacts, optical sensor that measures the impactor velocity, and the striker-mass carriage system on which additional masses

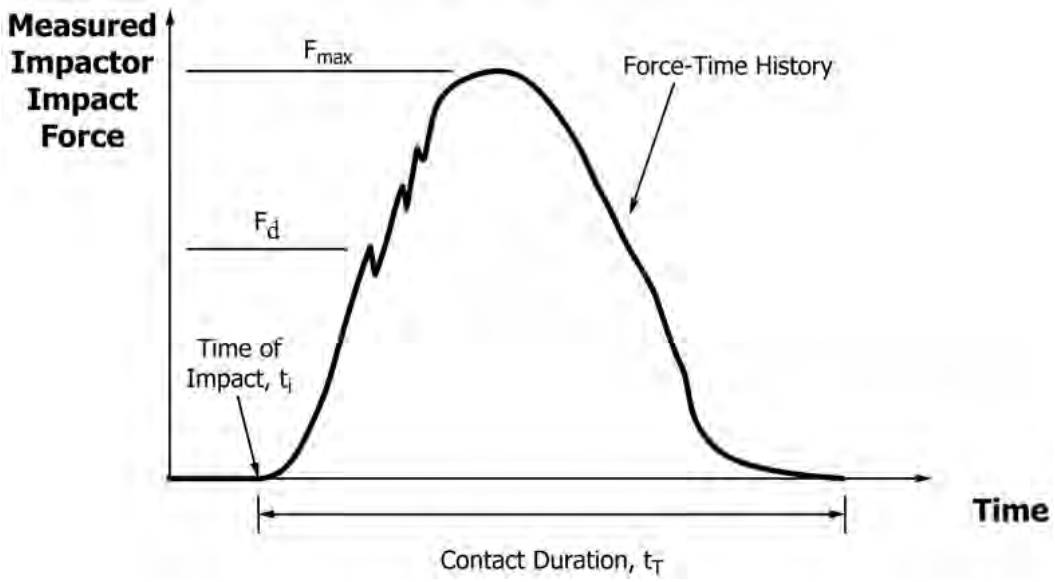

Fig. 3.2: Representative impactor force versus time history; F_d is the impact damage threshold load, adapted from [164].

can be added. The standard impactor geometry with a blunt, hemispherical striker tip of 8 mm in radius was used. Fig. 3.4 depicts the photograph showing the striker-mass carriage system and its necessary components. The test coupon were placed in the test area that hosts the support fixture and the specimen clamping system. Fig. 3.5 sketches of the impact support fixture with the test specimen and the location of the clamps as well as the associate dimensions of the cut-out window.

3.2.2 Quasi-static indentation tests

The quasi-static indentation tests partially followed the test standard ASTM D7136 [164]. In order to reproduce the same setup conditions as those of the low velocity test, the specifications of both the indentation support fixture and indenter followed ASTM D7136 recommendation. The tests were performed with an MTS Insight electromechanic testing machine equipped with a 100 kN load cell at a loading rate of 0.5 mm/min.

Fig. 3.6, taken from Wagih et al. [165], illustrates the instrumented quasi-static indentation test setup. The instrumentation also included a laser displacement transducer MEL M70LL to record the laminate back-face displacement right under the indentation zone.

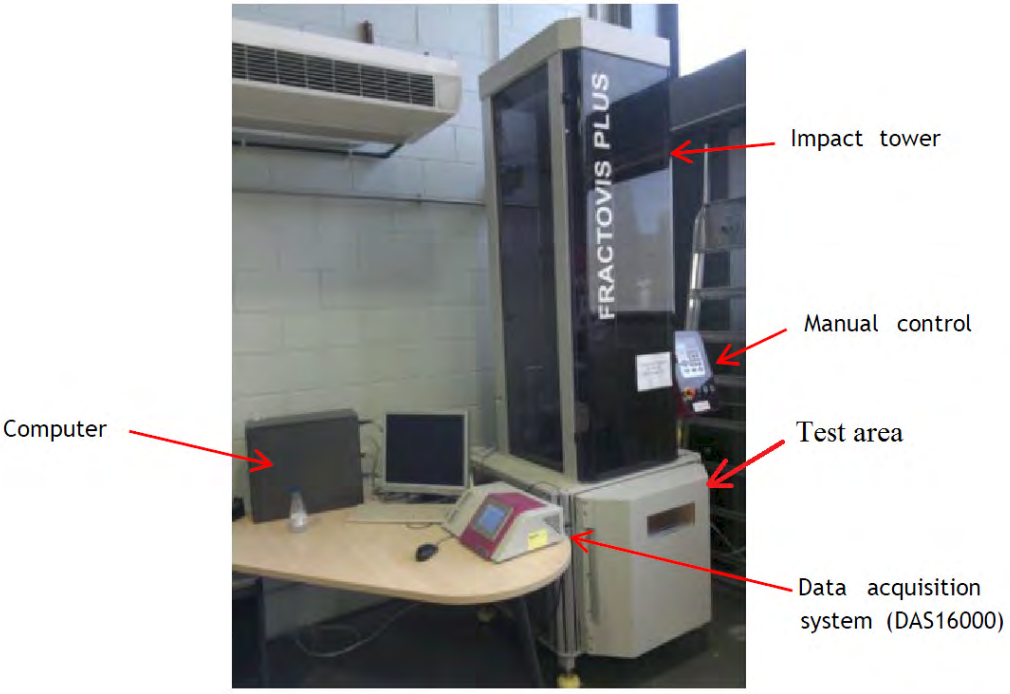

Fig. 3.3: Main components of the impact testing facilities.

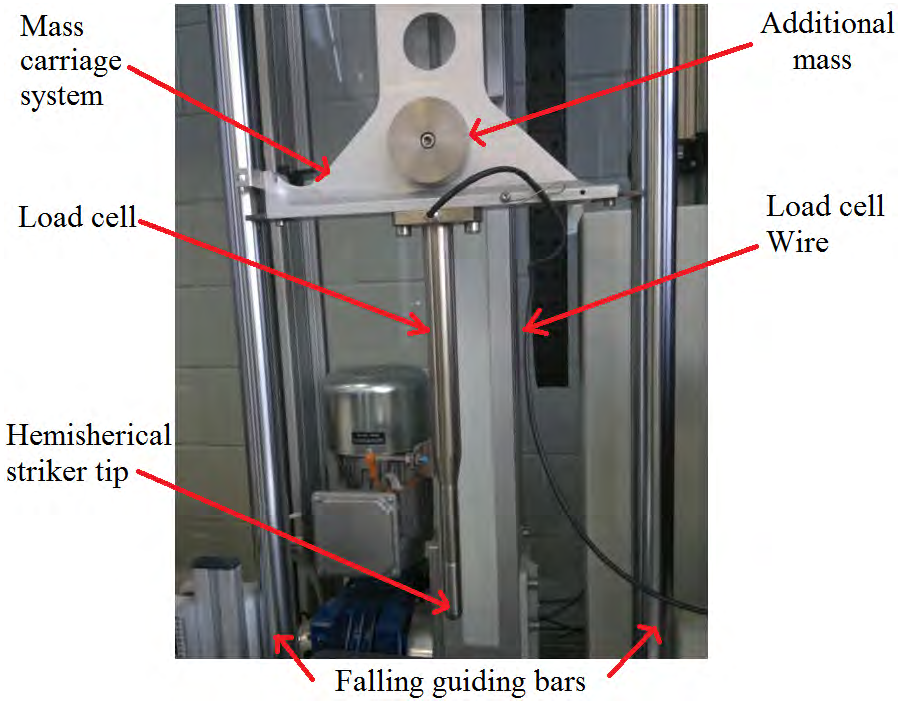

Fig. 3.4: The striker-mass carriage system and its components.

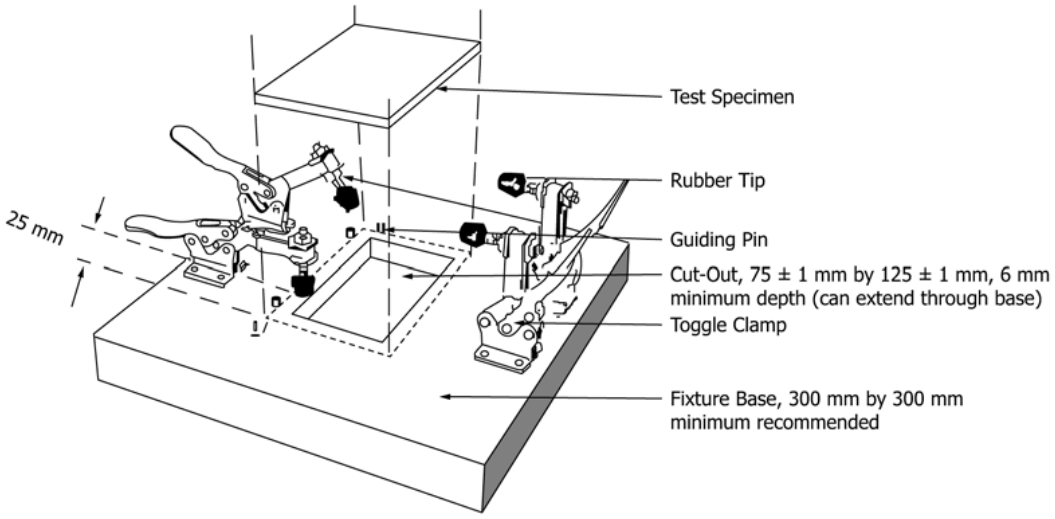

Fig. 3.5: Sketch of the impact support fixture, the test specimen and the location of the clamps as well as the associate dimensions of the cut-out window, taken from [164].

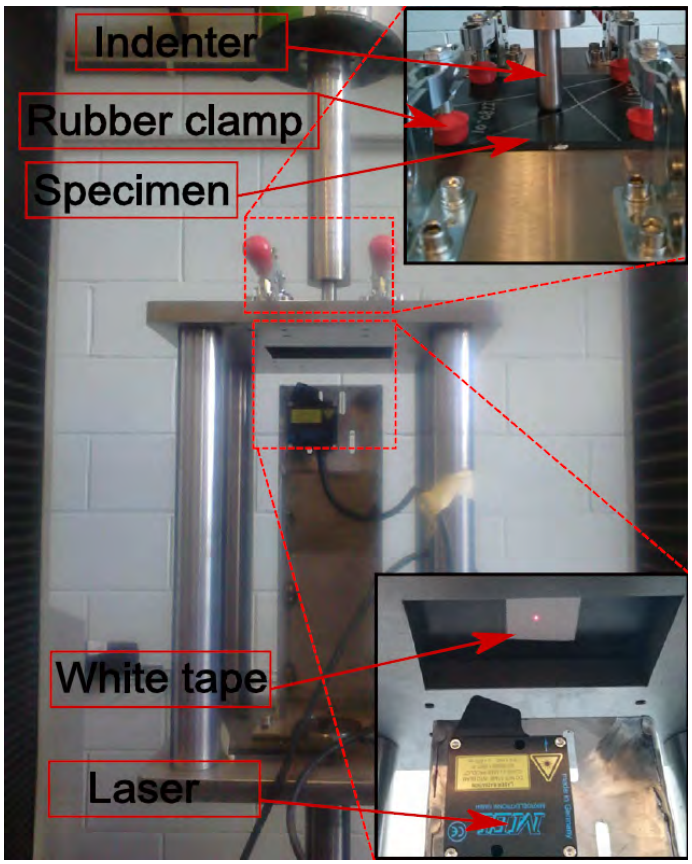

Fig. 3.6: Experimental test setup of quasi-static indentation, taken from Wagih et al. [165]

3.2.3 Compression after impact

Test standard ASTM D7137 [166] was followed for the compression after impact tests. Compression tests of all impacted and non-impacted coupons were performed with an MTS 810 Servo-hydraulic Testing Machine equipped with a 250 kN load cell at a loading rate of 1 mm/min.

To ensure the proper loading alignment in accordance with the test standard recommendation, a steel specimen with two pairs of bonded strain gauges, Fig. 3.7, was compressed up to the recommended strain level of between 2000-2400 micro-strains, where the percent bending B_y was found to be less than 10%, acceptable according to [166]. The value of B_y was calculated according to Equation 3.2, where the convention of the gauge positions followed those indicted in Fig. 3.7. The percent bending was calculated for both pairs of the strain gauges; i.e. left pair (G1-G3) and right pair (G2-G4), see Fig. 3.7. Note that when Equation 3.2 was applied to the left pair, the strain ε_1 was replaced by ε_2 and ε_3 by ε_4

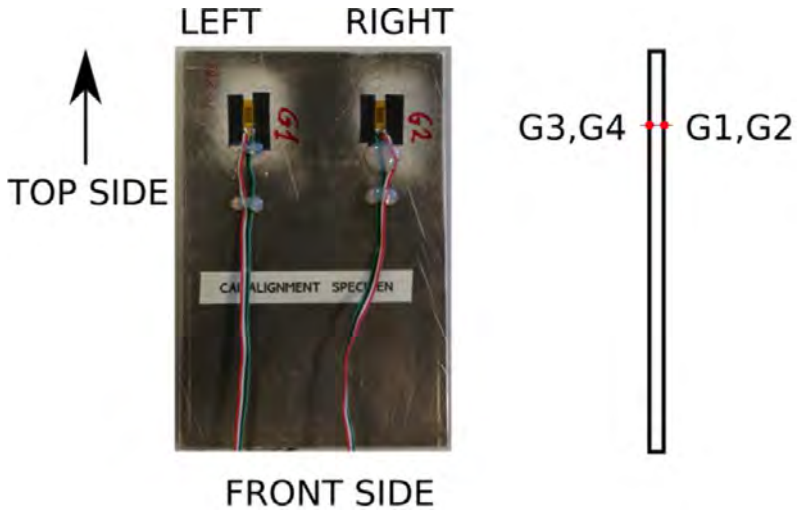

Fig. 3.7: Photograph showing the steel specimen with two pairs of bonded strain gauges, G1-G3 and G2-G4, each having 6mm in gauge length for ensuring proper alignment.

$$B_y = \frac{\varepsilon_1 - \varepsilon_3}{\varepsilon_1 + \varepsilon_3} \tag{3.2}$$

The composite specimens were instrumented with two linear transducers to measure the out-of-plane displacement at the impacted location, Fig. 3.8. Load-displacement curves were recorded for each test during the loading process. The compression after impact strength σ_{CAI} was determined with Equation 3.3, where P_{max} is ultimate load and A the cross-sectional area of the specimen. P_{max} can be identified from the load-displacement as shown in Fig. 3.9.

$$\sigma_{CAI} = \frac{P_{max}}{A} \tag{3.3}$$

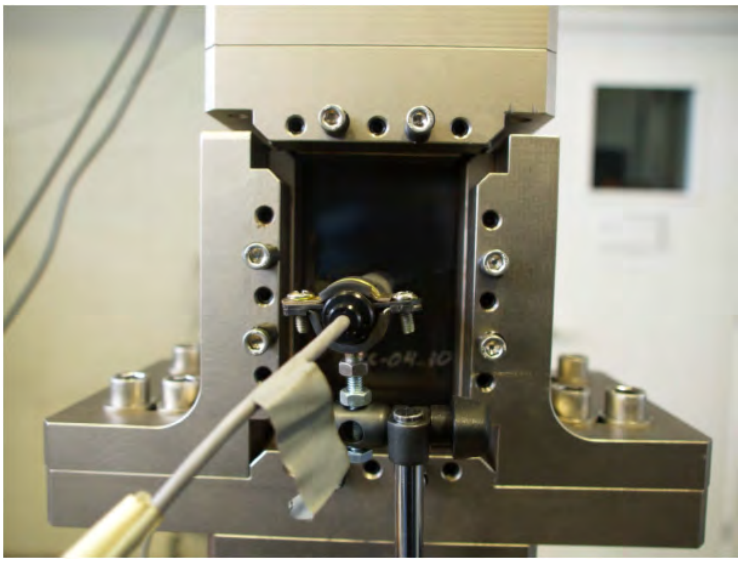

Fig. 3.8: Photograph of the linear displacement transducer placed on one side test specimen for out-of-plane displacement measurement, taken from [167].

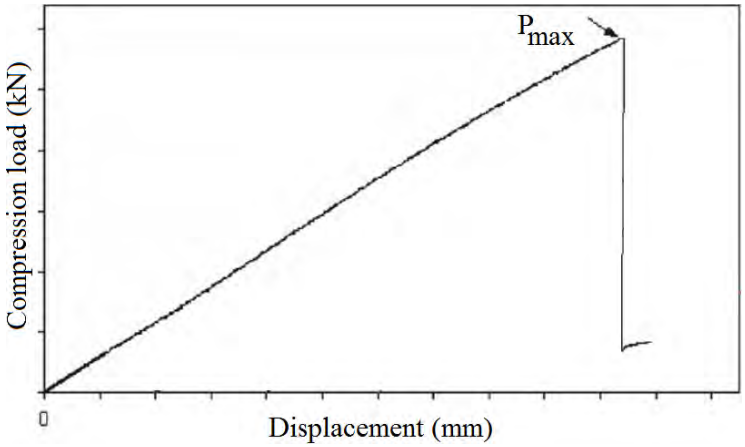

Fig. 3.9: Representative load-displacement curve recorded during compression after impact loading process

3.3 Damage inspection

3.3.1 Permanent indentation

The indentation depth δ_{ind} was measured using a Mitutoyo digital dial depth gauge of 0.001 mm precision, see Fig. 3.10a. For each impacted specimen, two indentation measurements at the impacted location were made: one by placing the gauge arms parallel to the specimen length (d_1) and the other parallel to the specimen width; i.e. d_1 and d_2 in Fig. 3.10b. These measurements were taken within less than 20

min after the impact test, and the indentation depth δ_{ind} was taken as the average of the two measurements. To facilitate the measurements, a steel frame was used to support the specimen as shown in Fig. 3.11.

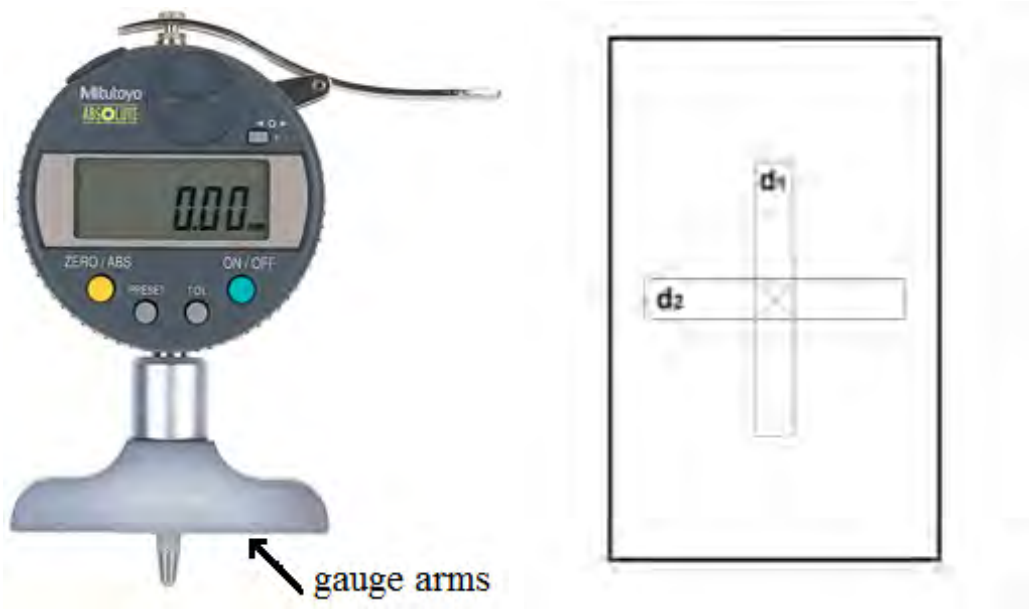

(a) **(b)**

Fig. 3.10: (a) Digital dial dent gauge used for indentation depth measurement, and (b) Schematic illustrating locations of how the gauge arms were placed during the measurement.

Fig. 3.11: Photograph showing the steel frame used to facilitate indentation depth measurements; left: frame without specimen, and right: frame with specimen.

3.3.2 C-Scan inspection and damage area

The damaged area was inspected with a non-destructive ultrasonic C-Scan(OLYMPUS OMNISCAN MX). Fig. 3.12 shows the scanning facilities with the main components. The robotic arm was controlled to move over the scan area with a PC-based soft-

ware Robotporticado. The probe used was 9.525 mm in diameter and 5 MHz in frequency.

Each impacted specimen went through two C-Scan inspections: one for the impacted face and the other for the non-impacted face. The projected damage area A_{pro} was taken as the mean value of the projected delamination areas from the two C-Scan inspections by means of Inkscape free software.

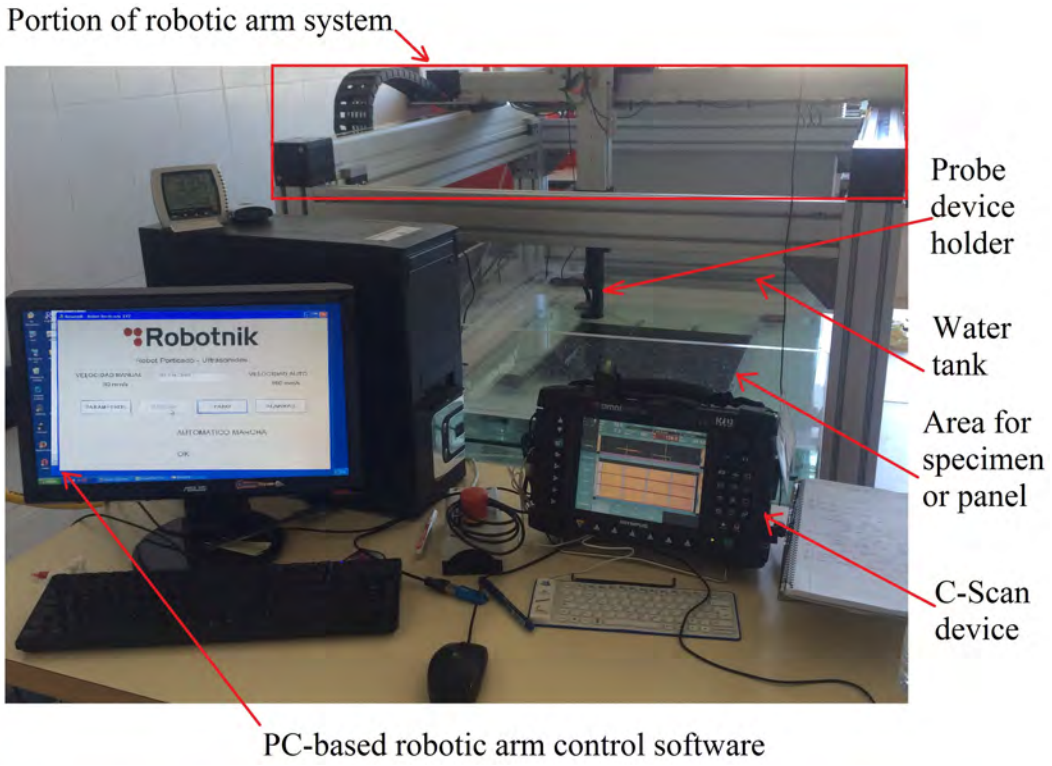

Fig. 3.12: Photograph showing the ultrasonic scan facilities comprising of the main components.

3.3.3 Computed X-ray tomography

To reveal different damage modes at the micro-scale, miro-Computed X-ray tomography (μCT) was used to inspect the damaged region induced by quasi-static identation tests. The inspection facilities include an X-Ray source with the maximum power of 20 W and focal spot of 5 microns, and a detector of 2400 x 2400 pixel. The source and detector were manufactured by HAMAMATSU and assembled by Novadep Scientific Instruments. Depending on the desirable field of view required to achieve a good resolution, two groups of μCT imaging conditions, as summarised in Table 3.2, were used to inspect the selected test coupons (see Table 5.1). In Table 3.2, the sample width is the length of the specimen central portion cut along the specimen length, Fig. 3.13. For each coupon under the inspection, a total number of 1600 projections were acquired while the sample was rotating in 360°. The medical

Tab. 3.2: Imaging conditions for μCT of two fields of view.

Imaging conditions	Group A	Group B
Field of view (mm)	13.44	40.32
Sample width (mm)	19-10	30
Energy (kV)	55	60
Gun current (μA)	80	70
Voxel resolution (μm^3)	6	18
Exposure time (s)	15	12

software Starviewer was used to render the acquired 3D image in the postprocessing.

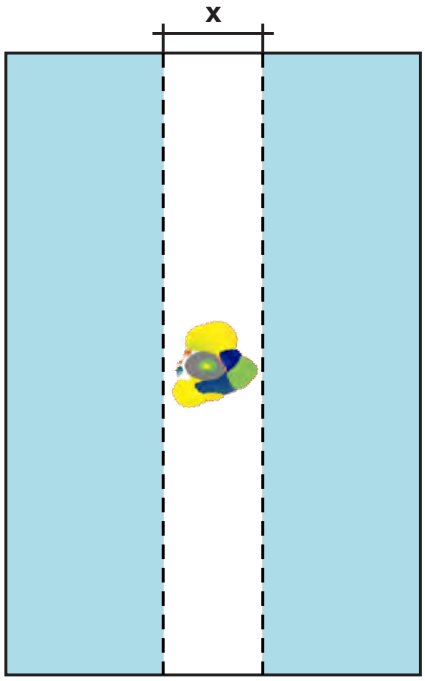

Fig. 3.13: A representative sketch showing the sample width X.

3.4 Experimental sequence

First, the specimen dimensions were measured. Prior to the impact tests, ultrasonic C-Scan inspections were performed to detect any premature damage caused during cutting and handling. No damage was observed from the inspection. Therefore, for brevity, the results at this stage of the test campaign are excluded from the thesis.

The test sequence afterwards can be summarised in the following order:

1. Perform impact tests with the CEAST Fractovis Plus drop-weight impact test machine (see Section 3.2.1), or quasi-static indentation test (see Section 3.2.2).

2. Measure the indentation depth with a Mitutoyo dial depth gauge and support frame described in Section 3.3.1.

3. Subject each specimen to C-Scan inspections twice: one for the impacted face and the other for non-impacted face as previously mentioned (Section 3.3.2).

4. Perform X-ray computed tomography as described in Section 3.3.3; this step involves only specimens tested under indentation.

5. Run the compression tests for both pristine and impacted specimens (Section 3.2.3). Indentation test coupons were not subjected to test because they were cut for high resolution tomography inspection.

3.5 Conditioning and testing of WET specimens

Three batches of each layup, referred to as WET in Table 4.2, were conditioned at 80°C/85% RH inside a CTS conditioning chamber until equilibrium state, following the EN2823 protocol [168]. After 2000 hours of conditioning, equilibrium state of approximately 1.26% weight gain was reached.

The sequence of tests from impact to CAI was the same as those described in Section 3.4 with the only difference being in how the WET specimens were handled after each impact test prior to CAI. The total duration of an impact test and indentation measurement was less than 10 minutes, after which the specimen was returned to the chamber. Next, each specimen was subjected to the C-Scan inspection from impacted and non-impacted faces for less than 30 minutes and then put back into the chamber. This process was repeated for all the WET specimens to ensure that they lost about the same amount of moisture while they were outside the conditioning chamber. Before the specimens were compression tested, they were kept in the conditioning chamber for much more than two weeks so that they could regain the moisture content.

3.6 Numerical model

To understand the influence of a delamination in terms of its sizes and through-the-thickness position on the compressive strength, a parametric study was conducted using FEM. The numerical model was created using ABAQUS Python Scripting. ABAQUS/Explicit was selected because it was observed, through trials and errors, that ABAQUS/Standard experienced convergence difficulties. The model was parameterized such that changes could be easily made to some of its important features such as:

- Diameter of the delamination,
- Through-the-thickness position of the delamination,
- Dimensions of the specimen,
- Layup of the specimen, and
- Mesh size.

3.6.1 Geometry and boundary conditions

The specimen has the same dimensions as the impact coupon recommended in ASTM D7136 [164]; i.e. 150 mm in length and 100 mm width with 0°-ply aligned in parallel to the longer dimension, see Fig. 3.1 of Section 3.2.1. The boundary condition mimics that of CAI test following the recommendations of the test standard. Fig. 3.14 represents both the geometry and the boundary conditions, in accordance with the CAI test setup of ASTM D7137 [166].

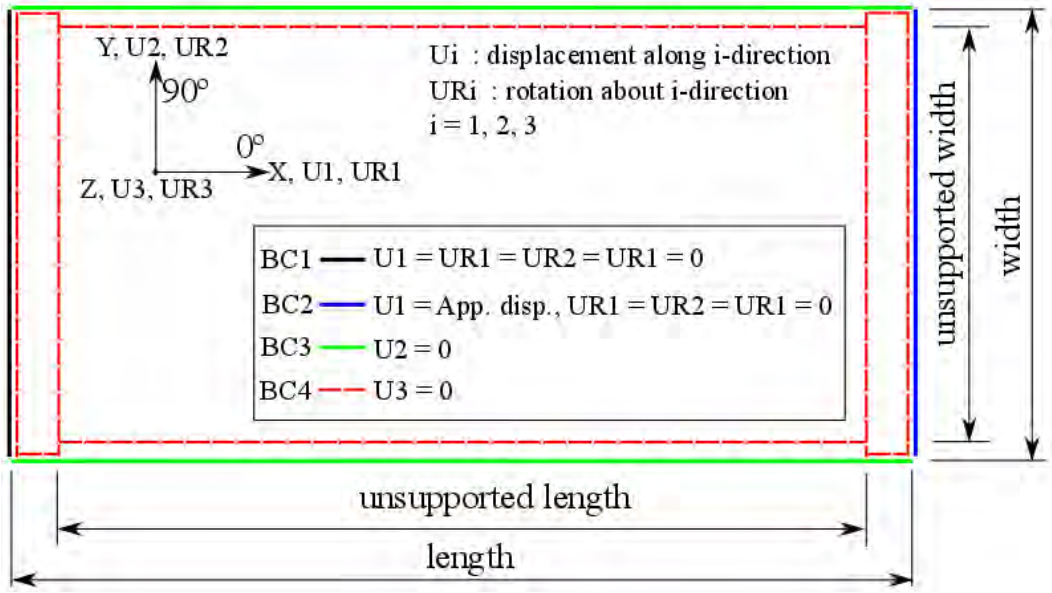

Fig. 3.14: Representative geometry and boundary conditions of the FE model; Ui and URi: translation and rotation degree of freedom along and bout the axis; App. displ.: applied displacement a long the loaded edge; Z-axis: out-of-the plane direction (or through-the-thickness direction of the laminated plate).

Fig. 3.15 illustrates the side view of the FE model of a delaminated laminate of 24 plies. The laminate is divided into top and bottom sublaminates by a delamination. The sketch exemplifies the delamination located at the 11^{th} interface from the laminate top surface, and is denoted as Int11. This notation of location is used for presenting the results throughout Chapter 6. If the location of the delamination is at the first interface from the surface instead of the 11^{th} interface, the notation is

changed to Int1 and so on. Each sublaminate is modelled with a composite layup. Each vertical arrow (upper and lower) represents the contral point of the laminate top and bottom surfaces where the out-of-plane displacement can be output.

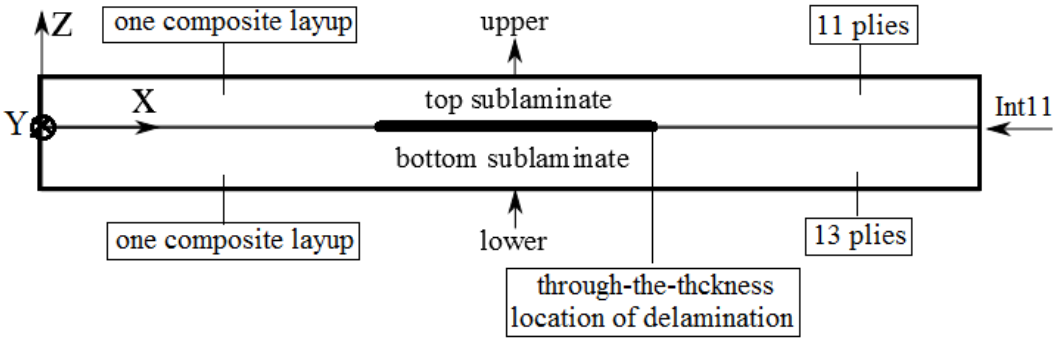

Fig. 3.15: Sketch showing the side view of the model consisting of the top and bottom sublaminates divided a central delamination located at the 11^{th} interface, denoted as Int11, for a 24-ply layup.

3.6.2 Material behaviour and constants

In this FE model, only two damage modes are considered considered: delamination and brittle fibre breakage. These two failure modes were modelled using the built-in capabilities of ABAQUS for interlaminar and intralaminar failures. The interlaminar failure (i.e. delamination initiaton and propagation) was simulated with VCCT by defining, inside the interaction module, the interaction property and assigning the property to the interface with initial delamination. To simulate the propagation of the delamination under mixed-mode loading, the Benzeggagh-Kenane (BK) criterion was used, with BK-exponent η=1.45. To avoid penetration hard contact was assigned in the areas of the initial delamination and expected propagation, Fig. 3.16.

The fibre breakage was modelled by means of the continuum damage model based on Hashin's failure criteria using the material definition module. This damage behaviour was assigned to the entire specimen, i.e. regions both inside and outside the initial delamination area. The lamina elastic properties used to model elastic behaviour are those presented in Table 3.1. Other material constants used in the FE model are listed in Table 3.3. Note that the values of $G^C{}_{ft}$, $G^C{}_{fc}$, $G^C{}_{mt}$, and $G^C{}_{mc}$ are assumed in order to cause completely brittle behaviour of fibres. This assumption was made to avoid the progressive failure process, which thus helps to reduce the computational time for a big number of simulations. A one-element FE model on tension and compression response confirmed this desired behaviour, see Fig. 3.17. Another set of assumed material constants are Y_T, Y_C, S_L and S_T. Both sets of assumed values allows the brittle failure of fibres to be simulated in Hashin's failure criteria of ABAQUS. It is important to point out that the model that

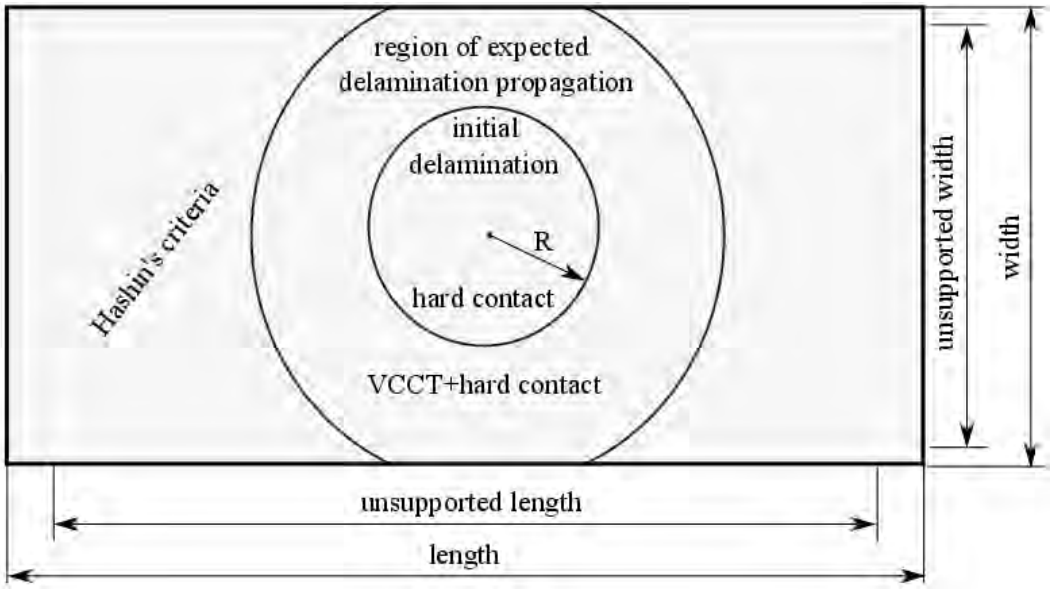

Fig. 3.16: In-plane view of the FE model showing regions where particular material behaviours are assigned.

Tab. 3.3: Material constants considered in the numerical study of embedded delamination.

Property	Unit	Value	Description
G_{Ic}	N/mm	0.280	Interlaminar fracture toughness under mode I
G_{IIc}	N/mm	0.790	Interlaminar fracture toughness under mode II
X_T	MPa	2290.5	Longitudinal tensile strength of the lamina
X_C	MPa	1051.0	Longitudinal compression strength of the lamina
Y_T	MPa	10^6	Transverse tensile strength of the lamina
Y_C	MPa	10^6	Transverse compression strength of the lamina
S_L	MPa	10^6	Longitudinal shear strength of the lamina
S_T	MPa	10^6	Transverse shear strength of the lamina
G^C_{ft}	N/mm	10^{-6}	Energy dissipated during fiber tension failure
G^C_{fc}	N/mm	10^{-6}	Energy dissipated during fiber compression failure
G^C_{mt}	N/mm	10^{-6}	Energy dissipated during matrix tension failure
G^C_{mc}	N/mm	10^{-6}	Energy dissipated during matrix compression failure

considers only delamination exhibits no clear load drop, thus making identification of the failure point unclear.

3.6.3 Element type and mesh consideration

Two types of conventional shell elements are initially considered in order to check both the computational efficiency and accuracy. These elements were the four-node full integration S4 and reduced integration S4R, available in the ABAQUS 6.12 library. Fig. 3.18 compares delamination growth predicted by models with S4 and S4R elements at the instant of the propagation onset and of propgagation reaching the unsupported width (the dash lines along the specimen length in Fig. 3.14). The global responses of reaction force vs applied displacement at the loaded edge, and

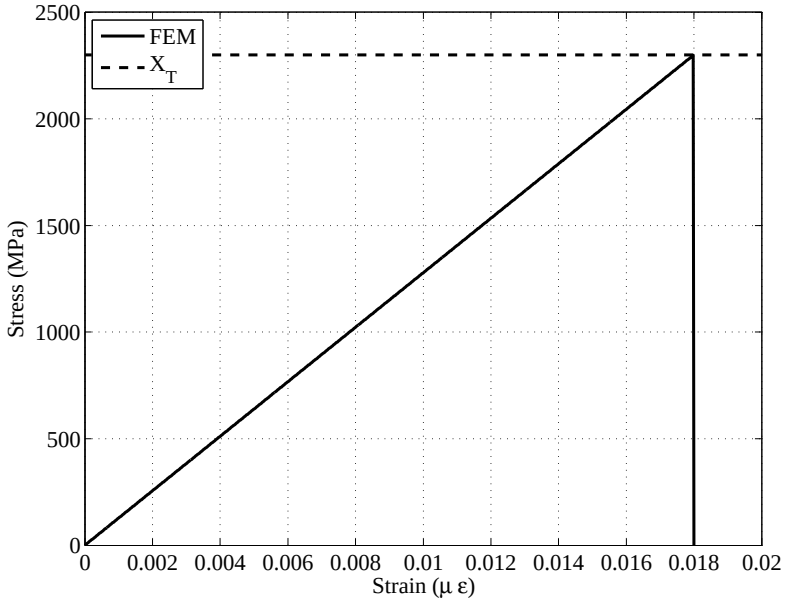

(a) Compression response

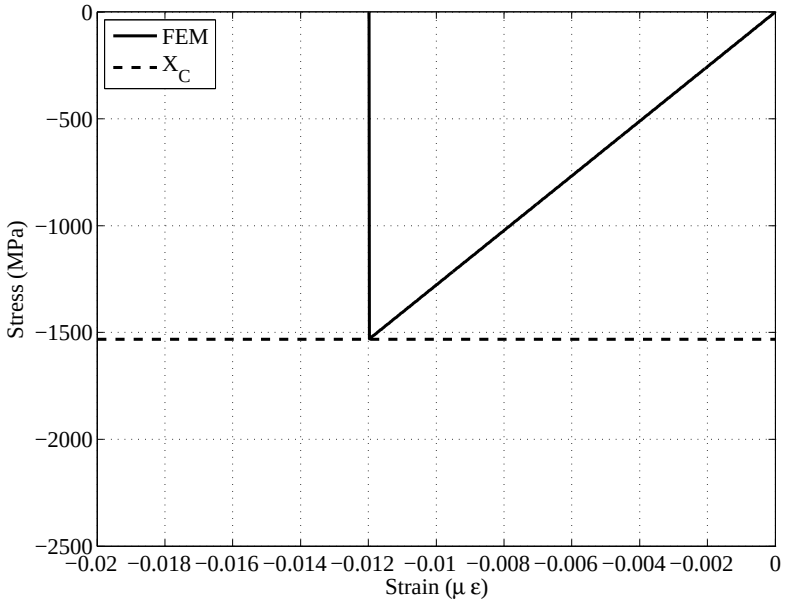

(b) Compression response

Fig. 3.17: One element constitutive response for tension and compression loading cases tested on S4R element: X_T and X_C are taken from experiments and used as inputs into the model.

.

Tab. 3.4: Computational time of S4 and S4R under varying mesh sizes.

Radial mesh size (mm)	S4 Time (min)	S4R Time (min)
2.00	7	5
1.50	12	6
1.00	44	21
0.75	59	26
0.50	178	57

local response of reaction force vs out-of-plane displacement of upper and lower sublaminates are presented in Fig. 3.19. The large markers in the direction of increasing strain indicate when the sublaminate buckles, when the delamination propagation onset occurs, and when the delamination growth reaches the knife edge, respectively, as predicted by the FE model. The rectangular boxes in the direction of increasing strain mark sublaminate buckling and propagation onset, respectively, observed in the experimental test. The results in both Figs. 3.18 and 3.19 were from the angular mesh size of 2 mm along the perimeter of the initial delamination (silver color) and the constant radial mesh size of 2 mm. The results from the two elements clearly show no difference and are reasonably good agreement with the experimental tests reported in [169]. Different cases were run to assess the advantage of the computational time saving of S4R over S4, of which results are summarized in Table 3.4. Given the advantages in computational efficiency and accuracy, only S4R was considered in the rest of the study.

Three types of meshes were initially explored, see Fig. 3.6.3 for meshes in one quarter of the specimen. Type I mesh did not show good propagation behaviour due to the presence of the abrupt mesh transition along the largest perimeter, which did not allow for further crack advance, see Fig. 3.21. Type II mesh was anticipated to be the remedy of the first case but resulted in the decreasing-increasing trend of the failure loads as the delamination diameter normalized by the specimen width was increased from 0.25 to 0.50 and to 0.75 for many cases. This unexpected trend can possibly be attributed to the limitation in the mesh design where the polar mesh pattern could not offer the full control over the regions around which boundary conditions were applied (bounded by red for Type II). It is reasonable to anticipate that the failure loads monotonically decrease when delamination size increases. Contradicting the intuition, this mesh was not considered for the parametric study, and the final mesh pattern was Type III.

The final mesh size used to obtain the results presented in Chapter 6 is the square mesh of 1x1 mm all over the entire area of the specimen. This size was selected based on the results of the mesh pattern type II, considering the convergent study of the load level at which delamination growth onset occurred, see Fig. 3.22. In

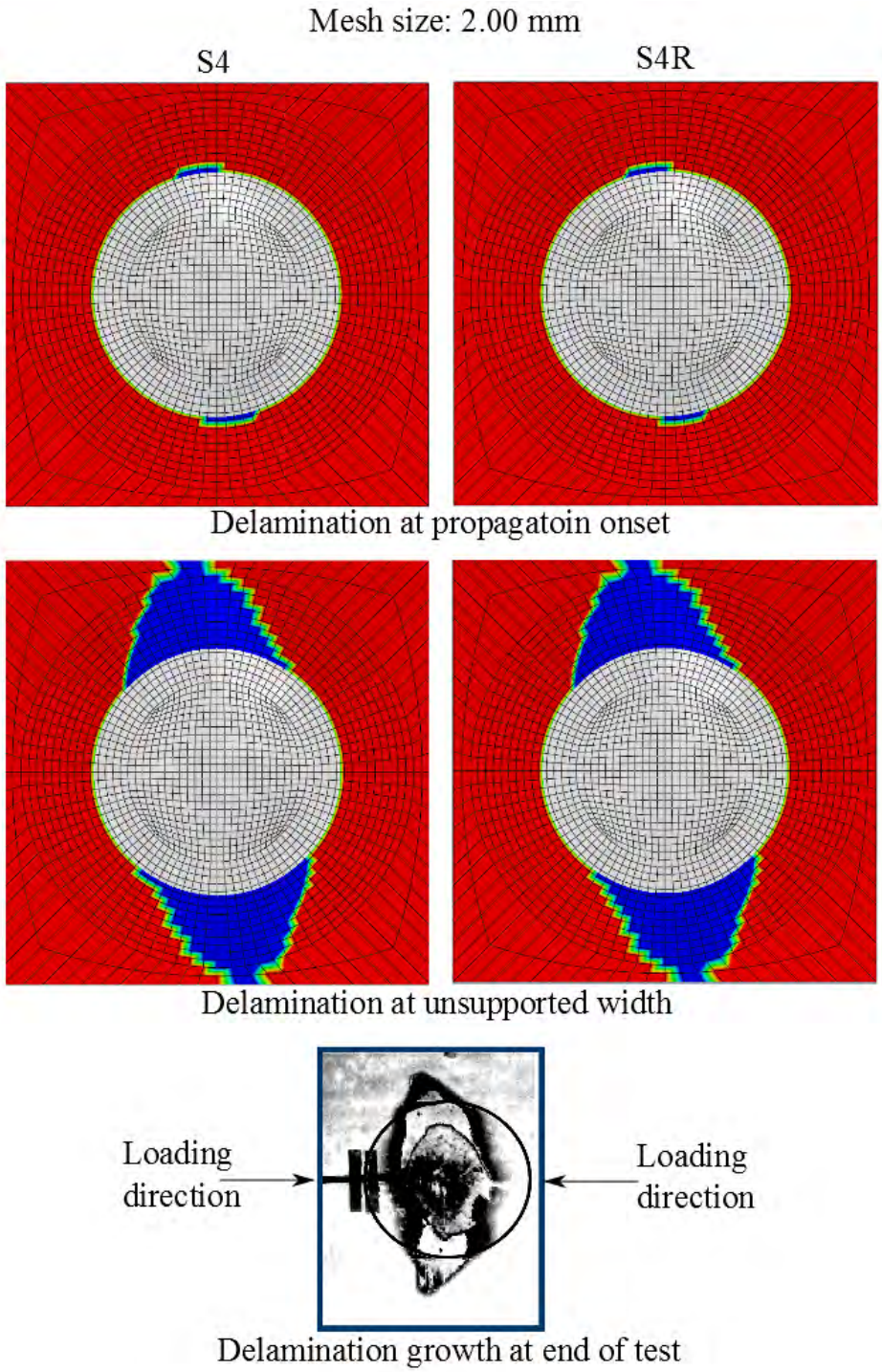

Fig. 3.18: Delamination growth direction for S4 and S4R, and experimental delamination growth direction obtained from X-ray inspection as reported in [169].

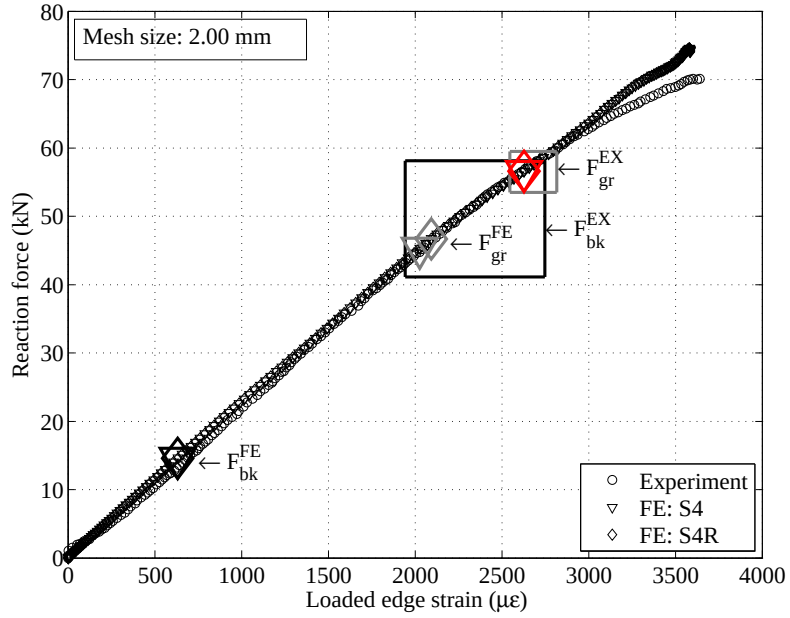

(a)

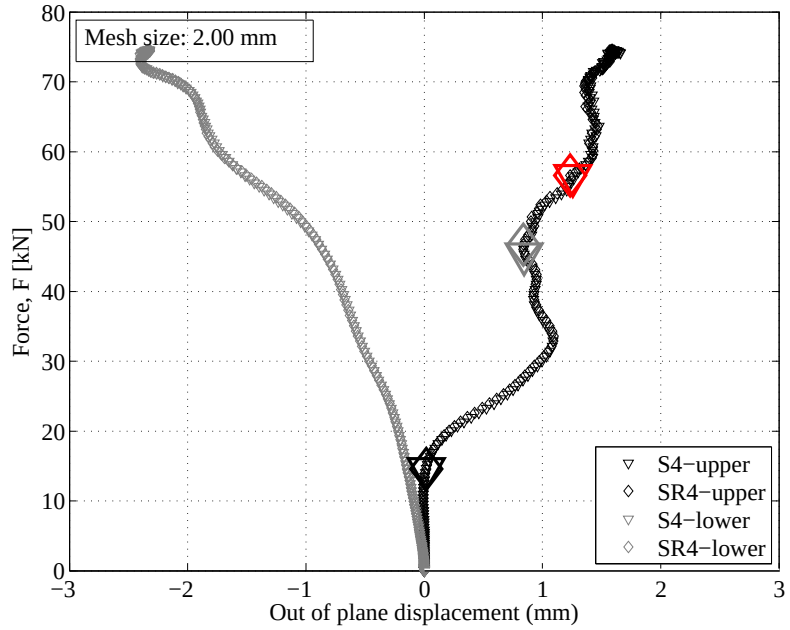

(b)

Fig. 3.19: Comparison of the responses obtained with S4 and S4R FE models: (a) reaction force vs applied strain at the loaded edge, and (b) reaction force vs out-of-plane displacement of upper and lower sublaminates. F_{bk}^{FE} and F_{gr}^{FE} sublaminate buckling and delamination growth onset loads predicted in FE model in the validation study. F_{bk}^{EX} and F_{gr}^{EX} are sublaminate buckling and delamination growth onset loads experimentally determined in [169].

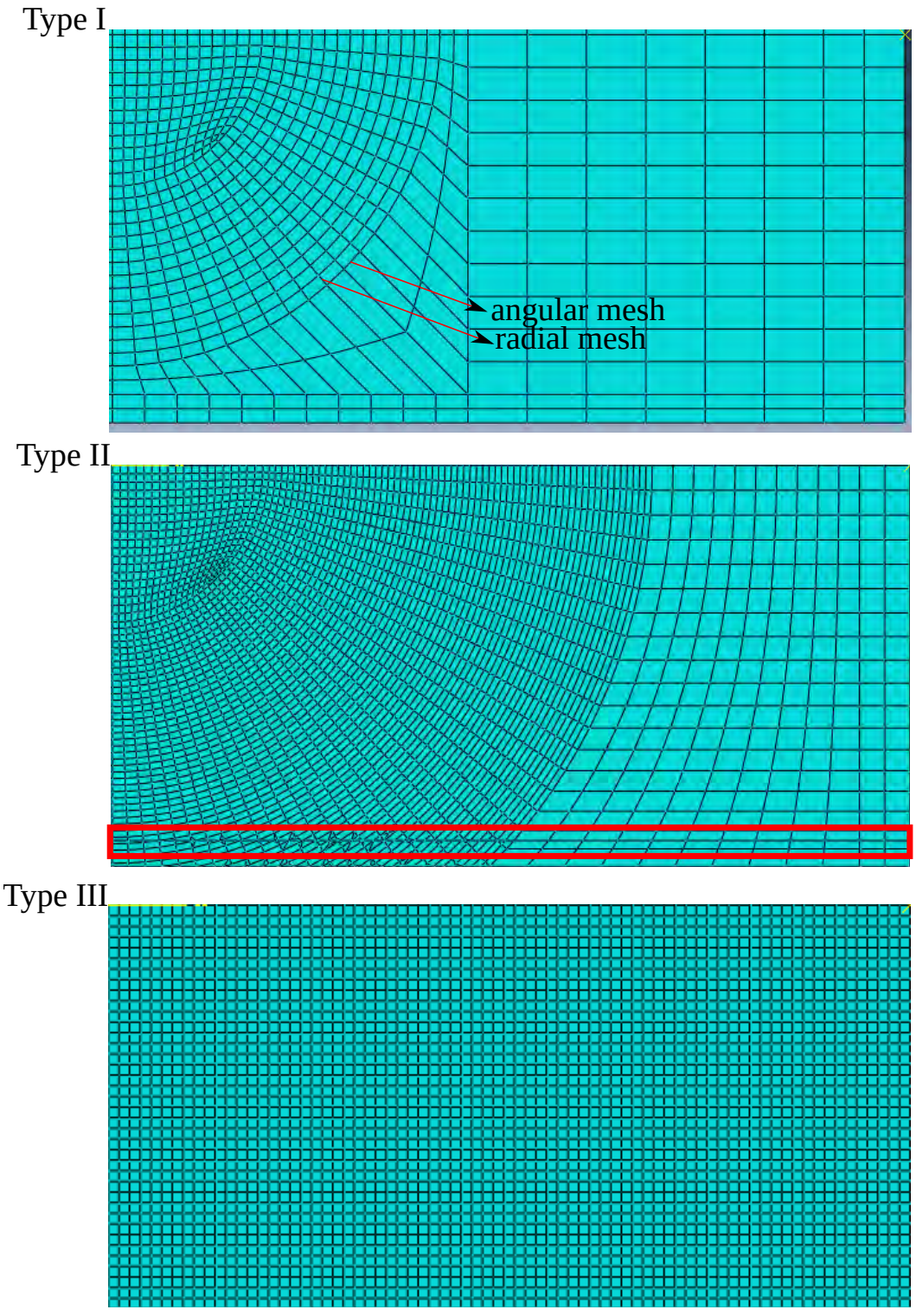

Fig. 3.20: Three types of meshes initially explored to decide the final mesh configuration.

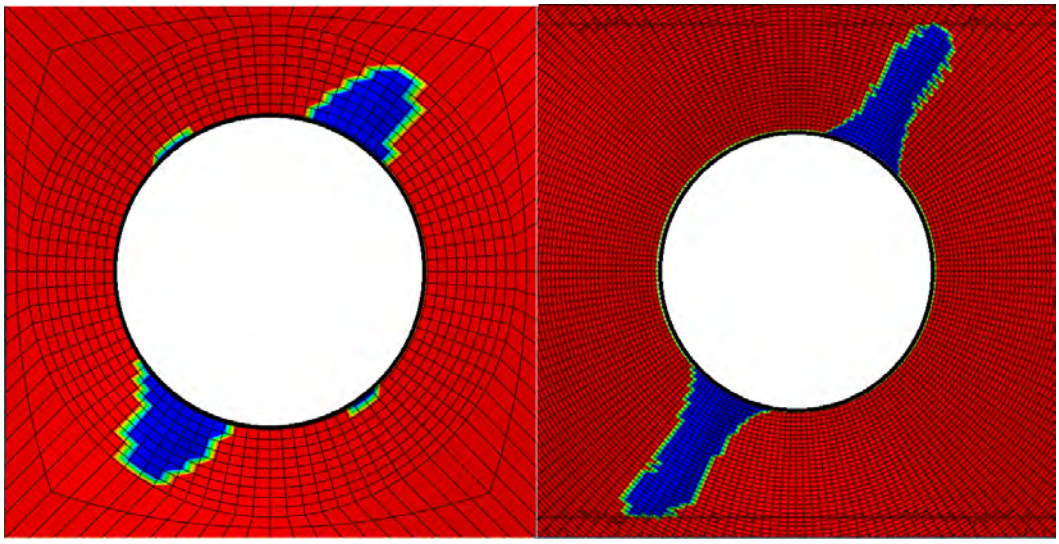

Fig. 3.21: Delamination growth extension for Type I (left) and Type II (right).

Fig. 3.22, $\Delta\theta$ represents the angular mesh and ΔR the radial mesh as shown in the example of mesh Type I of Fig. .

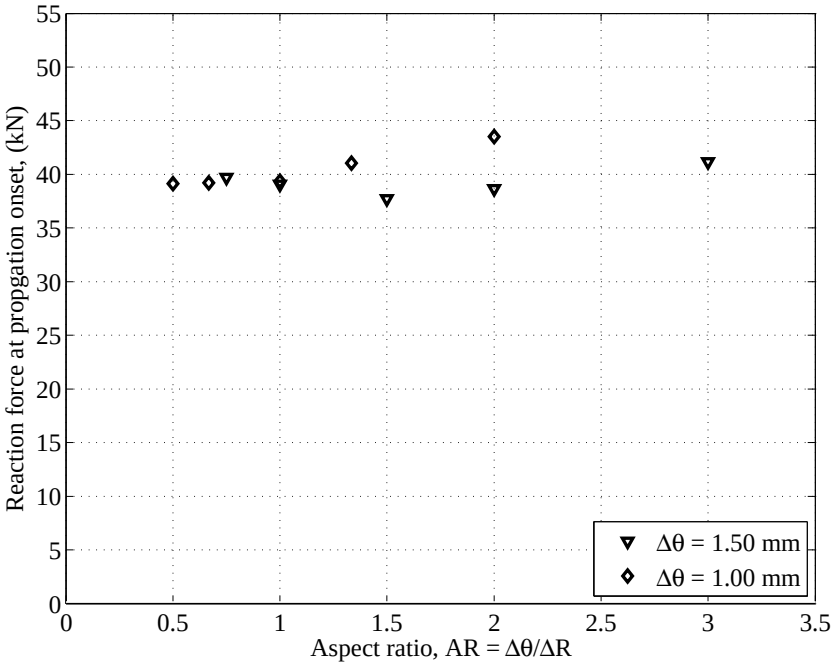

Fig. 3.22: Load at propagation onset against different mesh sizes at the delamination front of mesh Type II. $\Delta\theta$ and ΔR are angular and radial mesh respectively.

Part III

Results and Discussion

4 CAI strength of conventional and nonconventional laminates

4.1 Overview

Departing from the hypothesis that compression after impact (CAI) strength is impaired by the presence of delaminations, a nonconventional ply sequence was defined by selecting the mismatch angles between plies so as to maintain a central sublaminate with no, or small, delaminations resulted from a low velocity impact (LVI) event. The main aim of this chapter is to experimentally validate this hypothesis, which was expected to improve the CAI strength with respect to a traditional quasi-isotropic baseline laminate. Also discussed here is the effect of blocking plies and moisture on the CAI strength. The content of this chapter meets the first objective stated in Section 1.3, and partially fulfills the fourth and fifth objectives of the same section regarding the out-of-plane and CAI loading. The test methods used for LVI, damage inspection and CAI were described in Sections 3.2.1, 3.3.2 and 3.2.3 respectively.

4.2 Rationale behind the selected layups

4.2.1 Baseline laminate (LBA)

The stacking sequence of the baseline laminate LBA is $[90/\text{-}45/0/45\,]_{3s}$, which differs slightly from the layup recommended by the standard test ASTM D7136M-12 [164] ($[45/0/\text{-}45/90]_{ns}$). The LBA ply sequence has 90° ply on the laminate surface, a constant MMA value of 45° between adjacent plies and no blocking of plies (except those above and below the midplane, i.e. MMA=0°). Placing the 90° ply as the outermost ply has been considered in some past studies and proven to be more impact resistant than having a $\pm 45°$ ply on the surface [19], and to enhance buckling strains [170] and CAI strength [171].

4.2.2 Nonconventional laminate (LNC)

The aim to control the through-the-thickness location and size of the delaminations created in a low velocity impact by means of the mismatch angle between plies is the novelty of this study. As shown in Fig. 4.1, the LNC laminate is divided

into three sublaminates: top, central and bottom. Our intention is to promote large delaminations at the bottom sublaminate and leave the central one mostly undamaged. This almost-pristine central sublaminate would account for an increase on the buckling strain as compared to a laminate where delaminations would be evenly distributed. This approach relies on previous findings that large MMA located close to the non-impacted face (specimen's bottom) results in large delaminations [15]. Therefore, large MMA values ($\geq$45°) were imposed on all the interfaces within the bottom sublaminate. Large MMAs also appear within the top sublaminate due to the symmetry constraint. On the other hand, a constant MMA of 15° was imposed on all the interfaces within the central sublaminate so as to prevent large delaminations from occuring in this region.

The aim of this approach is to dissipate the impact energy through large delaminations predetermined to appear at the bottom sublaminate. The rest of the laminate would be left with smaller delaminations thus, CAI strength is expected to be enhanced.

To avoid the differences in stiffness hiding the effect of the stacking sequence definition, both LNC and LBA were defined as having the same in-plane elastic properties. In addition to the aforementioned requirement, the following features of the LBA were regarded as constraints: same number of plies (24) and non-zero MMA (22), symmetry, balance, and quasi-isotropy. The LNC layup is [90/-45/75/-60/60/-75/-30/-15/0/15/30/45]$_s$, obtained by means of the Ant Colony Optimization (ACO) algorithm [16]. Note that the number of 0° plies is one-third that of the baseline.

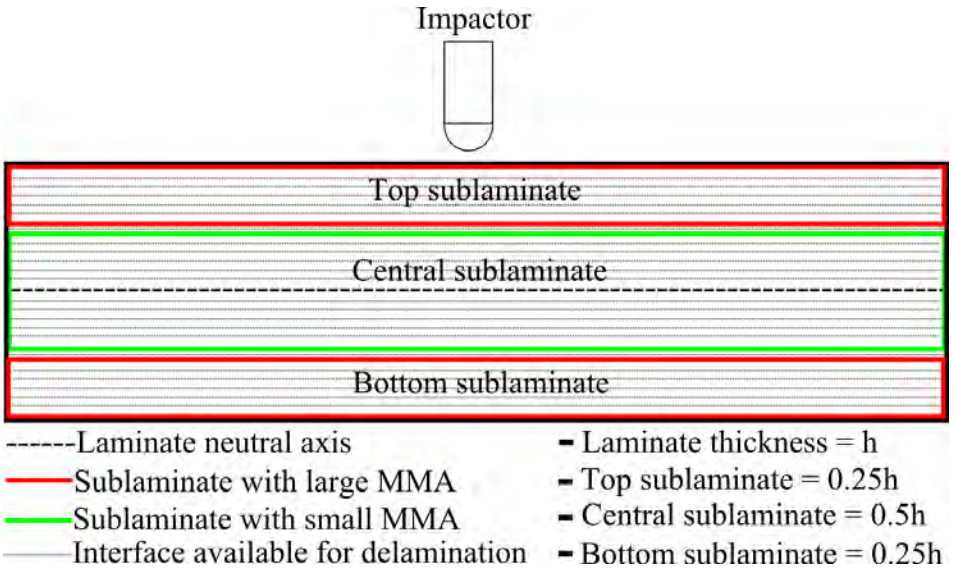

Fig. 4.1: Through-the-thickness view illustrating definition of the tailored nonconventional laminate (LNC) comprising of three sublaminates: top and bottom sublaminates with large MMAs of 45-60° and central sublaminate with small MMAs of 15°.

4.2.3 Thick-ply laminate (LTP)

The stacking sequence of the thick-ply laminate is $[90_3/\text{-}45_3/0_3/45_3]_s$, obtained by blocking plies of the same orientations. Note that ply thickness in this layup is three times that of the LBA, and a cluster of six $45°$ plies is inevitable due to symmetry. Another important aspect is the reduction in the number of interfaces (potential sites for delamination) from 22 in the LBA to 6 in the LTP.

4.3 Laminate elastic constants

The stacking sequence of each layup, as well as the MMA values, are presented in Table 4.1. Note that the three layups are quasi-isotropic, and all their in-plane elastic properties are constrained to be the same. Using the classical laminate theory and the ply elastic properties listed in Table 3.1 yields Young's modulus of 57.25 GPa, shear modulus of 21.68 GPa, and Poisson's ratio of 0.32. In the layup design, the equivalent bending stiffness D^*, an elastic parameter commonly used to assess the stiffness of an infinite composite plate under out-of-plane loading [172], was not constrained. However, its values for the three layups are reported here for completion. The D^* values of the three layups along 0°, calculated according to [173], differ by less than 10% (Table 4.1)

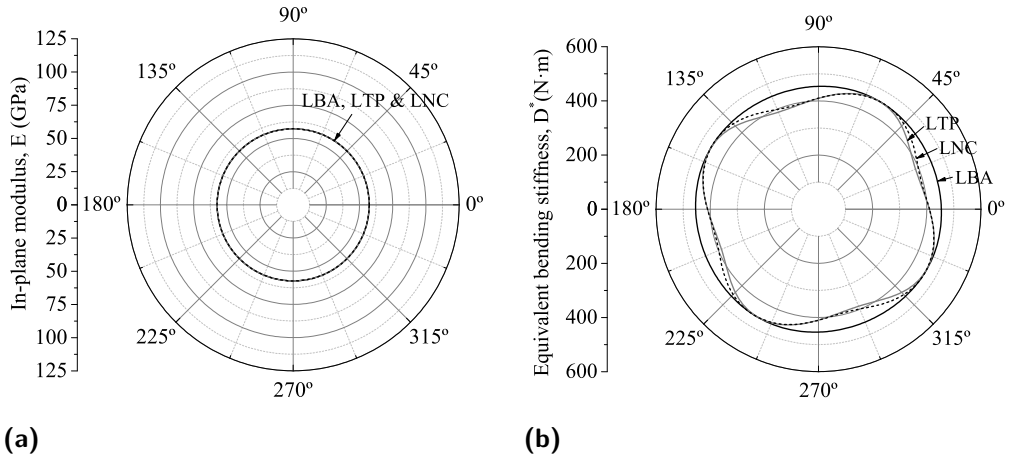

Fig. 4.2: Young's modulus (a) and equivalent bending stiffness (b). LBA: Baseline, LNC: Nonconventional, and LTP: Thick-ply.

4.4 Test matrix

The test matrix in this study is presented in Table 4.2, in which AR refers to "As Received" specimens and "WET" to specimens conditioned in a climatic chamber. Pristine/non-impacted coupons of each layup were also tested under compression for reference. Specimen conditioning and tests were conducted in the mechanical

Tab. 4.1: Stacking sequences and mismatch angle (MMA) of two adjacent plies; ply count: total number of plies; int count: total number of interfaces with non-zero MMA; ply thickness: 0.184 mm; *: interface at the midplane. Equivalent bending stiffness (D^*) values presented here are along 0°.

Laminate labels and stacking sequences				
Laminate	Decription	Ply/Int count	Stacking sequences	D^* (Nm)
LBA	Baseline	24/22	$[90/\text{-}45/0/45]_{3s}$	454
LNC	Nonconventional	24/22	$[90/\text{-}45/75/\text{-}60/60/\text{-}75/\text{-}30/\text{-}15/0/15/30/45]_s$	410
LTP	Thick-ply	24/6	$[90_3/\text{-}45_3/0_3/45_3]_s$	409

Mismatch angle value at each interface for half of the layups													
Interface number after first ply:			1	2	3	4	5	6	7	8	9	10	11	12
Laminate		LBA	45°	45°	45°	45°	45°	45°	45°	45°	45°	45°	45°	*
		LNC	45°	60°	45°	60°	45°	45°	15°	15°	15°	15°	15°	*
		LTP	0°	0°	45°	0°	0°	45°	0°	0°	45°	0°	0°	*

testing laboratory of the University of Girona, which is ISO 17025 and NADCAP (Non-metallic material testing laboratory) certified.

Tab. 4.2: Test matrix of the number of specimens tested; 0J: non-impacted/pristine specimens; AR: as-received or unconditioned specimens; WET: specimens conditioned at 80°C/85% RH. Impactor properties–mass = 5 kg, shape: hemispherical tub with radius R = 8 mm, material: steel of Young,s modulus E = 210 GPa and Poisson ratio $\nu = 0.3$.

Impactor		Laminates and conditions					
Energy (J)	Velocity (m/s)	Baseline (LBA)		Nonconventional (LNC)		Thick-ply (LTP)	
		AR	WET	AR	WET	AR	WET
0	-	4	2	4	2	4	2
12	2.191	3	2	3	2	3	2
20	2.828	3	3	3	3	3	3
30	3.464	2	-	3	-	3	-

4.5 Results

4.5.1 Impact and C-Scan

Impact responses of both AR and WET coupons at the explored impact energy levels are presented in Figs. 4.3 and 4.4. As the impact test reproducibility is reasonably good for both AR and WET coupons in terms of load-time history, only the mean value of load-displacement and impact energy evolution is shown (Fig.4.4) for ease of comparison. For AR coupons, the response of the baseline laminate (LBA) exhibits larger oscillations than those of the thick-ply (LTP) and nonconventional (LNC) laminates after F_d is reached. Once F_d is reached, separation between load-displacement curves emerges, at least for the AR coupons. On average, the F_d of LTP and LNC is 30.5% and 3.5% lower than that of LBA (5.50 kN). Note that the WET coupons of all the laminates have smoother responses than those of the AR coupons, making it hard to detect F_d due to the absence of clear load drop as frequently reported in the literature. Peak load F_{max} and dissipated energy E_{dis} are presented in Figs. 4.5 and 4.6, respectively. As the impact energy increases, the mean values of both F_{max} and E_{dis} increase linearly. For both AR and WET conditions, LBA has the highest F_{max} and the lowest E_{dis} on all impact energy levels, which is consistent with F_d (LBA has the highest F_d). On average, the maximum absolute differences between the AR and WET coupons are 6.4% for F_{max} (of LTP at 20J), and 5.0% for E_{dis} (of LNC at 12J). Like F_{max} and E_{dis}, the indentation depth δ_{ind} and projected delamination area A_{pro} increase with increasing impact energy (see Figs. 4.7 and 4.8). The baseline laminate LBA experiences the lowest δ_{ind} and the smallest A_{pro}. Thick ply significantly affects both δ_{ind} and A_{pro}, particularly for the AR condition. Moisture consistently reduces the indentation depth δ_{ind} of all the laminates, and A_{pro} for LTP and LNC only. Presented in Fig. 4.9 is the C-Scan inspection revealing

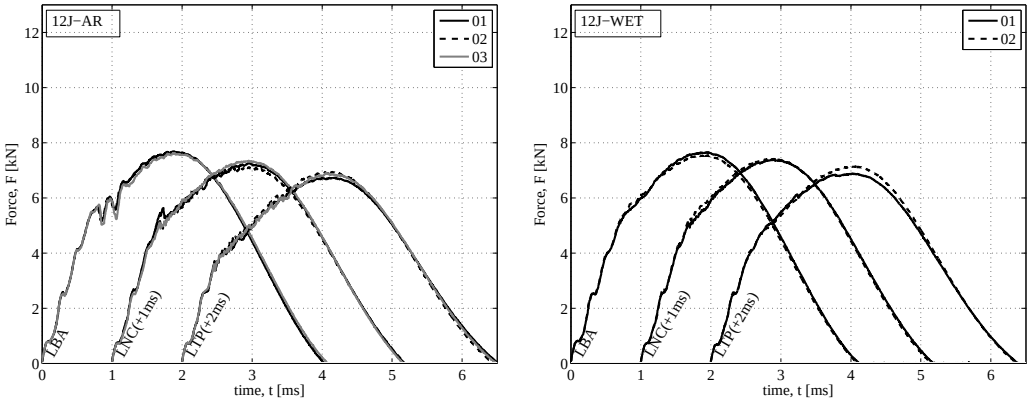

(a) 12 J - AR

(b) 12 J - WET

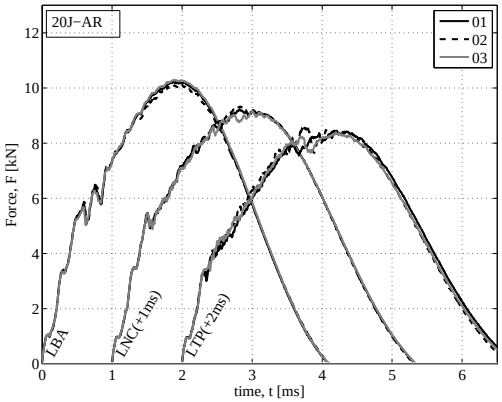

(c) 20 J - AR

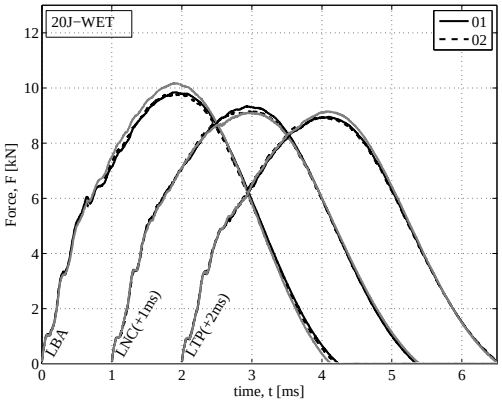

(d) 20 J - WET

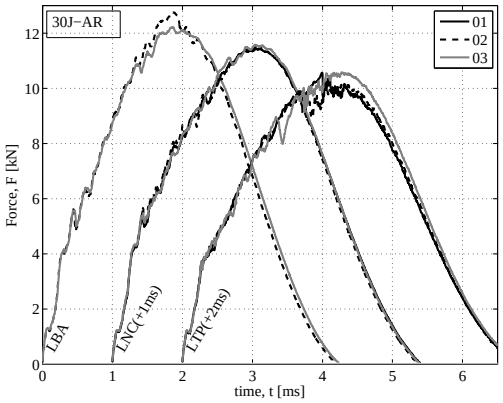

(e) 30 J - AR

Fig. 4.3: Load-time response at different impact energy levels. 01, 02 and 03 refer to the numbering of specimens in each batch tested at given energy level. AR: As-Received specimens, WET: Conditioned specimens (80 °C/85% Relative Humidity), LBA: Baseline, LNC: Nonconventional, and LTP: Thick-ply. Responses of LNC and LTP are offset by 1 and 2 ms respectively for ease of comparison.

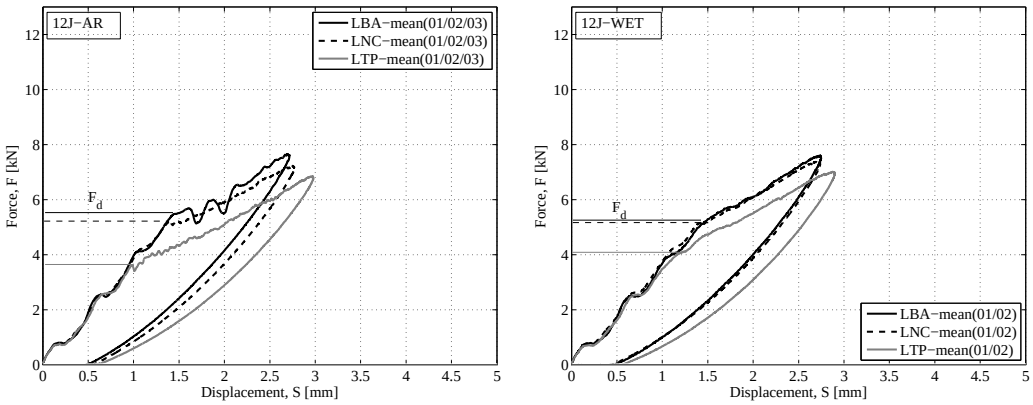

(a) 12 J - AR

(b) 12 J - WET

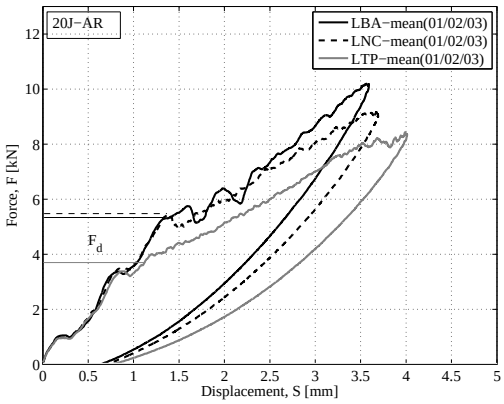

(c) 20 J - AR

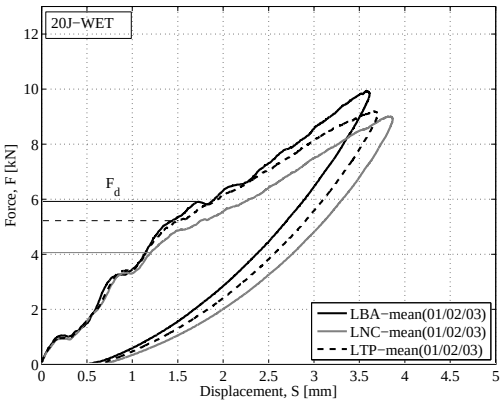

(d) 20 J - WET

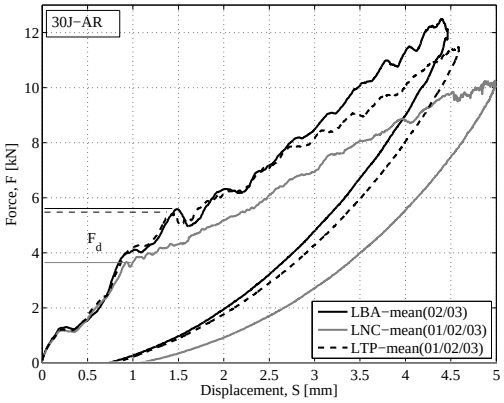

(e) 30 J - AR

Fig. 4.4: Load-displacement mean response at different impact energy levels. AR: As-Received specimens, WET: Conditioned specimens (80 °C/85% Relative Humidity), LBA: Baseline, LNC: Nonconventional, and LTP: Thick-ply.

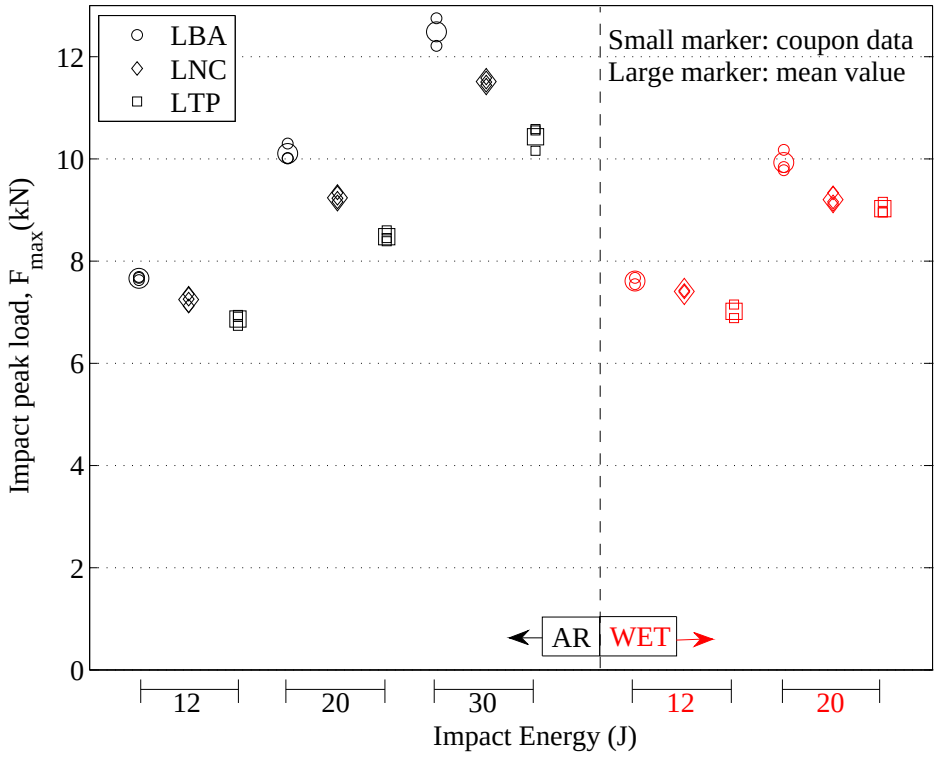

Fig. 4.5: Impact peak load; LBA: Baseline, LNC: Nonconventional, and LTP: Thick-ply. No WET coupons were tested at 30J.

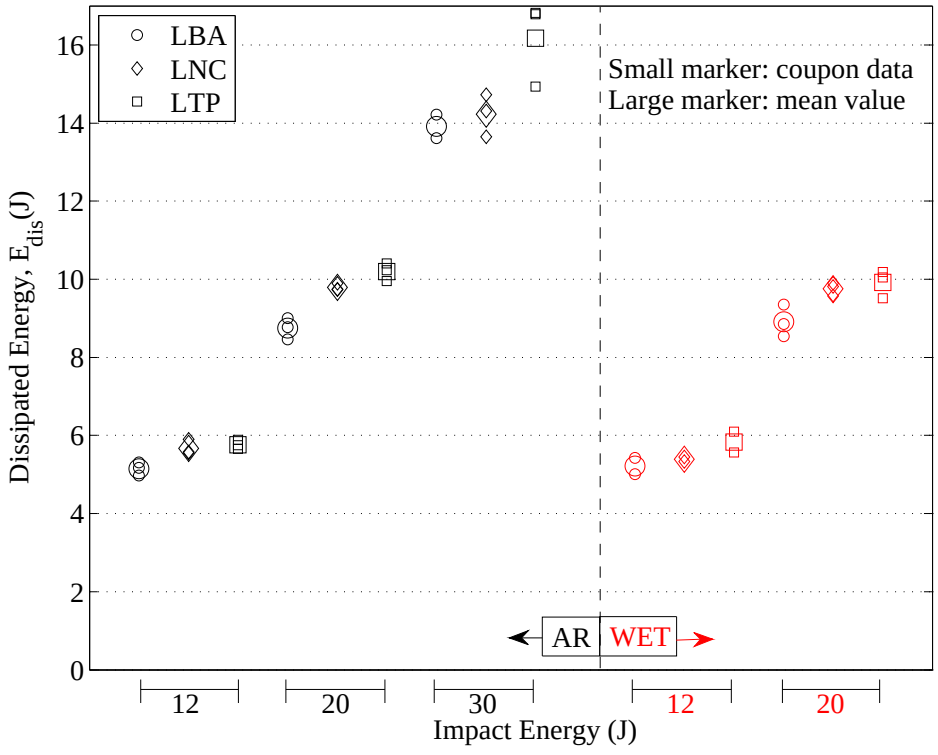

Fig. 4.6: Dissipated energy; LBA: Baseline, LNC: Nonconventional, and LTP: Thick-ply. No WET coupons were tested at 30J.

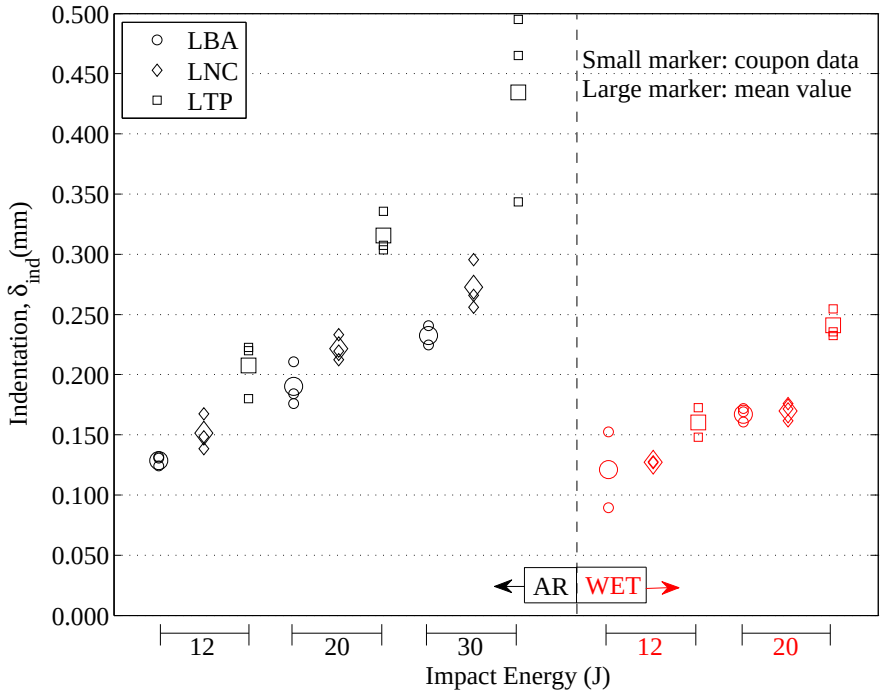

Fig. 4.7: Indentation depth; LBA: Baseline, LNC: Nonconventional, and LTP: Thick-ply. For each individual specimen, indentation depth was taken as mean value of those depths measured by placing the gauge arms along the specimen length and width; no WET coupons were tested at 30J.

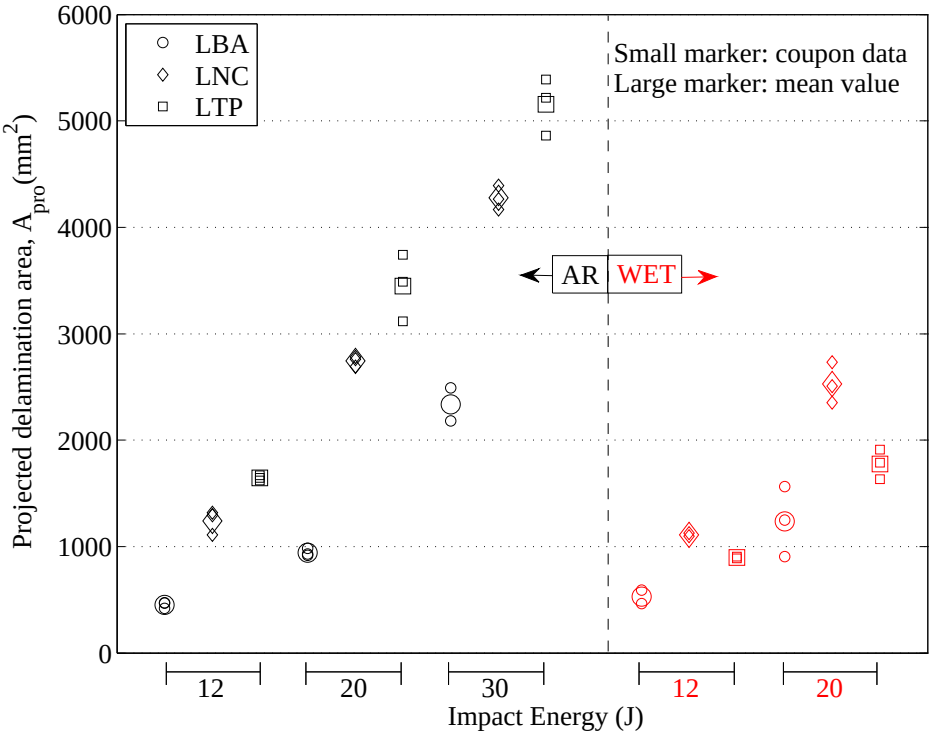

Fig. 4.8: Projected delamination area; LBA: Baseline, LNC: Nonconventional, and LTP: Thick-ply. For each individual specimen, projected delamination was taken as mean value of those projected delamination areas observed through C-Scan from impacted and non-impacted faces; no WET coupons were tested at 30J.

the shapes and sizes of the delaminated interfaces located through the thickness of the three laminates. Delaminations in LBA are more localized and circular than those seen in LTP and LNC. For the LTP AR specimens, delaminations are larger and more distinguishable, due to few non-zero MMA interfaces, than those of LBA and LNC. With the aid of the colour bar showing through-the-thickness locations of delaminated interfaces, the delamination sizes within the bottom sublaminate of LNC are seen to be larger than those within the central sublaminate. For the AR coupons of LTP and LNC tested at high energy, the extension of their delaminations reaches the window cut-out width (75 mm) of the impact fixture support. That is, the delamination area is highly constrained by the boundaries of the fixture.

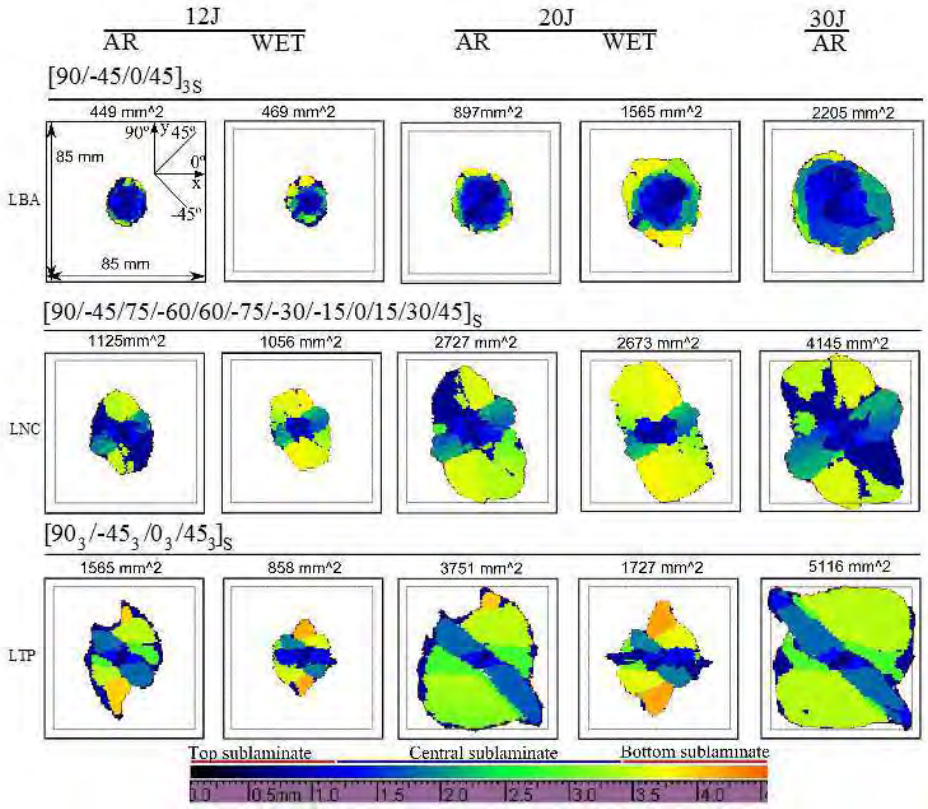

Fig. 4.9: C-Scan inspection of delaminated interfaces; LBA: Baseline, LNC: Nonconventional, and LTP: Thick-ply. Colour bar indicates the depth of coupon as measured from the non-impacted face. No WET coupons were tested at 30J; 75 mm is the shortest in-plane dimension of the window cut (125x75 mm) on impact fixture as specified in ASTM D7136M-12 [164].

4.5.2 Compression after impact

Owing to a lack of impact energy levels, asymptotic behaviour of no damage (at lower impact energy levels) and perforation (at higher energy levels) does not appear on the plots in Fig. 4.10. Superior strength are seen in LBA for AR specimens impacted at 12J and 20J, Fig. 4.10. For AR coupons, the compressive strength of non-impacted

LTP and LNC is 10-19% lower than that of LBA. The plot of normalized mean CAI strength in Fig. 4.10b reveals that the compressive strength retention of LTP and LNC at high impact energy (30J) is higher than that of LBA. This normalization of each laminate type is the ratio of the mean compressive strength of that laminate at a given impact energy level to the mean compressive strength of non-impacted specimens.

Moisture reduces the compressive strength of pristine specimens in all the laminates. The strength of pristine WET coupons decreases compared to their AR counterparts by 7%, 14%, and 12% on average for LBA, LTP, and LNC, respectively. For the impacted coupons at 12 J and 20 J there is a tendency to higher σ_{CAI} for WET samples (except LTP at 12 J and LBA at 20 J). For WET impacted coupons, only for LNC does CAI strength increase monotonically in the presence of moisture with respect to AR conditions (17% at 12 J and 16% at 20 J, see Fig. 4.10a). Note that the LNC WET coupons have even higher σ_{CAI} than those of LBA WET coupons at 20 J.

4.6 Discussion

The first area to be discussed is whether the selection of the MMA's across the thickness of the LNC laminate (large MMA within the bottom sublaminate and small MMA within the central sublaminate, Fig. 4.1) allows the location of delaminations to be predetermined. C-scan analysis of the LNC laminate (Fig. 4.9) provides evidence of large delaminations within the bottom sublaminate and small delaminations within the central sublaminate, thus supporting the initial hypothesis of this work. The differences on the distribution of delamination sizes between LNC and LBA (the baseline) are clear. However, the approach did not result in completely preventing delaminations in the central sublaminate, as was the aim. The fact that the extension of delaminations at the bottom sublaminate was constrained by the boundaries should be taken into account. Considering that in impact events that do not produce fibre failure, delaminations are the main energy dissipating mechanism, the prospect is that an impact on a specimen and boundary condition larger than the ones studied here, would have produced larger delaminations at the bottom sublaminate, at least for the impact energy levels equal to or greater than 20 J. Larger delaminations mean more dissipated energy, so the extension of delaminations within the central sublaminate would be expected to decrease. That is, the success of the proposed approach (Fig. 4.1) avoiding delaminations in the central sublaminate is hindered by the effect of the boundaries.

Before addressing whether the compressive strength after impact improves in LNC, it should be made clear that comparing the compressive strength of LBA, LNC and LTP needs to be done with a certain amount of caution. Indeed, the failure under on-axis

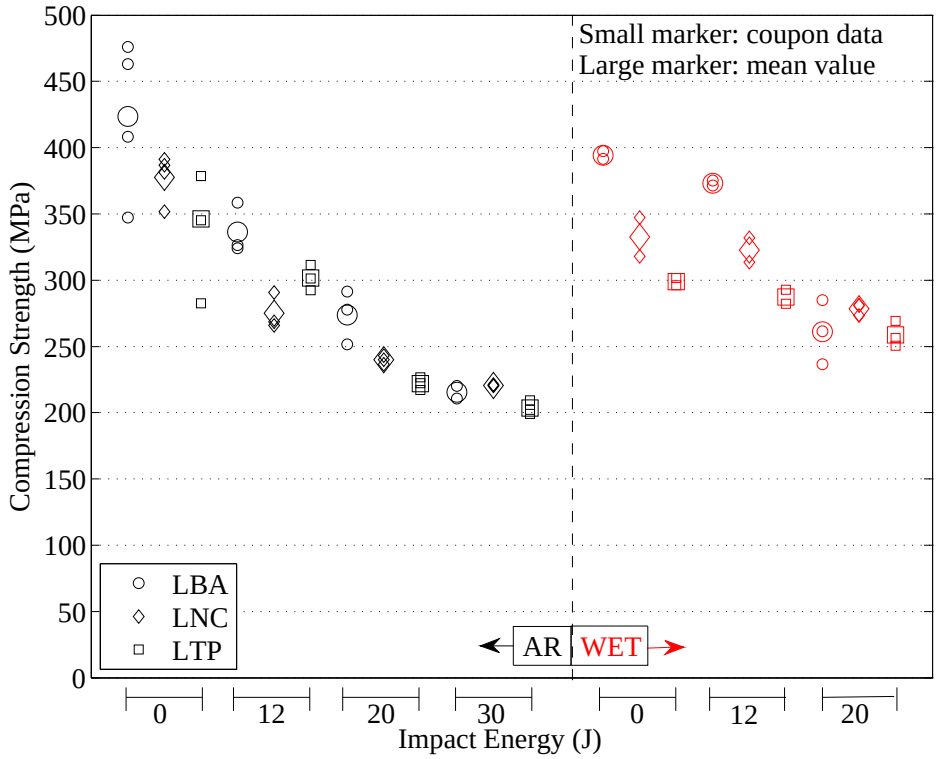

(a)

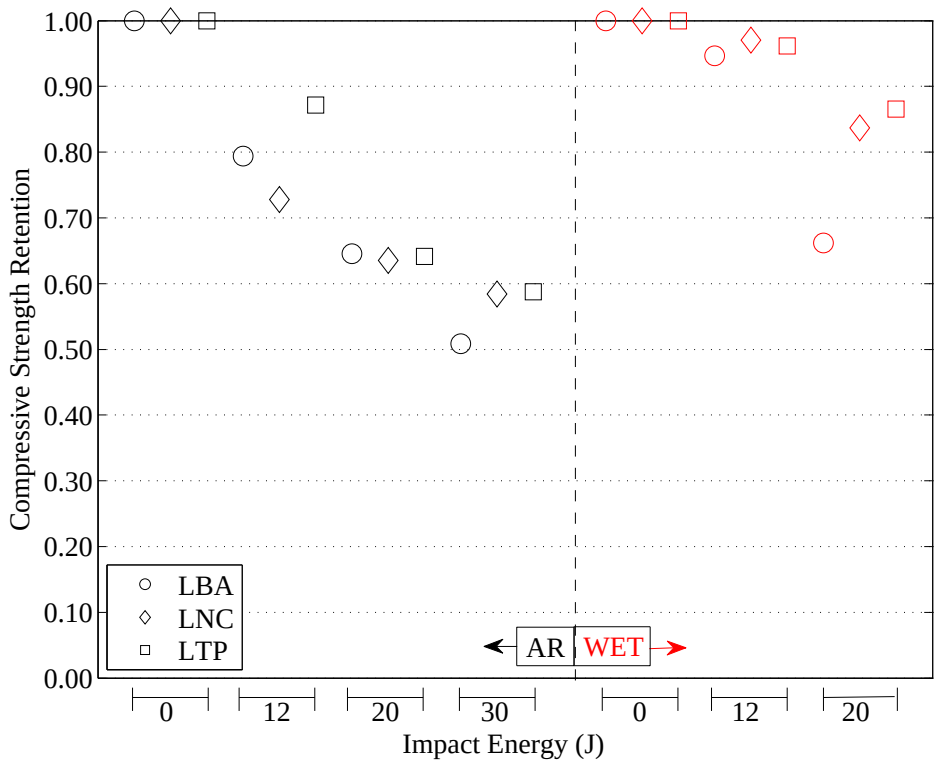

(b)

Fig. 4.10: Compression and CAI strength (a), and mean compression retention strength (b); LBA: Baseline, LNC: Nonconventional, and LTP: Thick-ply. 0J: non-impacted/pristine coupons; no WET coupons were tested at 30J.

compression is a fibre-dominated mechanism which is very sensitive to the alignment of the reinforcement with the applied load [174, 175]. LNC possesses three times fewer the number of 0° plies found in the baseline LBA. This can explain why LNC provided lower CAI strength than LBA did, albeit with the exception of specimens impacted at high energies (AR coupons impacted at 30J and WET coupons at 20J of Fig. 4.10). At these high impact energies the LNC retained their strength more efficiently than LBA and LTP. In terms of practical applications in aircraft structures, this behaviour is an asset.

The effect of blocking three plies (LTP laminate) is detrimental to both impact damage resistance and tolerance. In comparison to LBA, LTP results in lower F_d, lower F_{max}, higher E_{dis}, deeper δ_{ind}, larger A_{pro}, and low compressive strength for both non-impacted and impacted specimens. The low damage resistance and tolerance of LTP can be attributed to the in-situ strength effect for matrix cracking (i.e. the strength decreases as the thickness of the ply increases) [176–180]. Therefore, matrix cracking, and the associated delaminations, occurs earlier in blocked plies than in dispersed plies [5]. The effects of ply thickness on damage resistance to LVIs have also been reported in other studies [17, 19–21, 181]. Although the study conducted in this paper, and those in [21, 181], consider different composite systems and layups, the same effect of the blocking plies on CAI strength is observed.

The impact behaviour of the three laminates is altered in the presence of moisture. Firstly, after F_d is reached, load-time or load-displacement of the WET coupons exhibits smaller oscillations than those of the AR coupons; especially for LBA (Figs. 4.4). The physical reason behind this behaviour is unclear to the authors. Since delamination in the AR specimens tends to propagate unstably, this trend could be related to a tougher matrix (thus, interfaces) in WET specimens, as reported in [182]. The extension of delamination in Fig. 4.9 supports this idea for LTP and LNC in particular.

No sudden load drop due to specimen stiffness loss can be seen on either the load-time or load-displacement curves of the WET coupons (Figs. 4.3–4.4). Instead, the load-displacement curves show a gradual loss of stiffness about where the load is identified as F_d in the figures mentioned above.

A tougher matrix could also explain the noticeable increase of the F_d of LTP, compared to AR conditions as the onset of matrix cracking is delayed [127]. Reduced residual stresses associated to the plasticization of the matrix induced by moisture could also contribute to delaying the onset of damage mechanisms.

Moisture reduces the indentation depth δ_{ind} (Fig. 4.7). This same observation was reported elsewhere [128] but no explanation was given. Besides, moisture tends to reduce A_{pro} of all the laminates, except the baseline LBA (Fig. 4.8). Reduced

A_{pro} in the presence of moisture was also reported in [126, 127]. Scanning electron microscopy (SEM) images in [127] reveal that the number of matrix transverse cracks and delamination sizes are smaller in the WET specimens than in the AR specimens. Again, this behaviour is coherent with a tougher matrix.

Lastly, while moisture does reduce the undamaged compressive strength, the effect on the compressive strength of impacted specimens depends on the laminate itself. CAI in LTP and LNC decreases for 12J but increases for 20 J, where in LBA case, strength increases at 12 J and but not at 20 J. Again, the retention for strength of LNC outperforms dramatically that of LBA.

An ongoing detailed microstructural investigation of damage evolution in quasistatic tests will contribute to clarifying the effect of moisture on the impact behaviour of these laminates.

5 Damage development under quasi-static indentation

5.1 Overview

Chapter 4 demonstrated the success of predetermining the through-the-thickness positions of delamination in LNC and the overall characteristics of the impact damage in each laminate. However, LVI tests do not enable the sequence of damage development to be elucidated, especially around the delamination threshold load. It was also difficult to determine the threshold load for some cases because of the unobvious load drop. Therefore, the main aim of this chapter is to experimentally investigate the damage occurrence focusing on the damage initiation and delamination propagation in the three laminates studied in Chapter 4. To this purpose, the quasi-static indentation (QSI) was used under displacement instead of LVI. Also discussed here are the moisture effects on the behaviour of the laminates as well as the similarities and differences in the global responses and overall damage extent resulted from both QSI and LVI tests. The content of this chapter achieves the second objective stated in Section 1.3, and partially fulfills the fourth and fifth objectives of the same section in terms of the out-of-plane loading. The test methods used for QSI, overall damage extent and detailed damage morphology were presented in Sections 3.2.2, 3.3.2 and 3.3.3 respectively.

5.2 Material, layups and test matrix

In this test campaign, the composite material system and layup definition as well as their associated details are the same as those described in the study presented in Chapter 4, see Table 4.1 for stacking sequences. The test matrix for the quasi-static indentation test is summarized in Table 5.1. Due to lack of available material, only two indentation tests on WET coupons were performed. The superscripts a and b refer to specimens subjected to Tomography inspection with Group A and Group B imaging conditions listed in Table 3.2 of Section, respectively. Only AR specimens were inspected with μCT due to the availability of the inspection facilities.

5.3 Results

Tab. 5.1: Test matrix; AR: as-received or unconditioned specimens; WET: specimens conditioned at 80°C/85% RH until moisture equilibrium. Indenter shape: hemispherical tub with radius R = 8 mm, material: steel of Young's modulus E = 210 GPa and Poisson ratio $\nu = 0.3$.

Applied indentation displacement in mm	Number of coupon per laminate and condition					
	LBA		LTP		LNC	
	AR	WET	AR	WET	AR	WET
1.1	1^a	-	1^a	-	1^a	-
1.5	1^b	1	1^b	1	1^a	1
3.5	1^b	1	1^b	1	1^b	1

5.3.1 Quasi-static indentation (QSI)

The load-deflection curves at different applied indentation displacements are presented in Figs. 5.1-5.3. The test results clearly show that the curves are excellently reproducible as the curves of the coupons under higher applied displacements closely follow the ones under lower displacements, see Fig. 5.1. Fig. 5.2 compares the out-of-plane load-carrying capability of each laminate under equivalent applied displacement. The responses of all the three layups are the same until around 2.5 kN, where LTP can be observed to be more compliant than the other two layups. The influence of moisture on the global response of the three laminates can be easily seen on Fig. 5.3.

Fig. 5.4 summarizes the dissipated energy E_{dis} due to the damage development at different applied indentation displacements. E_{dis} was determined from the areas bounded between loading and unloading parts of the load-deflection curves using trapezoidal numerical integration. At low indentation displacements of 1.1 or 1.5 mm, LTP dissipated higher amount of energy than any other layups. However, the LNC turned out to dissipate the highest energy at 3.5 mm. This altered behaviour is observed for both specimen conditions (AR and WET). It is worth remarking that such alteration was not observed in the case of impact loading studied in the preceding chapter, see Fig. 4.6.

The permanent indentation depths measured right after the indentation tests are given in Fig. 5.5 respectively. Unlike the dissipated energy, LTP exhibited the deepest indentation regardless of all the applied displacements and specimen conditions. This observation is consistent with the impact loading case study, see Fig. 4.7.

5.3.2 C-Scan inspection

For quick comparison, the projected damage areas A_{pro} are plotted in Fig. 5.6. The overall morphology of delaminations is presented in Fig. 5.7. Each damage morphology is accompanied with A_{pro} value placed on top of the C-Scan image of

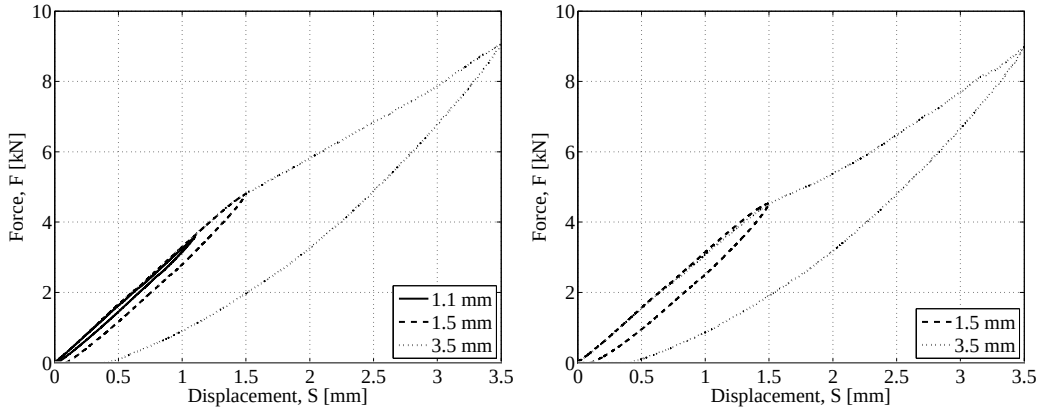

(a) LBA AR specimens **(b)** LBA WET specimens

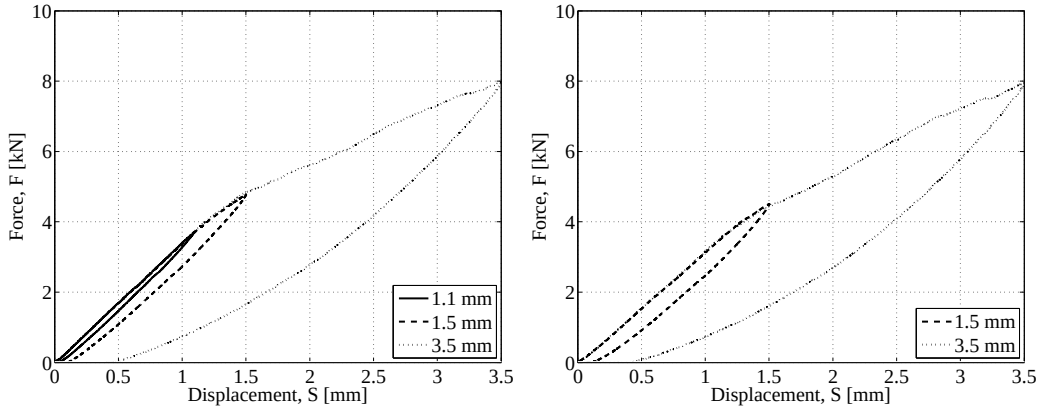

(c) LNC AR specimens **(d)** LNC WET specimens

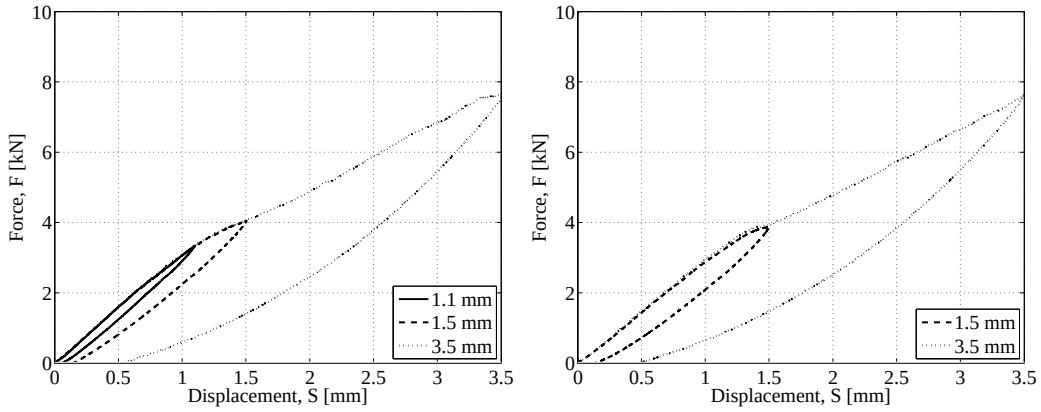

(e) LTP AR specimens **(f)** LTP WET specimens

Fig. 5.1: Load-displacement curves of LBA, LNC, and LTP for two specimen conditions, AR and WET, at different indentation displacements.

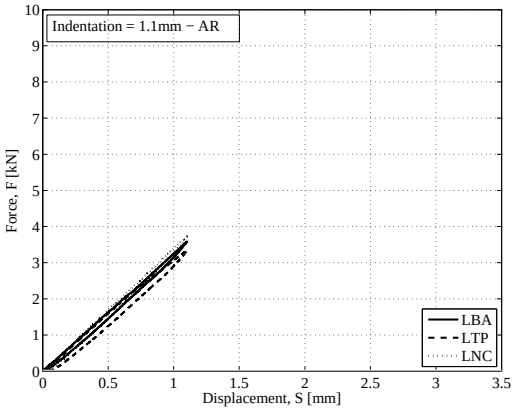

(a) AR specimen at 1.1 mm

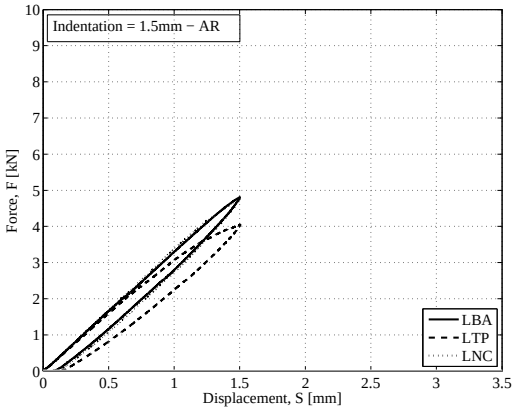

(b) AR specimen at 1.5 mm

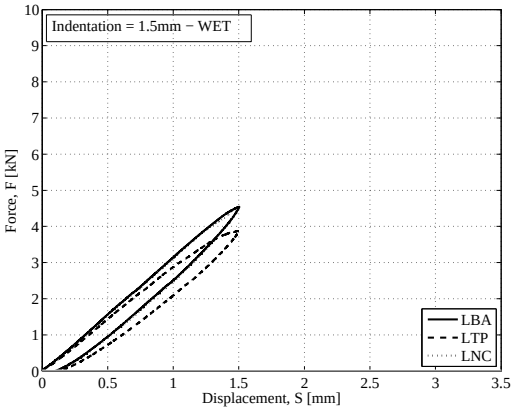

(c) WET specimen at 1.5 mm

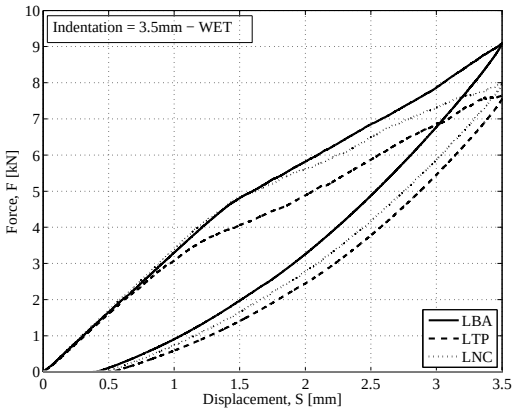

(d) AR specimen at 3.5 mm

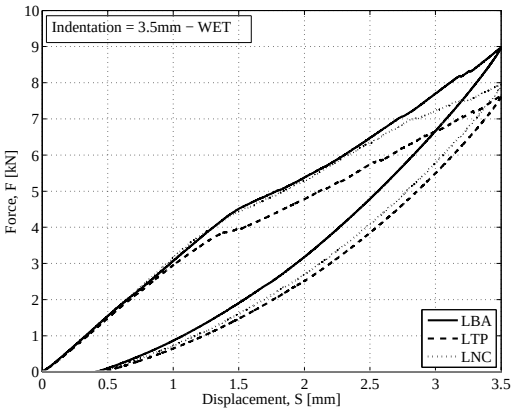

(e) WET specimen at 3.5 mm

Fig. 5.2: Comparison of load-deflection curves at equal applied indentation displacements for AR and WET coupons.

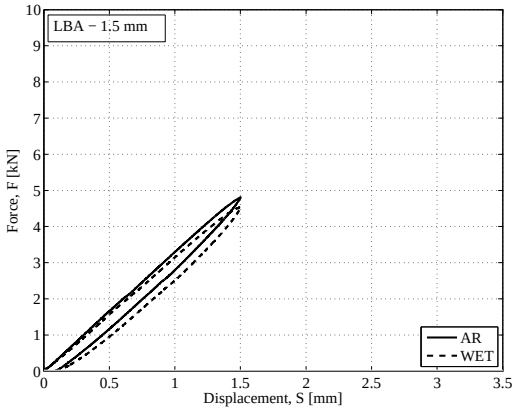

(a) LBA: AR and WET at 1.5 mm

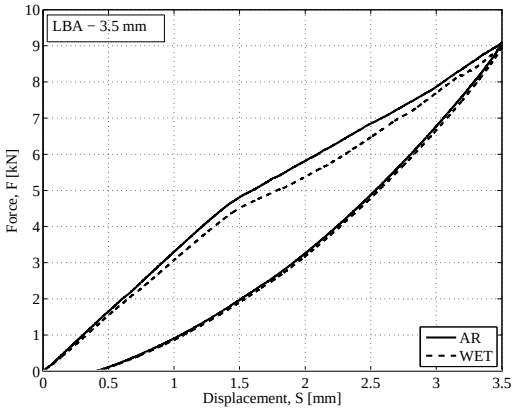

(b) LBA: AR and WET at 3.5 mm

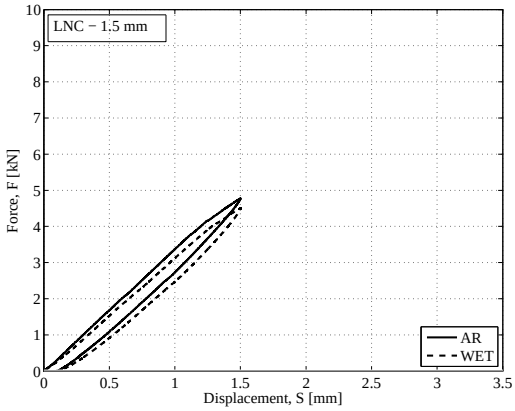

(c) LNC: AR and WET at 1.5 mm

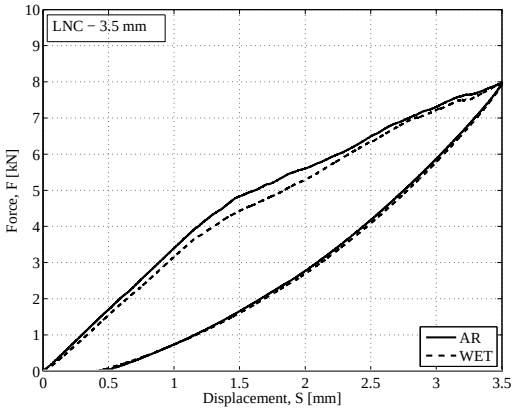

(d) LNC: AR and WET at 3.5 mm

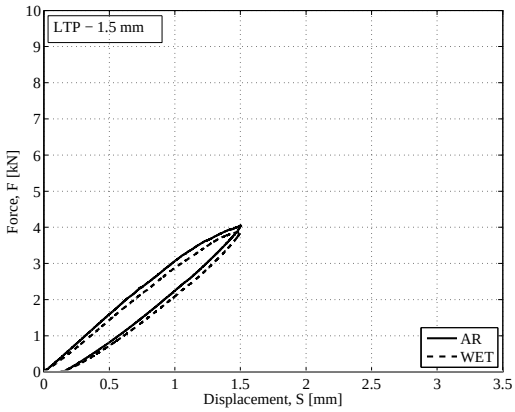

(e) LTP: AR and WET at 1.5 mm

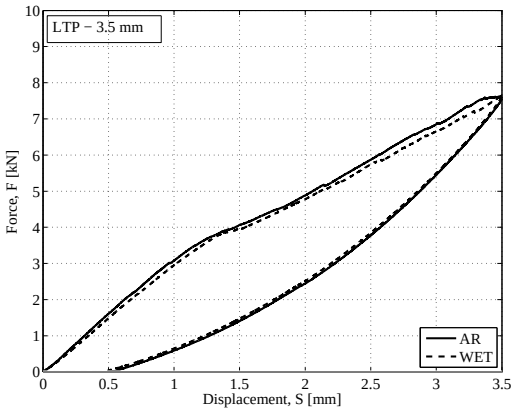

(f) LTP: AR and WET at 3.5 mm

Fig. 5.3: Comparison of load-deflection curves of AR and WET specimens at equal applied indentation displacements.

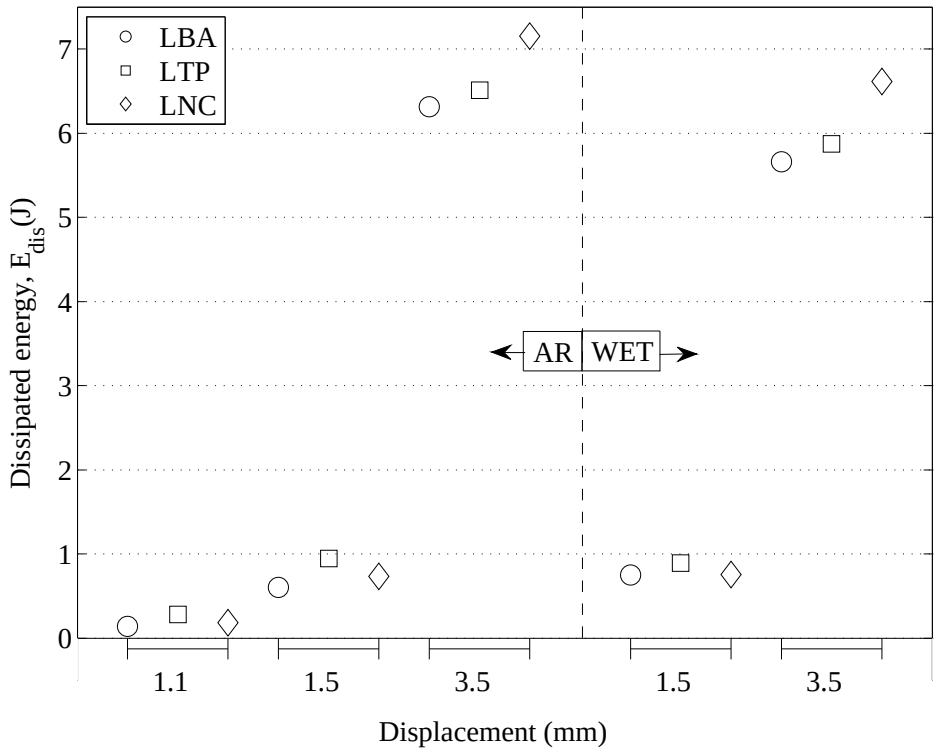

Fig. 5.4: Dissipated energy of laminates at applied displacements.

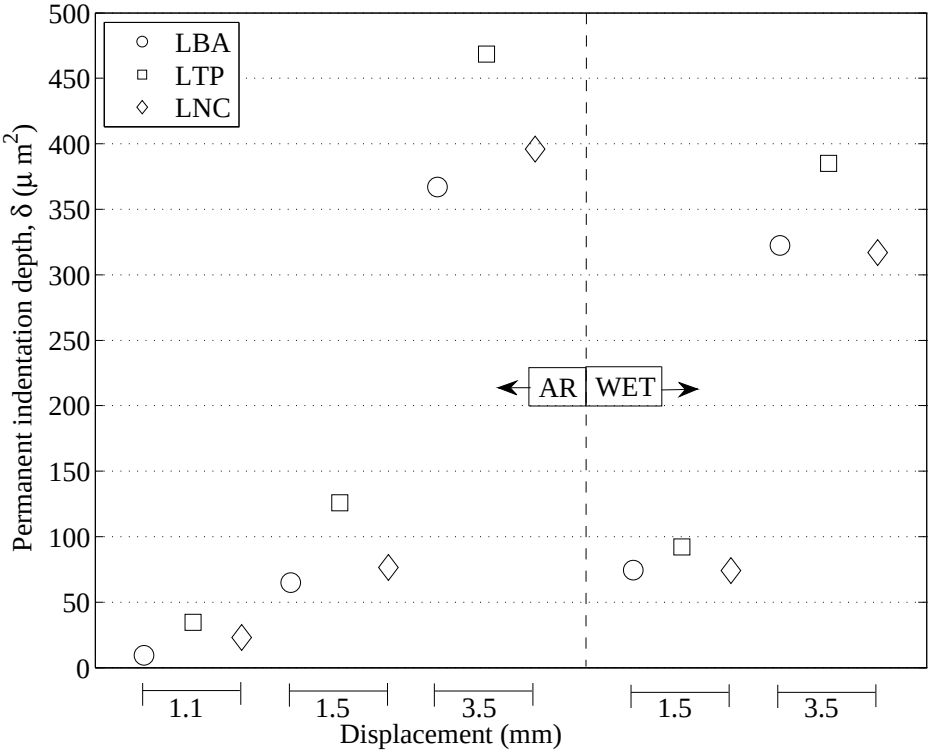

Fig. 5.5: Permanent indentation, measured right after indentation tests, at different applied displacements.

each inspected coupon. The through-the-thickness position of delaminations can be seen on the attached colour bar (ply thickness 0.184 mm). For layups tested at 1.1 mm, C-Scan revealed damage in the LTP only. At 1.5 mm, LTP experienced larger A_{pro} than the other two layups. Surprisingly, LTP showed smaller A_{pro} than LNC at 3.5 mm of applied displacement. This behaviour trend is observed for both specimen conditions, and is consistent with E_{dis} summarized earlier. Such alteration did not occur in the case of impact loading presented in the preceding chapter. Unlike the impact loading case, the presence of moisture tends to reduce A_{pro} for all layups except for LBA at 1.5 mm.

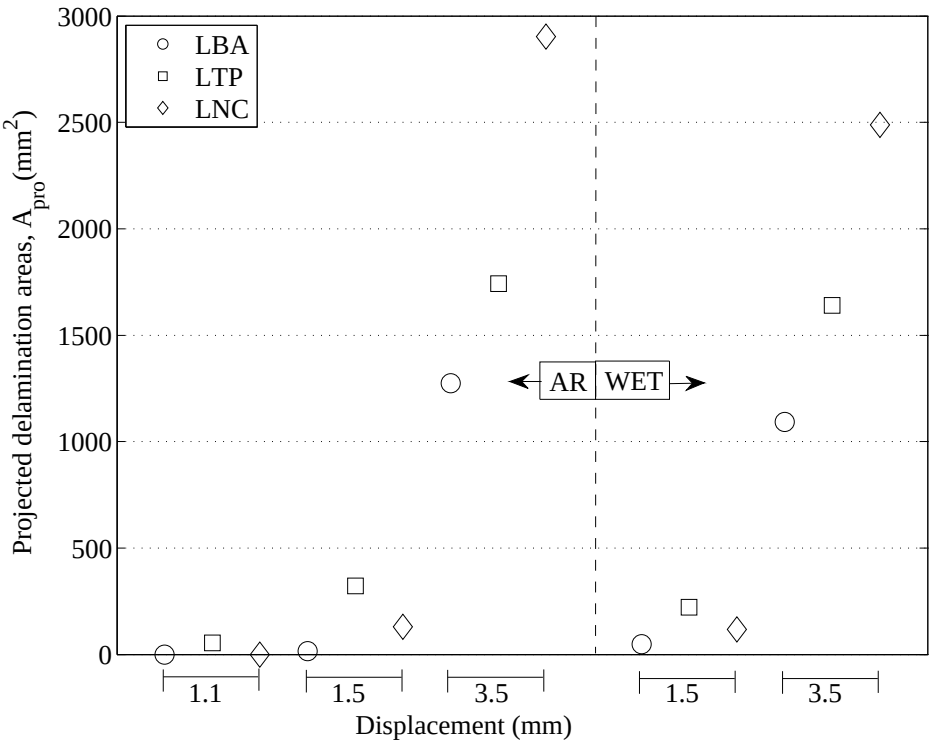

Fig. 5.6: Projected delamination at different applied displacements.

5.3.3 Computed Tomography inspection

Figs. 5.8 displays the segmented transverse matrix cracks and delaminations projected on the laminate plane for LBA (a) and LNC (b) at displacement of 1.5 mm. The details regarding location of the cracked plies and delaminated interfaces are given in Fig. 5.9 for LBA and Fig. 5.10 for LNC. Intraply matrix cracks are coloured black, whereas other colours represent delaminations. When the dark lines are thick, the matrix cracks belong to those plies oriented in the directions different from 0 and 90°. It is interesting to note that the directions and extents of the plies adjacent to the interface control the delamination morphology of an interface. The CT images of the through-the-thickness damage distributions caused by the indentation displacement of 3.5 mm are shown in Fig. 5.11. The cross-sectional views are from the cut along

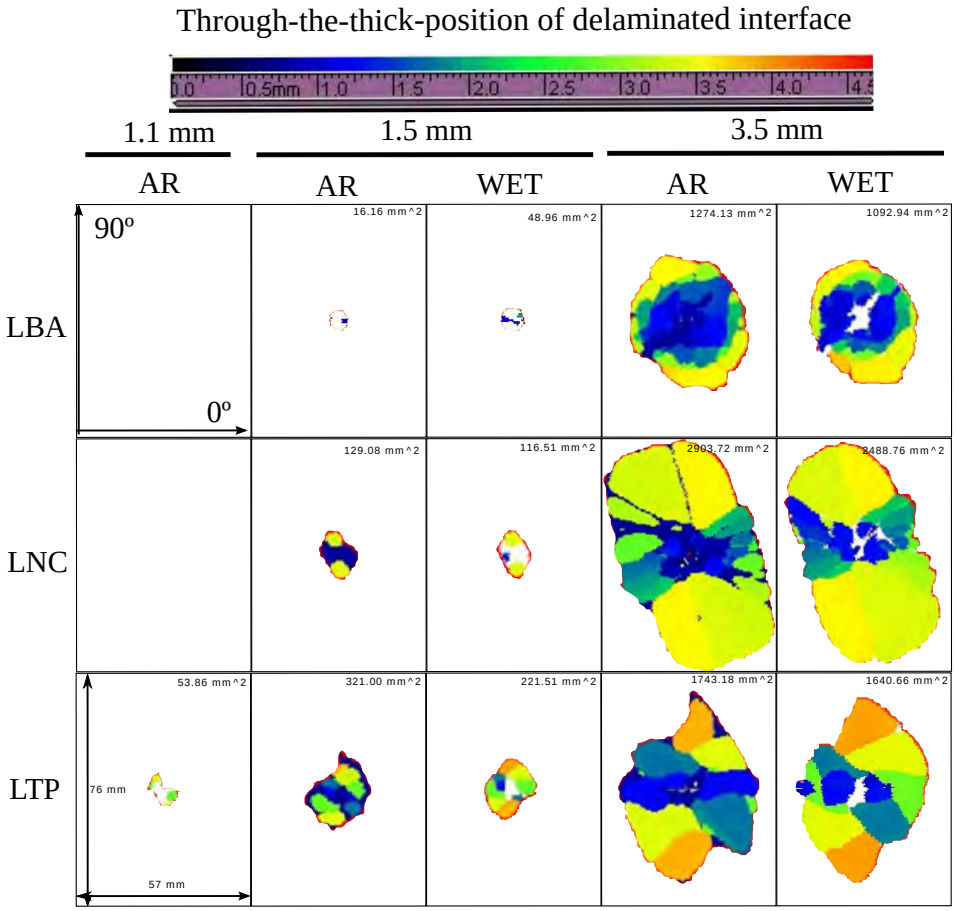

Fig. 5.7: C-Scan delamination shape and projected delamination areas in the inspection taken from the impacted face.

the 90°-ply. Again, the regions lacking damage can be observed underneath the impacted locations of the three layups.

To have a general overview of the through-the-thickness distribution of the two damage modes, cross-sectional views along the 90° obtained from CT inspection are shown in Fig. 5.11 for the applied indentation displacement of 3.5 mm. Note that, even at this large displacement, the two damage modes are still absent right underneath the impact zone in all layups. This evidence complements the inplane ply-by-ply observation of the LNC just presented.

5.3.4 Mapping damage on load-deflection curve

Figs. 5.12, 5.13 and 5.14 map the damage development onto the representative load-deflection curve with images from CT and/or C-Scan for LBA, LNC and LTP respectively. The figures were also illustrated to display the stiffness loss percentage after the knee-point. The knee-point corresponds to the load level around which the laminate stiffness starts to degrade gradually, so a clear difference is observed between the preceding and following parts of the curve. For all the laminates, this load level was assumed to be at the intersection between two linear regression lines, before knee-point and after knee-point. The former in gray dash line was obtained from data points between 0.1 and 0.6 mm, and the latter in black dotted line between 1.75 and 2.5 mm. This critical load is often seen as the onset of delamination propagation, generally known as the delamination threshold load (F_d) in impact loading. Note that the knee-point identified in this manner appears before any form of damage can be detected by C-Scan inspections for all laminates. CT images at 3.5 mm displacement in Fig. 5.11 reveal the different damage damage as seen a cut along the 90° ply.

5.3.5 Comparison between QSI & LVI

Load-deflection responses

The global response of all the laminates in (AR and WET conditions) are plotted in Fig. 5.15 in terms of load-deflection curves for the case of indentation displacement of 3.5 mm and low velocity impact of 20 J. The gradients of the unloading part of both indentation and impact responses are almost the same with the exception of LTP AR case. This particularity is a parallel to the case of projected delamination areas A_{pro} against the applied energy E_{app}. Furthermore, the loading part of the QSI test follows closely to that of the LVI test. This behaviour is not present in the rest of the cases. The results also reveal that, unlike most composite systems reported in the literature, there is no observable load drop in the global behaviour response. Instead, there exists a change in the slope at a critical point, namely a knee-point.

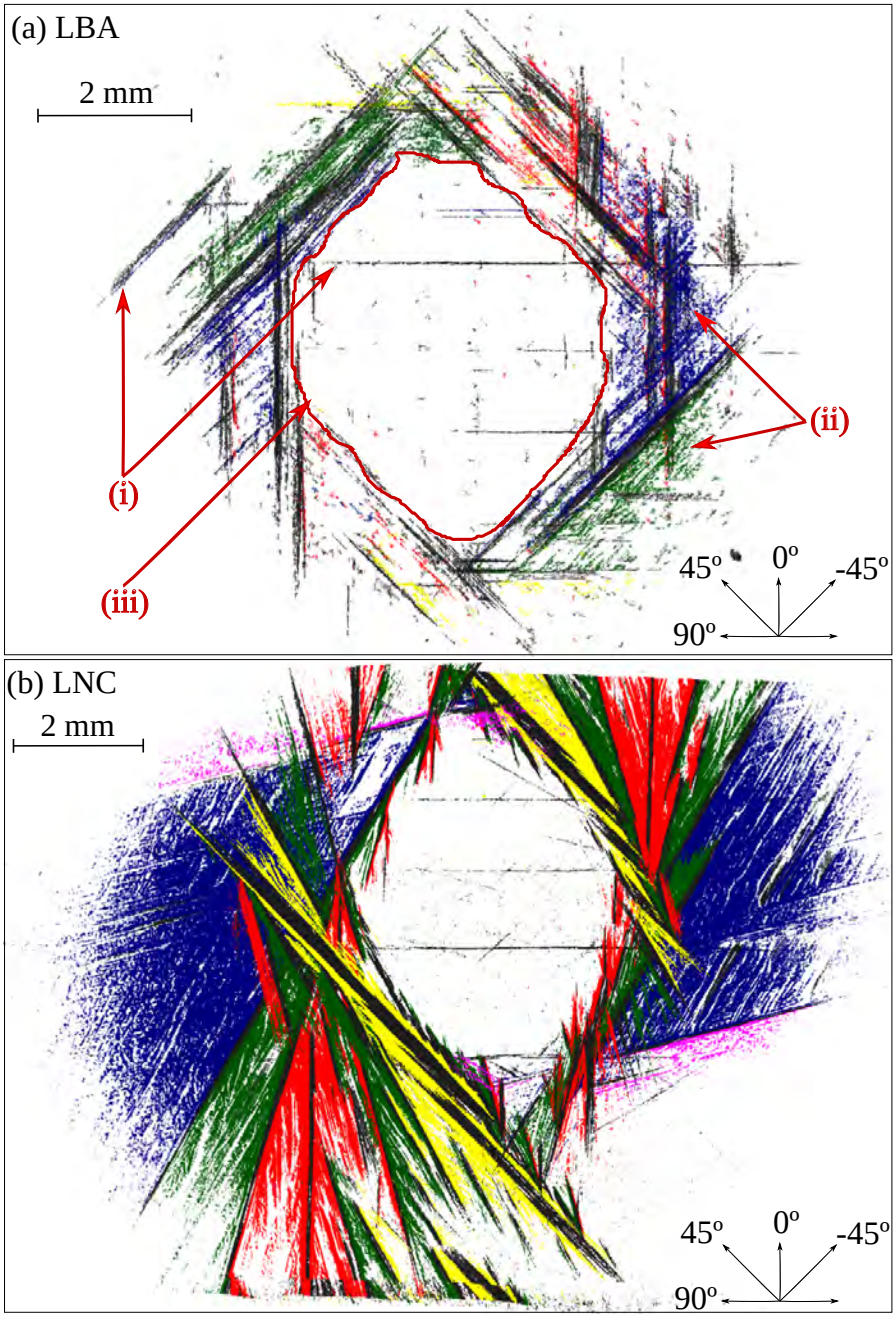

Fig. 5.8: Transverse matrix cracks and delaminations for LBA (a) and LNC (b) caused by indentation displacement of 1.5 mm. (i): examples of matrix transverse cracks, (ii): examples of delaminations and (iii): area lacking matrix cracks and delaminations.

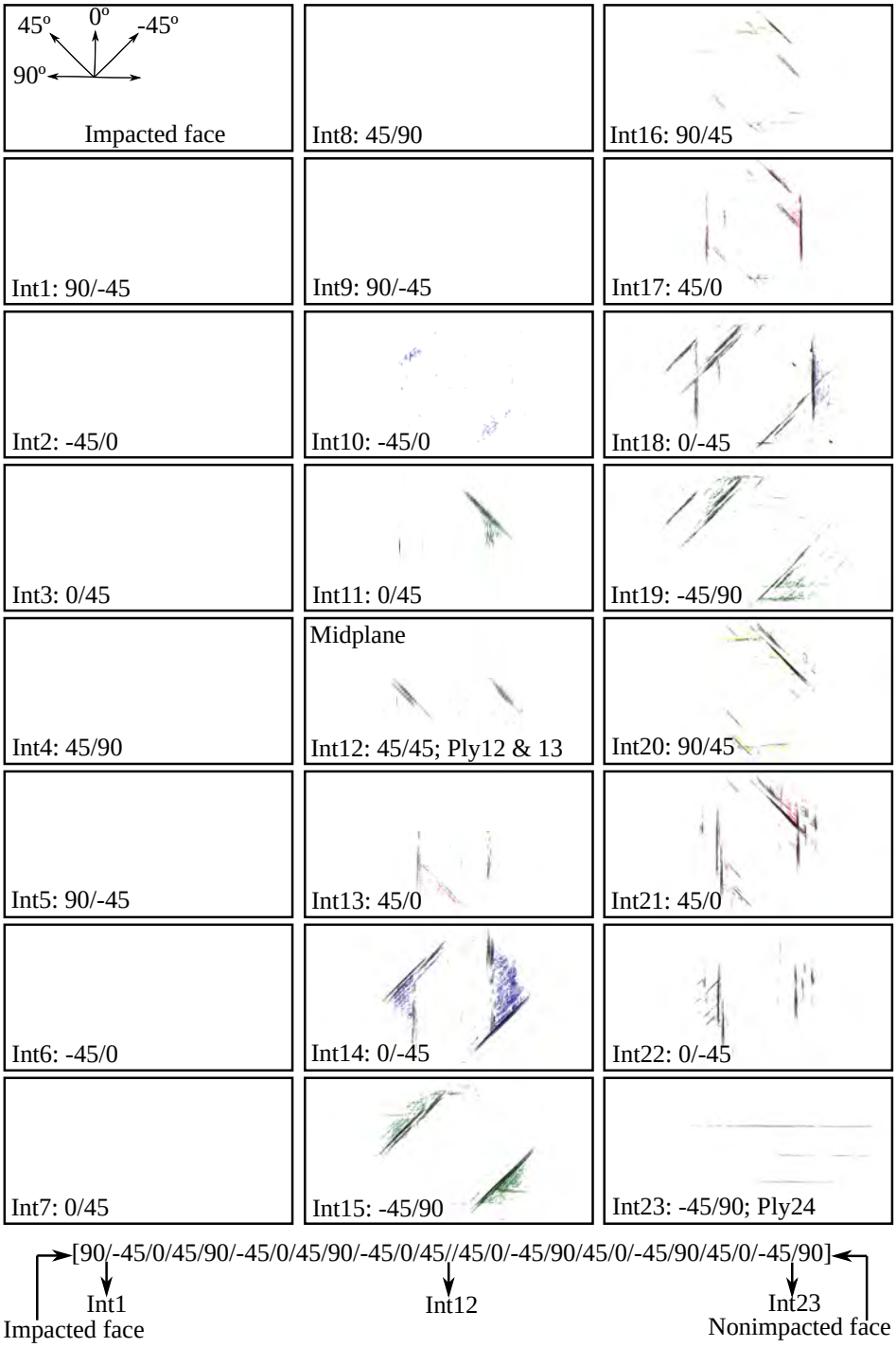

Fig. 5.9: CT images of LBA showing delaminations and transverse matrix cracks caused by indentation displacement of 1.5 mm.

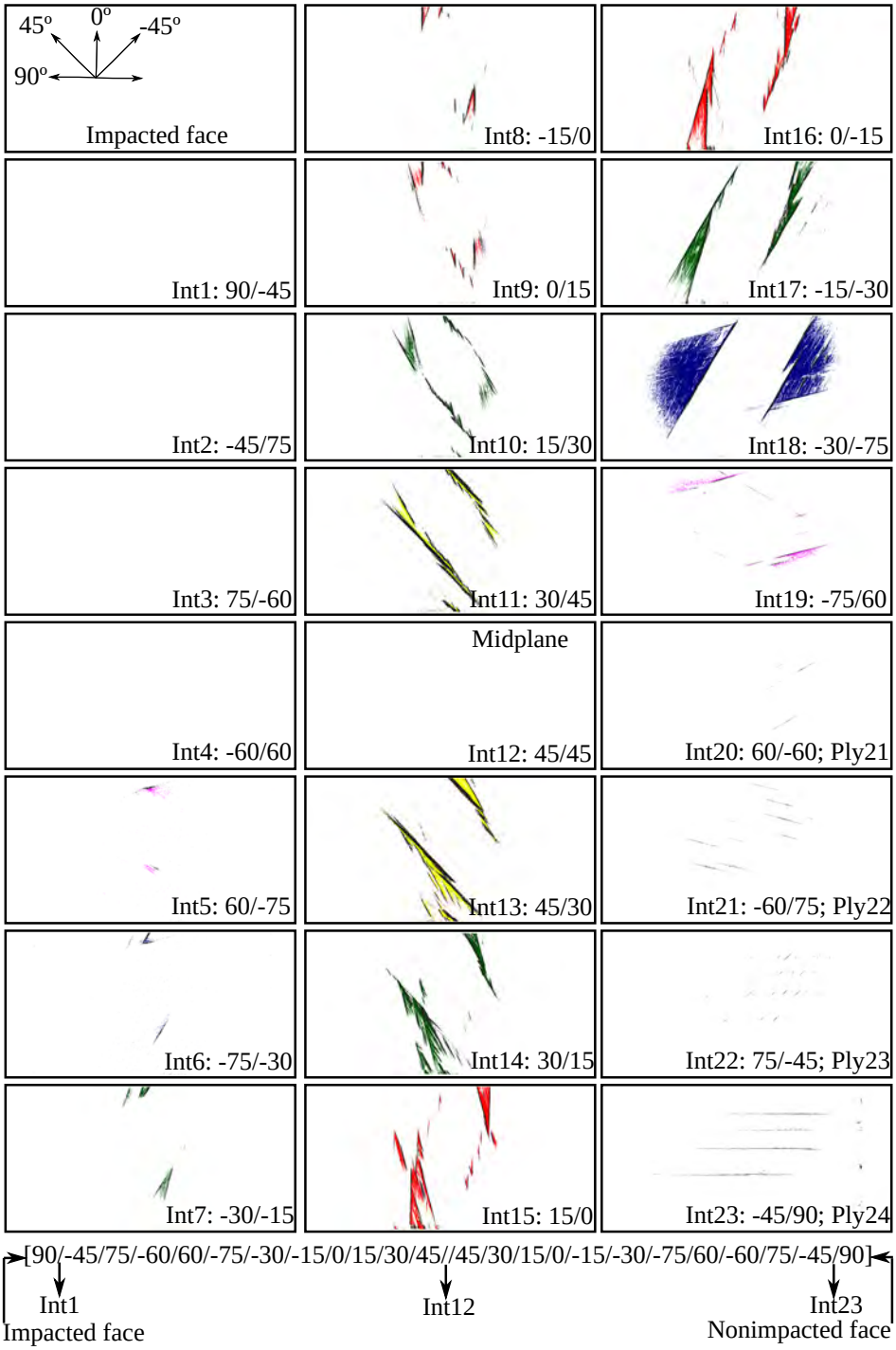

Fig. 5.10: CT images of LBA showing delaminations and transverse matrix cracks caused by indentation displacement of 1.5 mm.

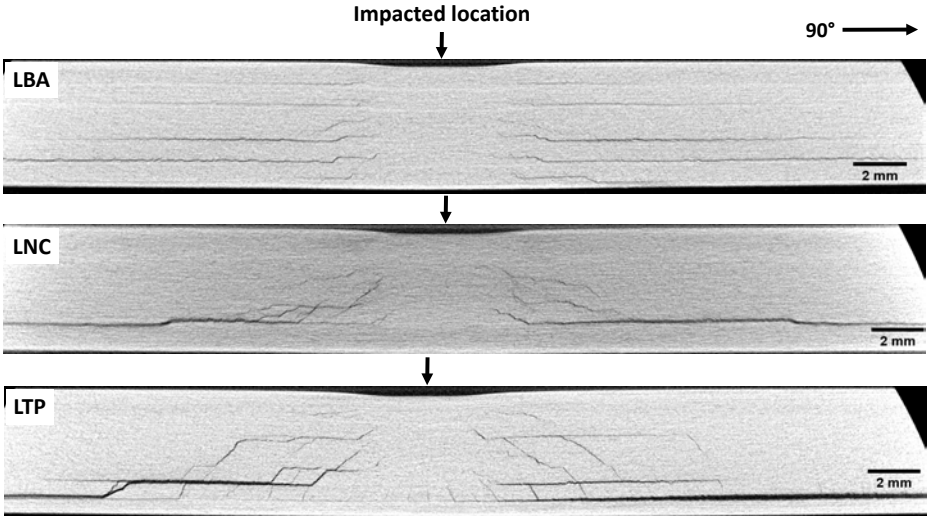

Fig. 5.11: CT images of cross-sectional cut along 90° for all laminates under applied indentation displacement of 3.5 mm.

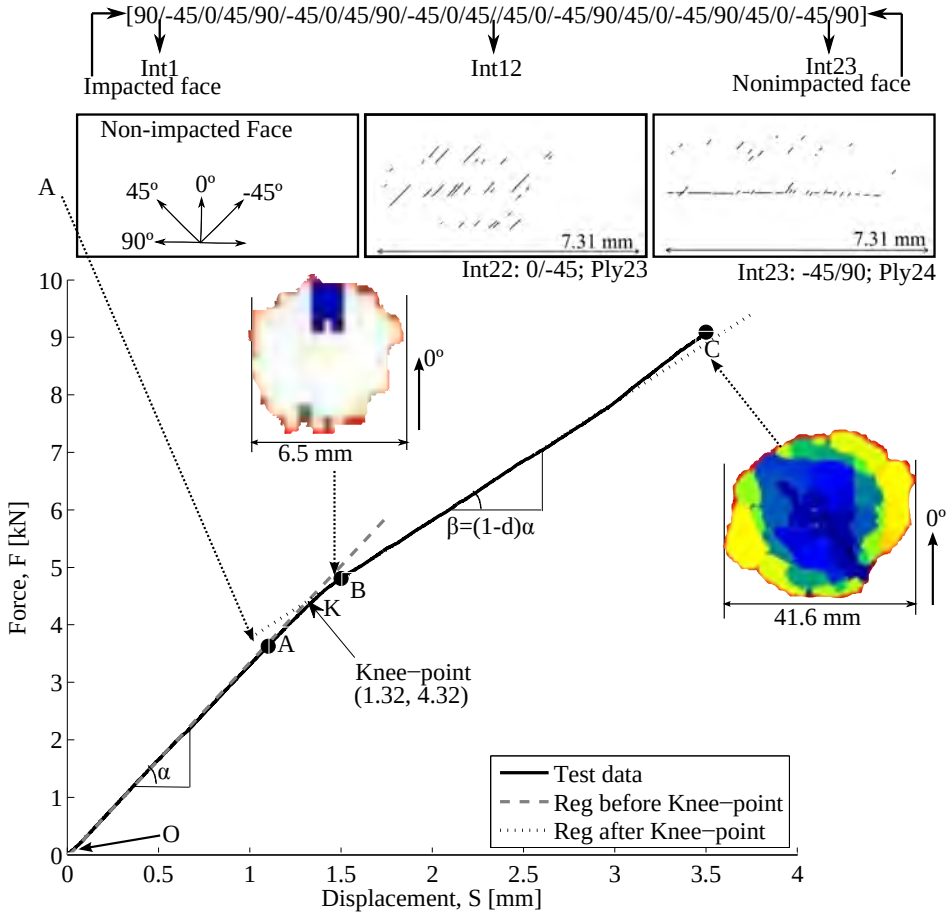

Stiffness loss: d=0.39

Applied indentation diplacement A: 1.1 mm ; B: 1.5 mm; C: 3.5 mm

Fig. 5.12: Mapping damage development onto representative load-deflection curve with images from CT at 1.1 mm and from C-Scan at 1.5 mm and 3.5 mm of applied displacement for LBA layup. LBA: $[90/-45/0/45]_{3s}$. Reg: Linear regression.

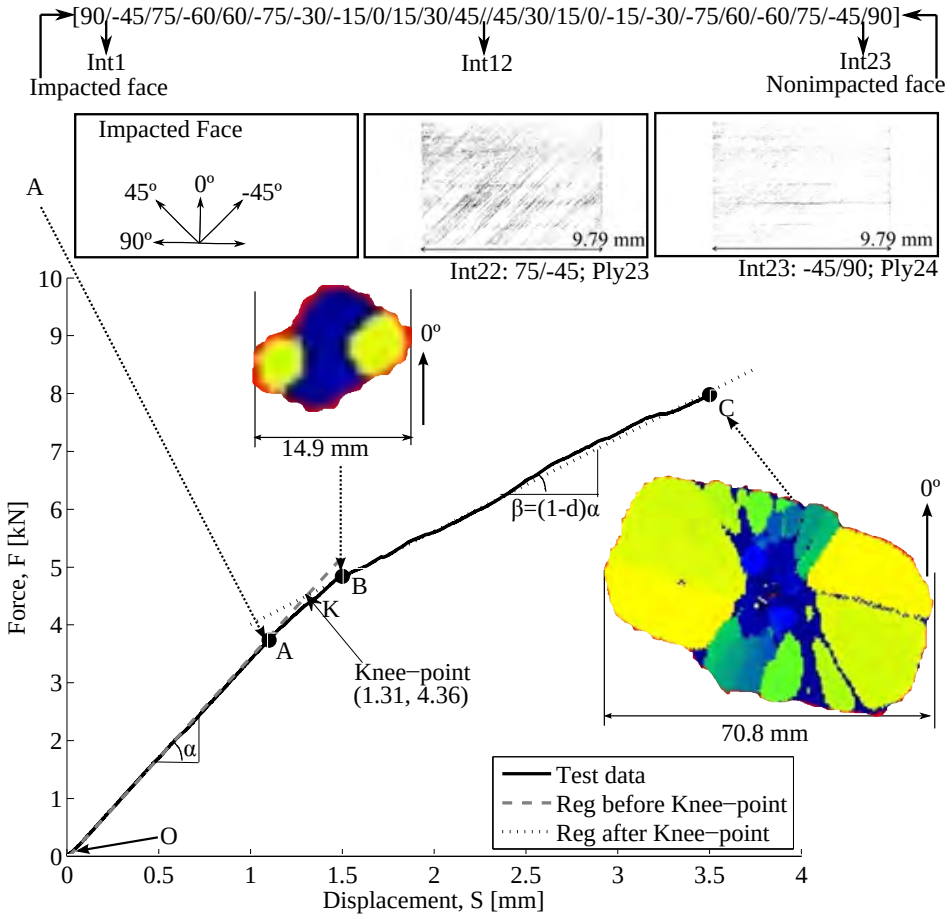

Stiffness loss: d=0.54

Applied indentation diplacement A: 1.1 mm ; B: 1.5 mm; C: 3.5 mm

Fig. 5.13: Mapping damage development onto representative load-deflection curve with images from CT at 1.1 mm and from C-Scan at 1.5 mm and 3.5 mm of applied displacement for LNC layup. LNC: $[90/-45/75/-60/60/-75/-30/-15/0/15/30/45]_s$. Reg: Linear regression.

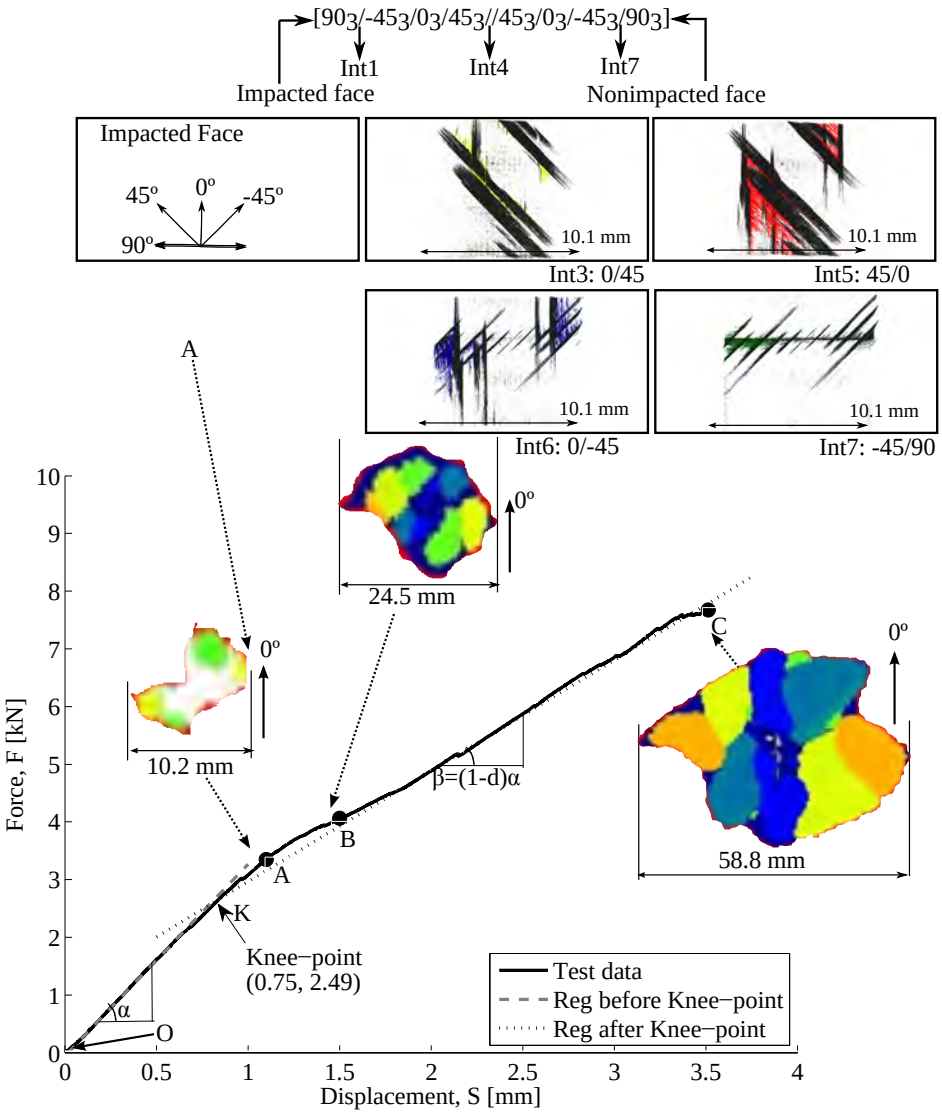

Fig. 5.14: Mapping damage development onto representative load-deflection curve with images from CT and C-Scan at 1.1 mm and from C-Scan at 1.5 mm and 3.5 mm of applied displacement for LTP layup. LTP: $[90_3/-45_3/0_3/45_3]_s$. Note that Int4 is the midplane interface, MMA=0º. Reg: Linear regression.

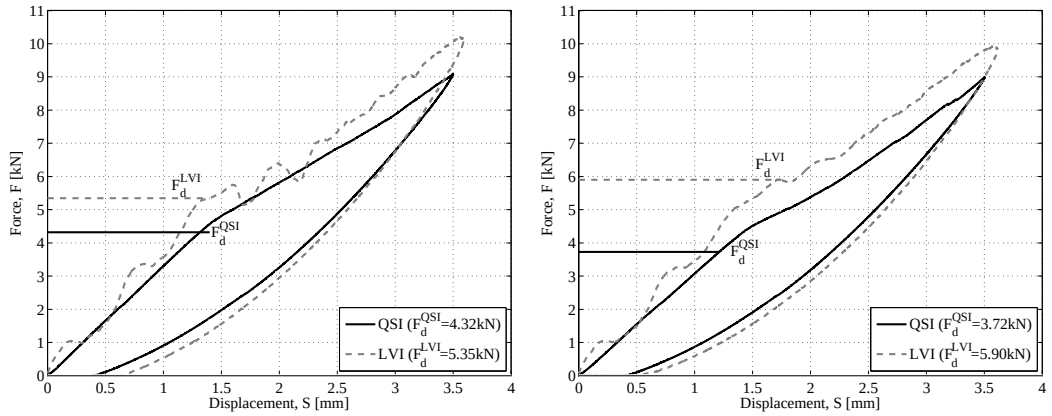

(a) LBA AR coupons

(b) LBA WET coupons

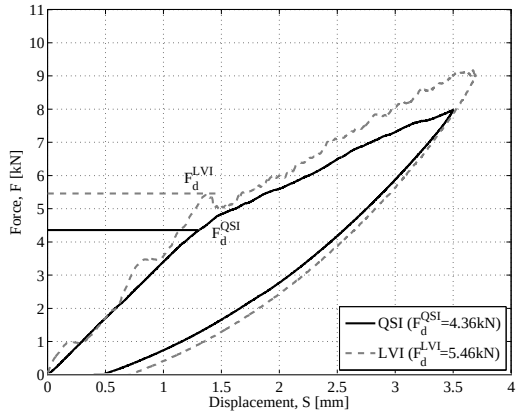

(c) LNC AR coupons

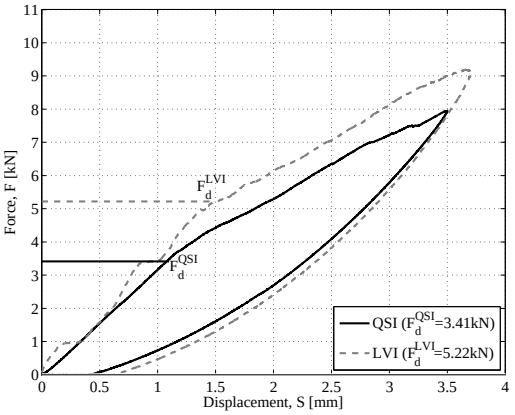

(d) LNC WET coupons

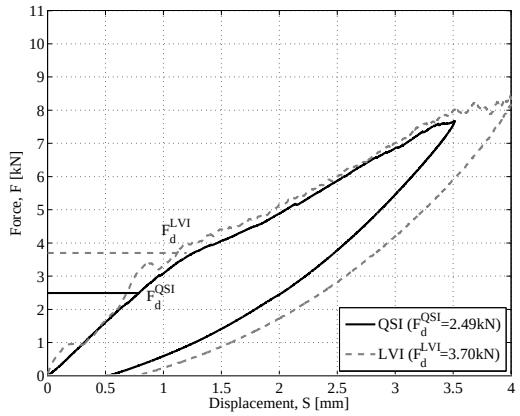

(e) LTP AR coupons

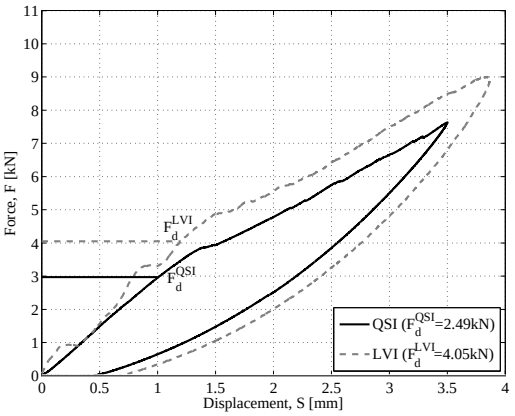

(f) LTP WET coupons

Fig. 5.15: Comparison of the responses between quasi-static indentation and low velocity impact.

C-Scan projected damage area A_{pro} against applied energy E_{app}
Fig. 5.16 shows the C-Scan A_{pro} measured from C-Scan against the E_{app}. For the quasi-static indentation test, the E_{app} was determined from the areas under the loading part of the load-deflection curves using trapezoidal numerical integration. For the impact case, the E_{app} is the impact energy itself. Fig. 5.16 demonstrates a strong linear relation in all the cases (three laminates, two loading types, two specimen conditions). The gradients of the linear regression lines for both loading types are almost the same with the exception of LTP AR specimens.

5.4 Discussion

5.4.1 Damage development

By combining the results from quasi-static indentation tests with the damage inspection from C-Scan and μCT, the laminate damage progression could be mapped on the global response of the laminates (Figs. 5.12–5.14). The matrix cracks always precede the observed delaminations except for the LTP. Indeed, the displacement of 1.1 mm for this layup is high enough to trigger multiple delaminations, thus hinders the matrix cracks to be seen in their isolation. The lowest indentation resulted in the presence of the matrix cracks themselves. Since no delaminations could be seen without the presence of the preceding matrix cracks, it can be concluded that the observed delaminations were induced by matrix cracking.

Despite the absence of dynamic components in QSI, it is difficult to identify a delamination threshold load F_d as no sudden load drop appears on the load-deflection curves (even at the displacement levels where extensive delaminations occurred). To determine F_d, the point at which the specimen stiffness changed was sought after by means of two linear regression lines, as shown in Figs. 5.12–5.14. The intercept between the two lines defines the threshold load, and named as the knee-point. This approach to identify an F_d may be subjective. Notwithstanding, the identified knee-point K lands on the load level before delaminations can be observed by either CT or C-Scan. Therefore, this knee-point can be reasonably attributed to the delamination propagation onset load, or the delamination threshold load as it is already well known. This absence of the load drop is really interesting and unlike the materials often reported in literature exhibit an obvious load drop, for example AS4/TC350 studied by Wagih et al. [5] and IM7/8552 by Abbiset et al [183]. The underpinning mechanism of the absence of the load drop is not clear to the authors, and a stable propagation of delaminations is speculated to be responsible for this phenomenon.

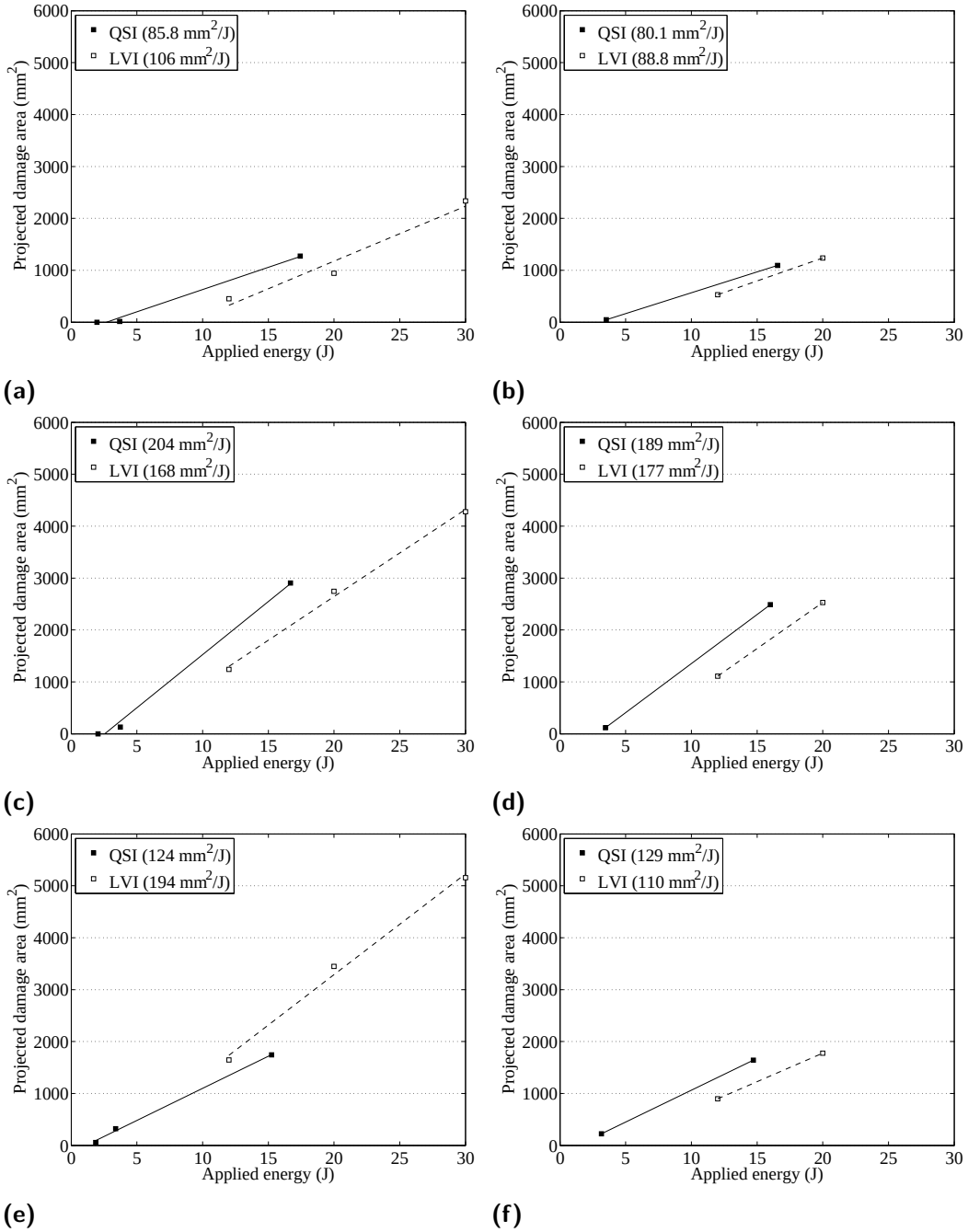

Fig. 5.16: C-scan projected damage areas against the energy applied for impact and quasi-static loading conditions of AR and WET specimens.

Regarding the laminate stiffness reduction, two remarks should be made. First, as observed from μCT at Point A in Figs. 5.12 and 5.13, in the part of the loading curve with the gradient α, the presence of the matrix cracks does not affect the laminate stiffness. Second, in the part of the loading curve with the gradient β, the load tends to increase linearly resulting in practically no loss of stiffness for all the layups (between points B and C). This is interesting because the propagation of delaminations from B to C enlarges the A_{pro} at least five times. These results appear to agree with the model of Suemasu et al. [184], which predicts that, under certain conditions during delamination propagation, the total delmainated area has a linear relationship with the applied energy.

Thanks to a good similarity in the response of three layups, their damage sequences within the range of indentation displacements of the composite system under study can be summarized in general as follows:

- Between O and K: the intralaminar matrix cracks can occur along the fibre direction in the plies located near bottom surface, although the load increases linearly with the applied displacement.

- At K: this knee-point is associated with the propagation onset of a number delaminations induced by intralaminar matrix cracks of plies above and below the delaminations.

- Between K and B: the range responds to the propagation of the delaminations that are developed at the knee-point K, and development of new delaminations at other interfaces; concurrently the relationship between the load and the applied displacement is nonlinear.

- Between B and C: this range sees the propagation of an existing number of delaminations developed at B, with the load increasing in a practically linear fashion with respect to the applied displacement.

Since delaminations were observed to be constrained by matrix cracks, future work should focus on understanding the development and interaction of the two failure mechanisms. Such investigation must also consider the effect of ply thickness and MMA together with their through-the-thickness positions. Both, as experimentally demonstrated in Chapter 4 and other studies [17, 18], can influence the impact damage morphology, which is closely linked to the compression after impact strengths. Some interesting insights have been reported in past studies regarding the topic of failure mechanism interaction [44, 50, 185, 186]. 2D and 3D FE studies [44, 50] reported that matrix crack-induced delamination propagation was dominated by mode II fracture, with mode I fracture contributing to the propagation onset. In [185], where $[0/\theta_n/90]_s$ was experimentally studied under tension loading, Yokozeki et al. found that decreasing either MMA with respect to the 90°-ply or the

θ-ply thickness gives rise to numerous short transverse matrix cracks in the θ-ply. Zheng and Sun [186] reported that interaction between two delaminations at a certain distance from one another resulted in a shielding effect, i.e. one preventing the other from further growth. Some of these findings highlight that efforts to model matrix cracked-induced delamination, as the one proposed by Zubillaga et al. [187], become even more relevant in predicting the impact damage morphology.

5.4.2 Moisture effect

Without the presence of dynamic components in QSI, moisture showed a consistent effect on the damage resistance of all the laminates: decreasing E_{dis}, δ_{ind}, and A_{pro} (Figs. 5.4–5.6). The decreased A_{pro} can be attributed to the matrix becoming tougher in the presence of moisture, as discussed for impact loading in Section 4.6, and reported in [126, 127, 182]. Smaller A_{pro} also implies less E_{dis} and lower δ_{ind}. More interestingly, the presence of moisture substantially reduced the sensitivity of thick-ply laminate to the loading rate as seen in Fig. 5.16e vs Fig. 5.16f. The difference in the gradients of LIV and QSI of LTP is 43%. An ongoing CT inspection on WET coupons remains to be done to provide more detailed evidence of the moisture influence on damage features, which will be reported in the near future. This sensitivity however disappears in WET condition, which is to be further discussed in the following section.

5.4.3 QSI and LVI

As observed in Fig. 5.15, the delamination threshold loads of LVI are consistently higher than those of quasi-static tests. In other words, the delamination threshold F_d^{LVI} is delayed under impact loading in comparison to its quasi-static counterpart F_d^{QSI}. These experimental results confirm the theoretical prediction by Olsson et al.[188], although the analysis was made for small mass impacts. In [188], F_d^{LVI} was shown to be 21.3% higher than F_d^{QSI} (F_d^{LVI}=1.213F_d^{QSI}). Following their derivation, the increase comes directly from the fact that the available energy release rate in impact G_{dyn} is lower than that in indentation G_{stat}, i.e. G_{dyn}=0.68G_{stat}. The energy balance based on linear fracture mechanics provides a straightforward explanation because part of the work done by the external force is transformed into the kinetic energy in addition to being transformed into the strain energy. In addition, QSI tests showed the undamaged and damaged parts on the load-deflection curves in the same fashion as those exhibited by LVI tests. To be precise, the stiffness degradation takes place once a delamination threshold load is reached with the gradients of LVI and QSI curves being almost the same, particularly after the delamination threshold. When compared to the C-Scan images of damaged areas due to LVI loading in Fig. 4.9, the C-Scan images due to QSI loading in Fig. 5.7 show a good similarity in overall damage morphology in terms of through-the-thickness positions and propagation

directions of delaminations. These similarities highlight the usefulness of QSI in capturing the responses of the LVI at the macroscopic level at the least.

Another aspect to be discussed is the loading rate effect due to LVI. The rate sensitivity is recognized by a noticeable difference between the gradients of two linear regression lines in the plot of A_{pro} against E_{app}, Fig. 5.16. The plot shows that, for the same applied energy, A_{pro} due to QSI is consistently higher than that caused by LVI with the exception of the LTP coupons tested under as-received (AR) condition (Fig. 5.16e). In LTP-AR case, LVI causes the A_{pro} to grow at a rate of 56% higher than QSI does. This large may be attributed to the combined effects of thick-ply on in-situ strengths [177] and loading on the interlaminar fracture toughness[189, 190]. This rate sensitivity highlights that evaluating the damage resistance of different layups must be cautiously done when QSI are used in lieu of LVI. The loading rate effect was also observed in toughened CFRPs tested at high energy levels [3]. Nonetheless, based on the load-deflection characteristics and C-Scan damage morphology, the loading rate effect may play a secondary role in the damage development. As a result, the experimental evidence provided by QSI can be a good asset for validating both analytical and numerical models.

6 Compressive strength of laminates with one embedded delamination

6.1 Overview

The literature survey on artificial impact damage study exposes the critical need to understand the influence of the through-the-thickness location of a single delamination on the compressive failure load of composite laminates, i.e. the maximum load-carrying capacity. Therefore, the main aim of this chapter is to deal with this topic considering both conventional and nonconventional laminates under compression loading. The FE model described in Section 3.6 was used to generate the results presented here. The discussion covers an explanation to the cause leading to low CAI strength of LNC presented in Chapter 4, and suggestions on how to improve the design of both conventional and nonconventional laminates. The content of this chapter fulfills the third objective stated in Section 1.3.

6.2 Layups and simulation test matrix

The numerical study considers eighteen layups; all are balanced, symmetric and quasi-isotropic. Their nomenclatures and short descriptions are given in Table 6.1. There are three groups of layups: LBA, LNC, and LNC-IV. Each group includes a stacking sequence which is rotated by a given angle. The group LBA contains two basic sequences: LBA and LBA-V3. Delamination diameters of 25, 50 and 75 mm were selected to study the influence of delamination sizes the compressive residual strength values. These three sizes were applied to only LBA and LNC. The rest were simulated with only 50 mm. The justification of this selected diameter will be provided later at the beginning of Section 6.4. The effect of the through-the-thickness position of the delamination was examined by locating it at an interface per simulation. In total, the test matrix contains 216 simulations, also summarized in Table 6.1.

LBA and LNC are the stacking sequences experimentally studied in Chapter 4. They are considered with the aim to understand the effect of size and through-the-thickness position of the delamination on the failure load. This numerical study can

serve to comprehend the causes of the low CAI strength in LNC observed in Chapter 4.

The conventional layup group permits assessing the influence of delamination position and stacking sequence on the compressive strength. Note that LBA-V3 is a variant layup of LBA, created by exposing $\pm$ 45 plies to the laminate surfaces. This idea mimics the current design philosophy for preventing global buckling [95]. It is also supported by the study conducted by Hitchen and Kemp [48], who found that $\pm$ 45 surface sublaminate is more damage tolerant. As a result, a MMA of 90° appears in this layup and the ones derived by its rotation. Placing 0°-ply on a laminate surface is not recommended in the design of conventional laminates. Thus, the layup rotation was done to result in only $\pm$45 or 90° as the surface ply. This set of conventional layups, though small, represents the stacking sequences commonly found in industrial applications.

Recalling the LNC architecture in Fig. 4.1, its definition seeks for large MMAs within the bottom sublaminate and small MMAs in the central one, with large MMAs also present in the top sublaminate due to symmetry constraint. Studying the listed nonconventional layups was stimulated by the desire to see how LNC definition can be modified to anticipate the CAI strength enhancement. The hypothesis is that not only the positions of the sublaminates influences the compressive strength of delaminated plates, but also do the ply orientations of the sublaminates. The findings may be used as guidelines for designing a nonconventional layup. To this end, a simple set of operations were done on the original LNC layup:

- Firstly, LNC was rotated by an increment of 15° or 30° to reach to a 90° rotation. As a result, small MMAs at central sublminate and large MMAs at bottom and top sublaminates are preserved, but the ply orientations of the sublaminates are not.

- Secondly, LNC stacking sequence was reversed to derive LNC-IV layup, by moving the ply at the laminate midplane to the laminate surface, and so on. This resulted in the positions of the sublaminates being exchanged.

- Lastly, LNC-IV was rotated with an increment of 15° or 30° to arrive at 90° rotation. As a result, large MMAs at central sublaminate and small MMAs at bottom and top sublaminates are preserved, but the ply orientations of the sublaminates are not. This enables the study of the effect of both position and ply orientation of the sublaminates.

According to the classical laminate theory, rotating the original LNC sequence by 90° results in the increase in A_{11} stiffness term of the top sublaminate and the decrease in A_{11} stiffness term of the central sublaminate along the loading direction. The opposite effect occurs when LNC-IV is rotated by 90°. It should be mentioned that the

0°-ply at the laminate surface was not avoided as was done in the conventional layup group. Indeed, Sebaey et el. [17] reported the increase in the CAI strength although a cluster of two 0° plies were placed at the laminate surface of the nonconventional layup.

6.3 Results

Fig. 6.1 summarizes the failure loads against the delamination depth (through-the-thickness position) of both LBA and LNC for the three delamination sizes considered. As the delamination depth approaches the midplane (Int12), failure loads tend to increase in both laminates, for 25 and 50 mm delamination in particular. The interfaces Int1 to Int6 are not affected by the delamination size as much as are the interfaces Int7 to Int12. Regardless of the delamination size, the maximum difference in the failure loads of all interfaces is 25.4% for the LBA layup. Disregarding the delamination size of 75 mm, the LNC layup results in the increase of 30.5% in the failure load when the delamination is located at deep interfaces.

Presented in Fig. 6.2 is the failure loads of the conventional layup group. Failure loads of delaminations at deep interfaces are consistently higher than those near the laminate surface. The failure loads increase almost monotonically for deep interfaces. For near-surface interfaces, the load-carrying capacity drops at Int3 or Int4, depending on the layups. An exception to this occurrence is the case of layup LBA-V3+90°.

The failure loads against the delamination depth of the 12 nonconventional layups are presented in Fig. 6.3, for nonconventional LNC and inverse nonconventional LNC-IV families respectively. Unlike the conventional layups, the load-bearing capacity of the nonconventional laminates strongly depends on the layups. In other words, they are quite sensitive to the loading direction. The increasing trend in terms of delamination depth disappears when the LNC is rotated by 15 and 30°, and appears again when layup rotation approaches 60°. For the LNC-IV family, the trend is surprisingly diverse before layup rotation reaches 75°.

6.4 Discussion

A remark on delamination sizes should be made before discussing the effect of the delamination depth on the CAI strength. To begin with, the C-Scan image of LNC indented at 3.5 mm was enhanced to provide richer information as in Fig. 6.4. The short line with the doubled head red arrows represents the delamination length of the delaminations at the deep interfaces; i.e., the central sublaminate. This length was measured to be only 47 mm. Therefore, the results for 75-mm delamination

Tab. 6.1: Layups and simulation text matrix. Positive direction of layup rotation is anti-clockwise. Symbol // marks the end of sublaminate with small MMA (15°) in nonconventional layups.

Layup ID	Shorthand description	Stacking sequence	Delamination (mm)	No. of simulations
Conventional laminates				
LBA	Baseline	$[90/\text{-}45/0/45]_{3s}$	25, 50, 75	36
LBA-V1	LBA+45°	$[\text{-}45/0/45/90]_{3s}$	50	12
LBA-V2	LBA-45°	$[\text{-}45/90/45/0]_{3s}$	50	12
LBA-V3	± 45 on laminate surface	$[\text{-}45/45/0/90]_{3s}$	50	12
LBA-V4	LBA-V3+90°	$[\text{-}45/45/90/0]_{3s}$	50	12
LBA-V5	LBA-V3-45°	$[90/0/\text{-}45/45]_{3s}$	50	12
Nonconventional laminates				
LNC	Nonconventional	$[90/\text{-}45/75/\text{-}60/60/\text{-}75//\text{-}30/\text{-}15/0/15/30/45]_{s}$	25, 50, 75	36
LNC-V1	LNC+15°	$[\text{-}75/\text{-}30/90/\text{-}45/75/\text{-}60//\text{-}15/0/15/30/45/60]_{s}$	50	12
LNC-V2	LNC+30°	$[\text{-}60/\text{-}15/\text{-}75/\text{-}30/90/\text{-}45//0/15/30/45/60/75]_{s}$	50	12
LNC-V3	LNC+60°	$[\text{-}30/15/\text{-}45/0/\text{-}60/\text{-}15//30/45/60/75/90/\text{-}75]_{s}$	50	12
LNC-V4	LNC+75°	$[\text{-}15/30/\text{-}30/15/\text{-}45/0//45/60/75/90/\text{-}75/\text{-}60]_{s}$	50	12
LNC-V5	LNC+90°	$[0/45/\text{-}15/30/\text{-}30/15//60/75/90/\text{-}75/\text{-}60/\text{-}45]_{s}$	50	12
Inverse layup of nonconventional laminates				
LNC-IV	Inverse nonconventional	$[45/30/15/0/\text{-}15/\text{-}30//\text{-}75/60/\text{-}60/75/\text{-}45/90]_{s}$	50	12
LNC-IV1	LNC-IV+15°	$[60/45/30/15/0/\text{-}15//\text{-}60/75/\text{-}45/90/\text{-}30/\text{-}75]_{s}$	50	12
LNC-IV2	LNC-IV+30°	$[75/60/45/30/15/0//\text{-}45/90/\text{-}30/\text{-}75/\text{-}15/\text{-}60]_{s}$	50	12
LNC-IV3	LNC-IV+60°	$[\text{-}75/90/75/60/45/30//\text{-}15/\text{-}60/0/\text{-}45/15/\text{-}30]_{s}$	50	12
LNC-IV4	LNC-IV+75°	$[\text{-}60/\text{-}75/90/75/60/45//0/\text{-}45/15/\text{-}30/30/\text{-}15]_{s}$	50	12
LNC-IV5	LNC-IV+90°	$[\text{-}45/\text{-}60/\text{-}75/90/75/60//15/\text{-}30/30/\text{-}15/45/0]_{s}$	50	12

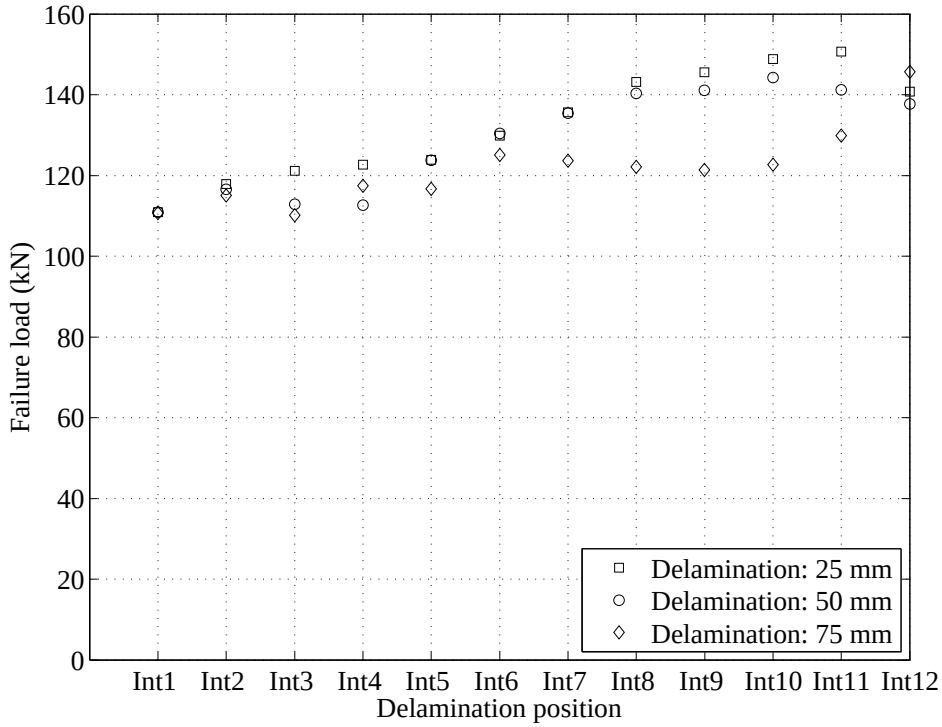

(a) LBA: $[90/\text{-}45/0/45]_{3s}$

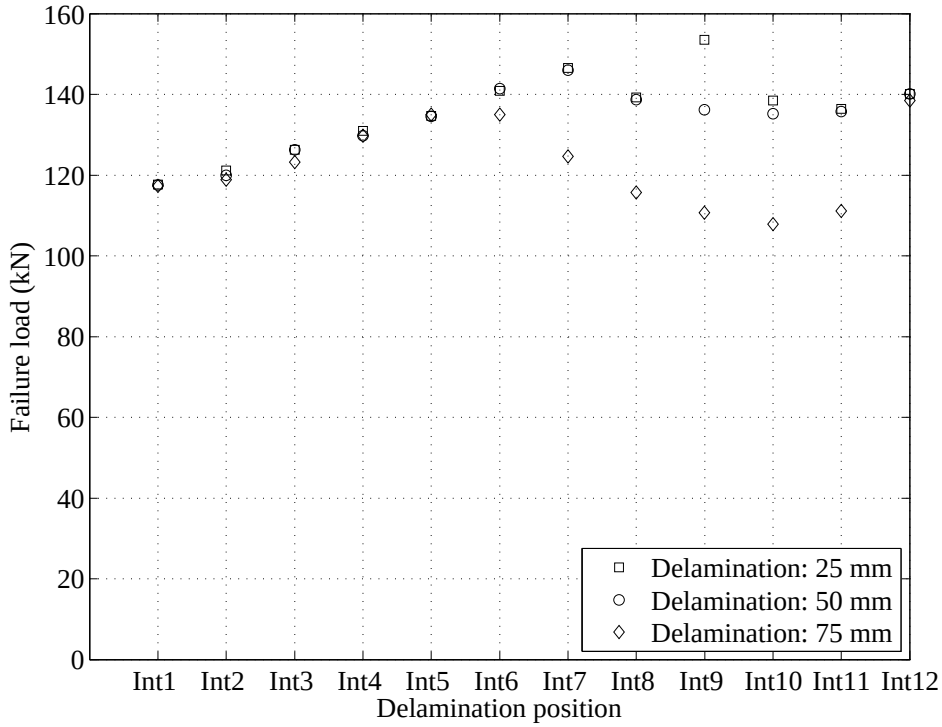

(b) LNC: $[90/\text{-}45/75/\text{-}60/60/\text{-}75/\text{-}30/\text{-}15/0/15/30/45]_{s}$

Fig. 6.1: Variation of failure loads against through-the-thickness positions for three delamination sizes.

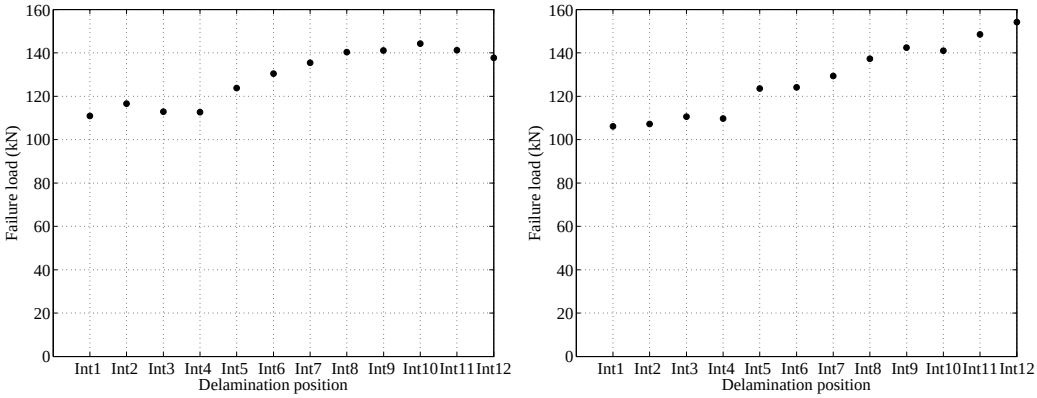

(a) LBA: $[90/-45/0/45]_{3s}$

(b) LBA+45° ($[-45/0/45/90]_{3s}$)

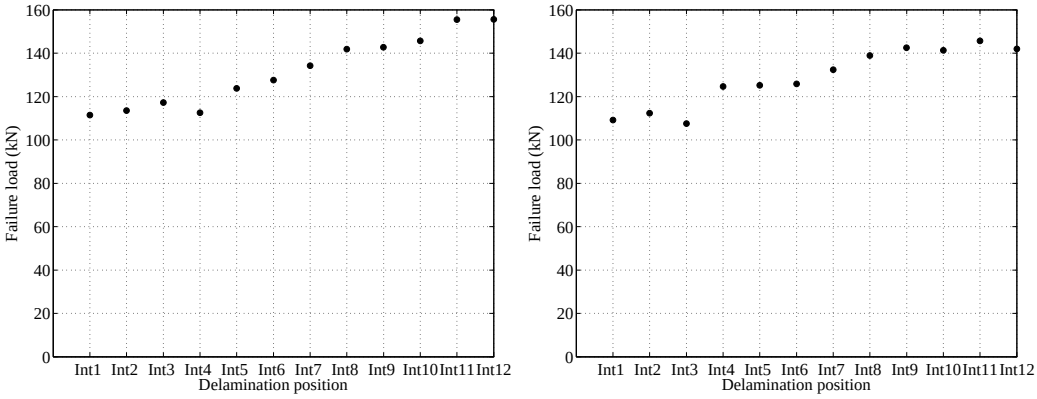

(c) LBA-45° ($[-45/90/45/0]_{3s}$)

(d) LBA-V3: $[-45/45/0/90]_{3s}$

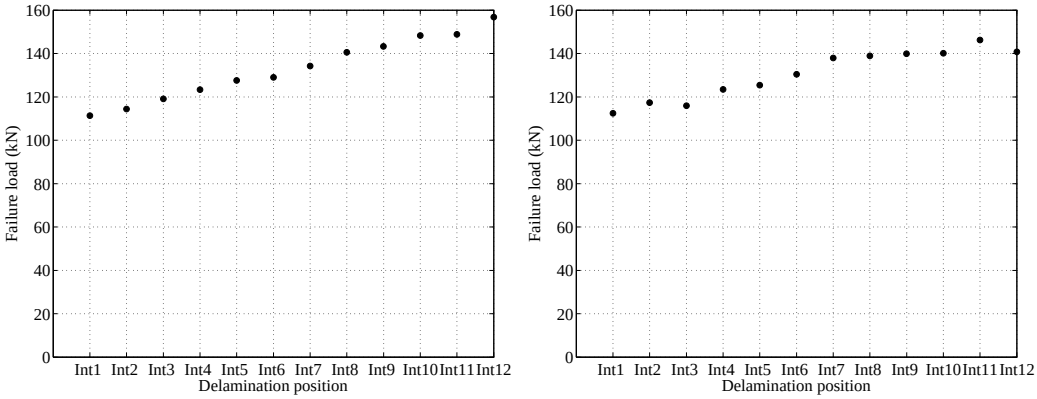

(e) LBA-V3+90° ($[-45/45/90/0]_{3s}$)

(f) LBA-V3-45° ($[90/0/-45/45]_{3s}$)

Fig. 6.2: Load carrying capacity of conventional layups for delamination size D = 50 mm.

.

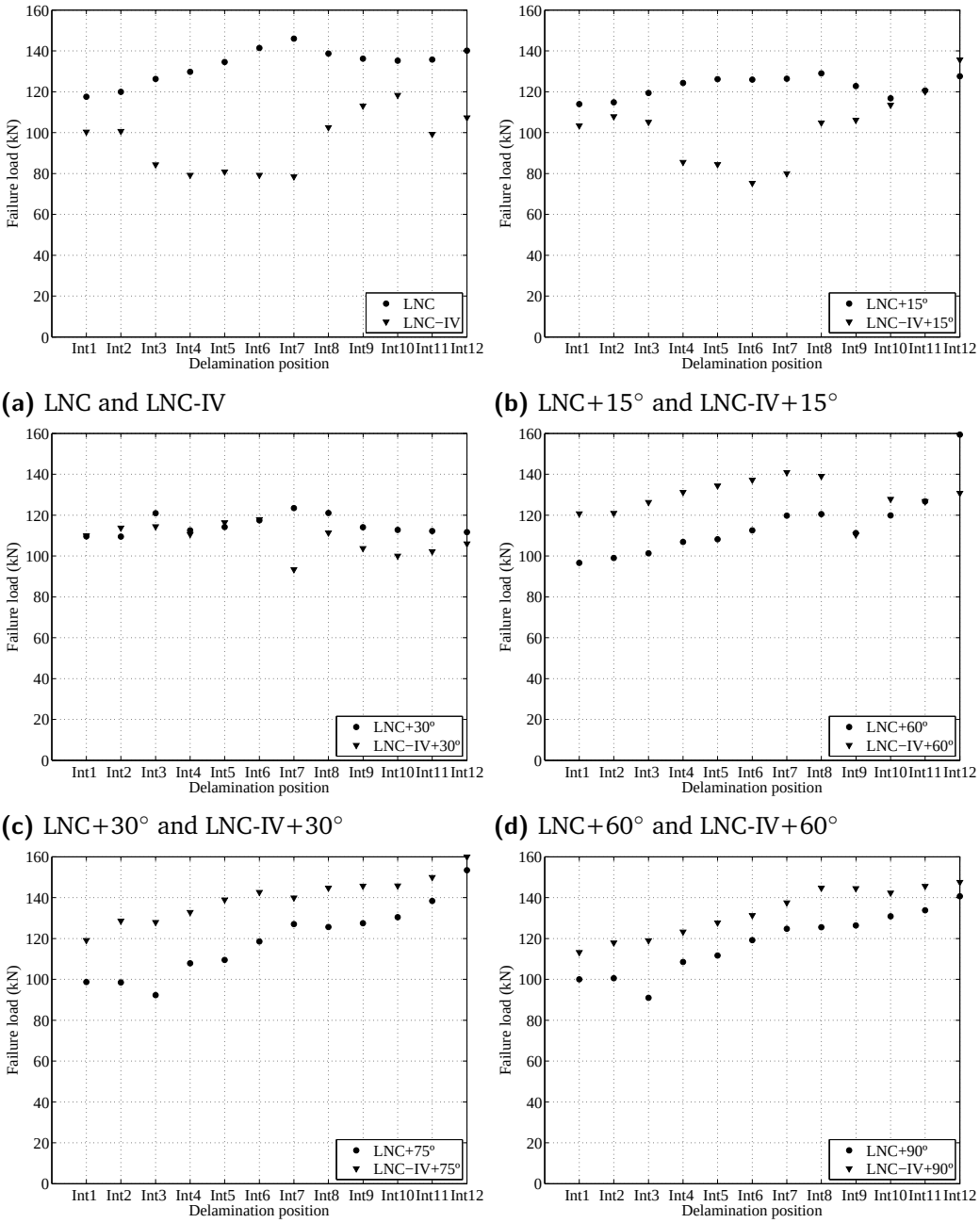

(a) LNC and LNC-IV

(b) LNC+15° and LNC-IV+15°

(c) LNC+30° and LNC-IV+30°

(d) LNC+60° and LNC-IV+60°

(e) LNC+75° and LNC-IV+75°

(f) LNC+90° and LNC-IV+90°

Fig. 6.3: Failure loads of inverse nonconventional layups LNC, LNC-IV and their rotated layups for delamination size D = 50 mm.
LNC: $[90/-45/75/-60/60/-75/-30/-15/0/15/30/45]_s$
LNC-IV: $[45/30/15/0/-15/-30/-75/60/-60/75/-45/90]_s$

.

case is most likely unrealistic and can be disregarded in the rest of the discussion. This consideration is even more meaningful for the conventional laminate as its delaminations are smaller.

6.4.1 Reasoning behind low CAI strength of LNC

The first topic to be discussed is the case of low CAI strength in LNC observed in Chapter 4. Before proceeding, the intention of LNC is briefly recalled here. LNC was defined such that the bottom sublaminate has large MMAs in order to experience large delaminations, and that the central sublaminate has small MMAs so as to experience small or no delaminations. As such, the CAI strength was anticipated to increase thanks to the almost-intact central sublaminate helping to bear the compression load. The hypothesis regarding small and large delaminations resulting from MMA selection was corroborated by the C-Scan results presented in Chapters 4 and 5. Nonetheless, the experimental results showed no CAI strength enhancement in the LNC.

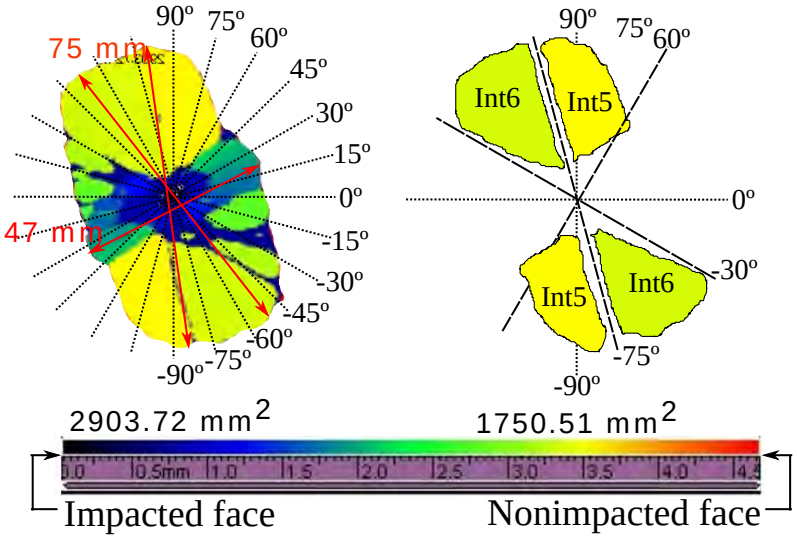

Fig. 6.4: C-Scan of LNC indented at 3.5 mm illustrating large delaminations, their positions and the estimates of their associated delaminated areas.

Based on Fig. 6.4, two large delaminations are identified at Int5 and Int6 from unimpacted face. Their total delaminated areas accounts for more than 60% of the entire projected delamination area. The effect of multiple delaminations on compressive strength values has been observed to be substantial. The experimental work of Laman et al. [191] showed that three circular delaminations could decrease the compressive strength of one circular delamination up to 36%. This effect was reported on layup $[45/90/-45/0]_{2s}$ with delaminations placed at interfaces 1 to 3 from the laminate surface. It is also important to note that the delamination at Int6 is oriented about 90° to the loading direction. The effect of orientation was earlier

reported in previous studies [134, 139], where the sublaminate buckling load was observed to decrease when the elliptical delamination major axis was rotated from 0° to 90°. Since the CAI failure sequence is triggered by the sublaminate buckling, as reviewed in Section 2.2.2, the delamination orientations at Int5 and Int6 of the LNC laminate must also be responsible for lowering CAI strength. Recognizing the effect of delaminations at shallow interfaces as per Fig. 6.1b as well as the number and orientations of delamination on the compressive strength, the low CAI strength in LNC can be attributed to the delaminations identified.

6.4.2 Conventional layup group

The second topic of discussion turns to the case of conventional layups. The increasing trend of failure loads in terms of delamination depth shows up in all the considered stacking sequences. The results provide the first convincing evidence that deep delaminations are less harmful to the compression strength in the conventional layup family, for all the 12 interfaces are considered. This can be attributed to the observation that mode II fracture dominates delamination growth onset at deep interfaces. Such behaviour was confirmed during the validation study of the FE model, see Figs. 9.2-9.5 of Appendix 9.1. Since mode II fracture requires higher energy to cause crack advance than the mode I does, the instability triggered by sublaminate buckling is delayed under compression. The delayed instability can contribute to the increased compression strength.

Indeed, it has been suggested that delaminations at deep interfaces could be beneficial under compression [91, 94, 95, 192]. However, no sufficient experimental or numerical results was reported. In [192], the authors considered 1D delaminated isotropic struts and demonstrated that there existed a critical depth where sublaminate buckling mode changed from opening to closing mode. From this finding, Butler et al. [91] suggested deeper sited delaminations may be considered to be safe because they will open under inplane compressive loading and hence they should not grow to cause failure. Their subsequent studies [94, 95] attributed the 40% improvement in CAI strength with layup $[\pm 45_4/(90/0)_4]_s$ to the largest delamination at Int8 (between -45° and 90° plies). They reasoned that this location is deep enough to delay buckling and result in high damage tolerance.

The finding presented in this chapter also encourages the development of laminated plates that force delaminations to occur at deep interfaces. In this regard, the study by Saito et al. [121] is found relevant. In [121], thin-ply laminates provided 23% higher in CAI strength than the standard ply-based laminates. SEM examination revealed that the former incur only one large delamination at the midplane and few matrix cracks whereas the latter showed multiple delaminations and more matrix cracks. Some approaches that can be exploited to benefit from the delamination

depth have already existed: reinforcing interfaces to enhance toughness of interfaces close to the laminate surface (Int1-Int6), mixing thin-thick plies in layup design and hybridizing different fibre types. A few examples of the approaches to enhancing interlaminar toughness include interleaving the interfaces with veil or thermoplastic particles and z-pinning.

6.4.3 Nonconventional layup group

The third theme to be discussed involves how LNC definition should be modified in order to enhance the CAI strength. This idea was examined by a sequence of operations on the LNC layup, see description in Section 6.2. Results show LNC group is quite sensitive to layup rotations or stacking sequences, see Fig. 6.3. The merit of delamination depth appears on five layups: LNC, LNC+75°, LNC+90°, LNC-IV+75°, and LNC-IV+90°. In terms of load carrying capacity, LNC, LNC+75° and LNC+90° outperform the rest of the group. These three laminates share two common traits:

- Central sublaminate is stiffer in the loading direction; i.e., $A_{11} > A_{22}$.
- Top and bottom sublaminates are softer in the loading direction; i.e., $A_{11} < A_{22}$.

Under impact loading, the delamination is observed to elongate along the fibre direction of the lower ply. Considering the extrinsic link between impact damage morphology and CAI strength, LNC+75° and LNC+90° deserves to be studied experimentally/numerically because they not only promote large delaminations at deep interfaces but also have ply orientations aligned toward the loading direction. In line with how to take advantages of the delamination depth, the following are suggested to guide nonconventional layup design with the loading direction parallel to the 0°-ply:

- Top and bottom sublaminates shall have small MMAs in order to minimize delamination sizes as shallow interfaces are less damage tolerant to compressive loading.
- Top and bottom sublaminates shall have ply orientations aligned towards 90° with respect to the loading axis.
- Central sublaminates shall have large MMAs in order to promote delamination as deep interfaces are more damage tolerant to compressive loading.
- Central sublaminates shall have ply orientations aligned towards the loading axis in order to help bear the compressive load thus directly reducing delamination extension in the 90° with respect to the loading axis.

Part IV

Conclusions and Future Work

7 Conclusions

> *One fact well understood by observation, and well guided development, is worth a thousand times more than a thousand words.*
>
> **— American Journal of Education, 1858**

C-Scan inspection proved that, by selecting mismatch angle (MMA) between plies, it is feasible to predetermine the location of delaminations through the thickness of the nonconventional laminate (LNC). While this did not result in an improvement of CAI strength in LNC, it did result in an increase in strength retention after impact (more noticeably in WET condition). In fact, the compressive strength can not be compared directly because LNC possesses one third of the 0° plies that LBA has, consequently lowering its effective load-carrying capacity under compression.

Blocking three plies impaired the impact resistance as well as the compressive strength of pristine and impacted specimens.

While moisture tends to improve damage resistance and tolerance with respect to the AR counterparts, its effect is far greater on thick-ply laminate (e.g. increasing F_d and decreasing A_{pro}). Under compression loading, moisture decreases the compressive strength of the non-impacted coupons, but the influence on the impacted coupons is diverse.

The delaminations resulted from QSI loading are considered to be induced by matrix cracking because no delaminations are visible without the presence of their preceding matrix cracks.

The absence of a clear load drop on the force-displacement curves of QSI loading is attributed to a stable propagation of delaminations for the composite system under study.

Without the presence of dynamic components in QSI, moisture has shown a consistent effect on the damage resistance of all the laminates: decreasing E_{dis}, δ_{ind}, and A_{pro}. The decreased A_{pro} can be attributed to the matrix becoming tougher in the presence of moisture.

QSI tests can be used to observe the chronology of damage development in LVI tests because the overall damage morphology of delaminations and load-deflection curves

exhibit the same essential characteristics (shapes, positions and orientations of the dealminations as well as the stiffness degradation in the global response).

The loading rate effect on the damage development mechanisms may be considered to have a secondary effect on the failure mode development because the aforementioned essential characteristics could be still be observed (even in the thick-ply laminate which exhibits a pronounced sensitivity to the effect).

Numerical results have shown the increasing trend of failure loads in terms of delamination depth in all the considered conventional stacking sequences but not in all the nonconventional ones. This means that taking advantage of the delamination depth is more straightforward in the former than in the latter.

Recognizing the demerit of delaminations located far from the midplane and the influence of the number and orientation of delaminations on the compressive strength, the low CAI strength in LNC can be attributed to the delaminations identified at Int5 and Int6, not to mention the lack of 0°-plies which help to bear the compressive load.

The CAI strength of the conventional layups may be efficiently enhanced by avoiding delaminations in Int1 to Int6 so that delaminations are forced to occur near the midplane. This approach may also help to reduce the extensive damage to the fibre as observed in other studies where all interfaces are toughened. Extensive fibre fracture in 0°-ply means a significant loss of load-carrying capacity.

Given that the nonconventional layup group is sensitive to the loading direction, the following are recommended to guide the design of such laminates with the aim to exploit the merit of the delamination depth and orientation assuming that the loading direction is parallel to the 0°-ply:

- Top and bottom sublaminates shall have small MMAs in order to minimize delamination sizes because the delaminated interfaces in these regions are found to be less damage tolerant to compressive loading.
- Top and bottom sublaminates shall have ply orientations aligned towards 90° with respect to the loading axis in order to have lower A_{11}, thus delaying the delamination growth in these regions.
- Central sublaminates shall have large MMAs in order to promote delamination because delaminated interfaces in these regions are found to be more damage tolerant to compressive loading.
- Central sublaminates shall have ply orientations aligned towards the loading axis in order to help bear the compressive load, thus directly reducing delamination extension in the 90° with respect to the loading axis.

8 Future work

> *Science and technology are the most important worldwide cooperative project. They do not advance by great leaps but by many small steps.*
>
> **— Unknown**

Various possibilities can be envisaged to continue this study:

- Perform μCT inspection of the WET coupons tested in Chapter 5 and compare the damage morphology to their AR counterparts by postprocessing their μCT images. The results will serve as a source of concrete evidence of detailed damage mechanisms for developing either analytical or numerical tools that better predict the impact damage morphology. Furthermore, an FE model with a more reliable impact damage morphology can be exploited to identify the CAI strength-controlling parameters.

- Extend the capability of the FE model developed in Chapter 6 such that it can simulate laminates containing multiple delaminations of different sizes, shapes and/or orientations. Such a model will offer more relevant insights regarding the CAI behaviour.

- Considering the extrinsic link between impact damage morphology and CAI strength, LNC+75° and LNC+90° (Chapter 6) deserves to be studied numerically and/or experimentally because they not only promote large delaminations at deep interfaces but also have ply orientations aligned toward the loading direction.

- Mixing thin- and thick-plies together with small and large MMAs offers a great opportunity to exploit the synergistic effect on controlling delamination locations for CAI strength improvement.

Appendix

9

9.1 Energy release rate along delamination front

This Appendix provides the results that support the argument made in the first paragraph of the discussion of Section of the 6.4.2. That is, during the validation study of the FE model developed in Section 3.6, the mode II fracture was observed to dominate the delamination growth behaviour at the onset of propagation at deep interfaces i.e. Int6 to Int12 (see Figs. 9.2-9.5). G_I, G_{II}, G_{III} are the components of the available energy release rate along the delamination front in the three fracture modes. G_{Ic}, G_{IIc}, G_{IIIc} are the components of the critical energy release rate along the delamination front. Fig. 9.1 illustrates the angle describing the position along delamination front where the components of energy release rate were output from the model. G_I/G_{Ic}, G_{II}/G_{IIc} and G_{III}/G_{IIIc} are the ratio of different modes of the energy release rate. The validation study was to compare the capability of the FE model to predict the global behaviour (Fig. 3.19) and delamination growth direction (Fig. 3.18) presented in the experimental study Reeder et al. [169]. Note that no significant differences in the onset growth direction were observed whether the model considers only VCCT or VCCT together with the brittle fibre breakage except at Int12.

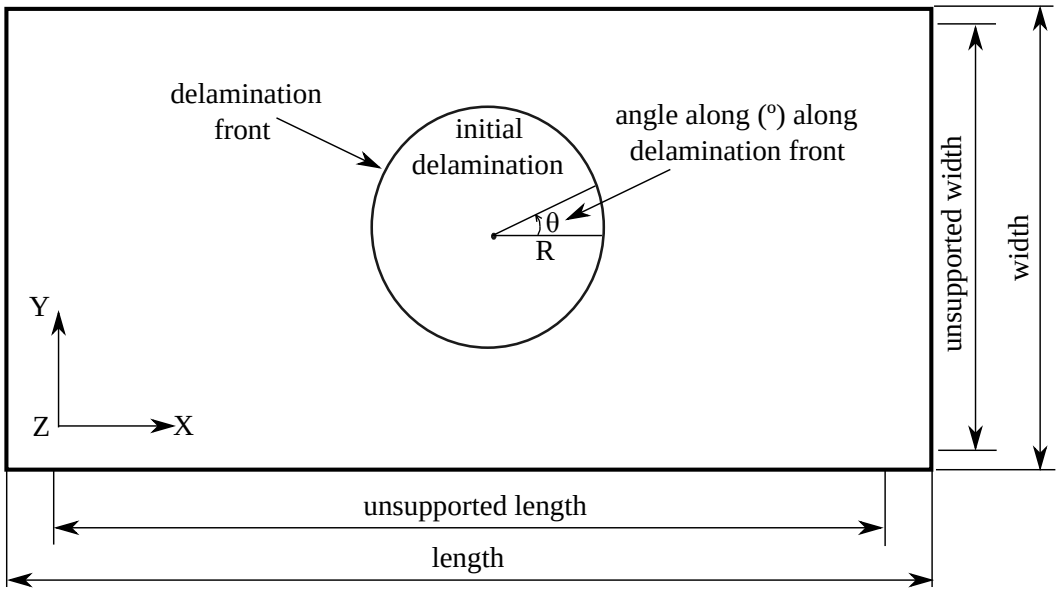

Fig. 9.1: Showing the angle describing the position along delamination front inside the in-plane view of the FE model geometry.

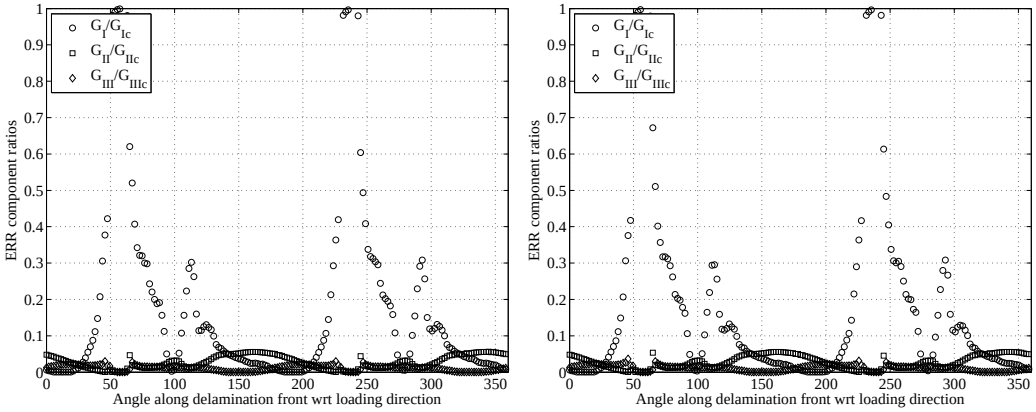

(a) Int1: VCCT

(b) Int1: VCCT+Hashin

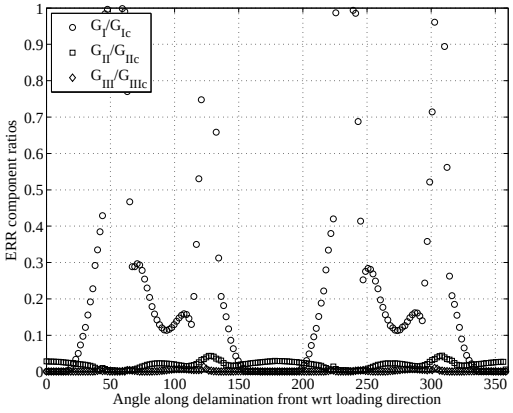

(c) Int2: VCCT

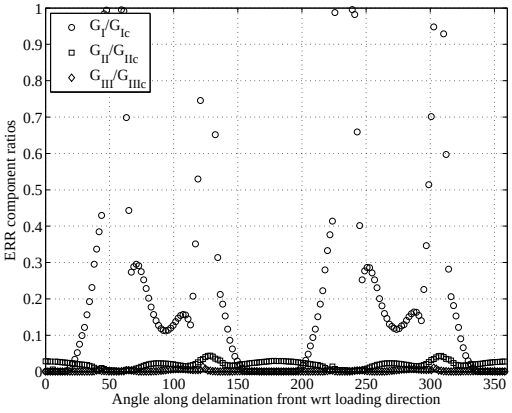

(d) Int2: VCCT+Hashin

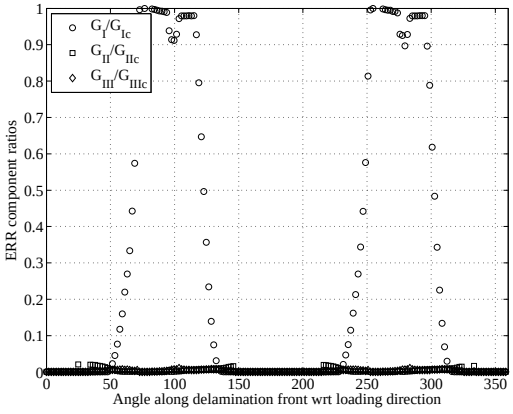

(e) Int3: VCCT

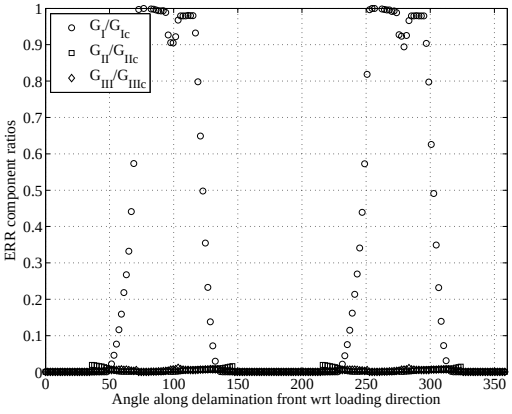

(f) Int3: VCCT+Hashin

Fig. 9.2: Components of energy release rate ratios along delamination front of Int1, Int2, and Int3.

.

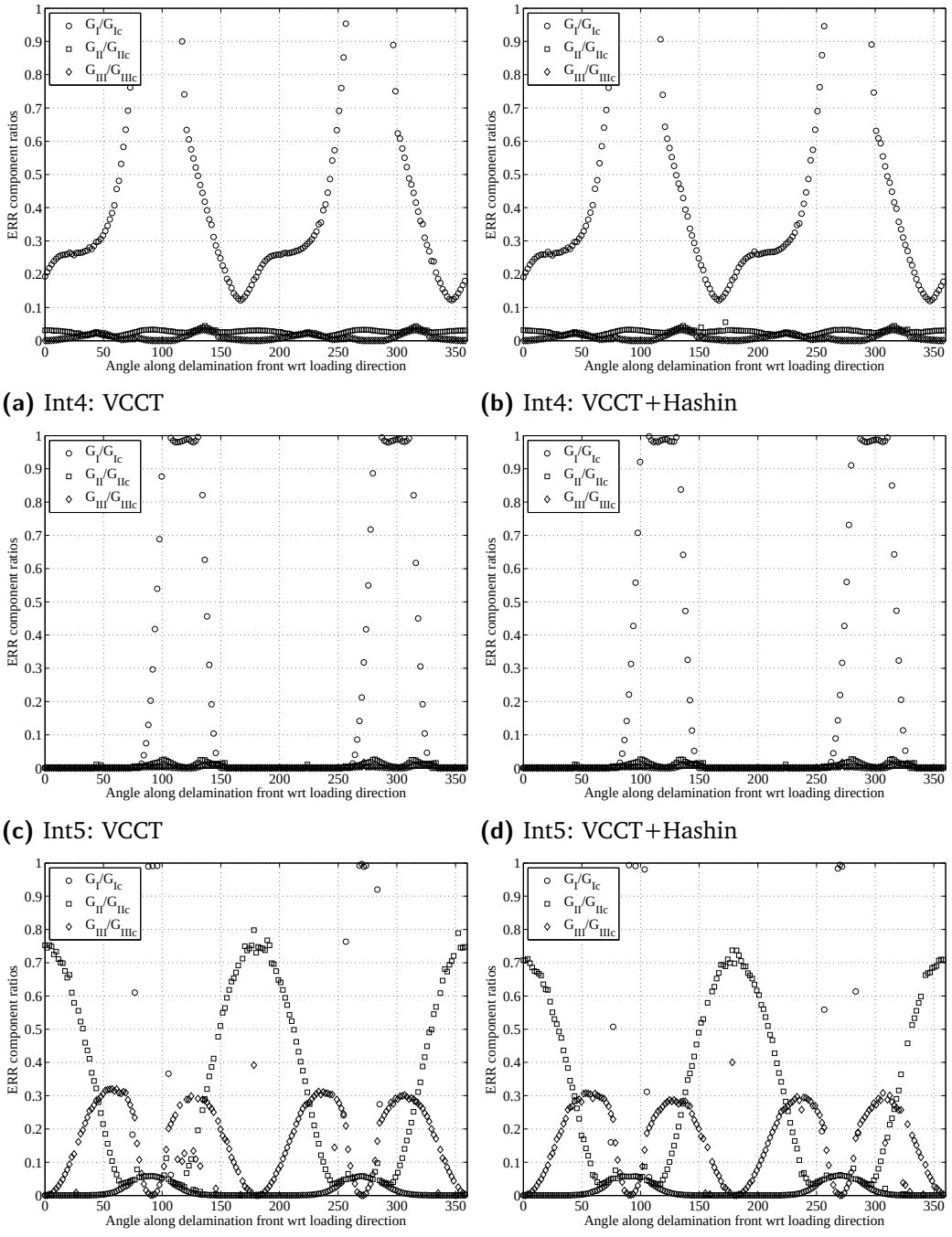

(a) Int4: VCCT **(b)** Int4: VCCT+Hashin

(c) Int5: VCCT **(d)** Int5: VCCT+Hashin

(e) Int6: VCCT **(f)** Int6: VCCT+Hashin

Fig. 9.3: Components of energy release rate ratios along delamination front of Int4, Int5, and Int6.

.

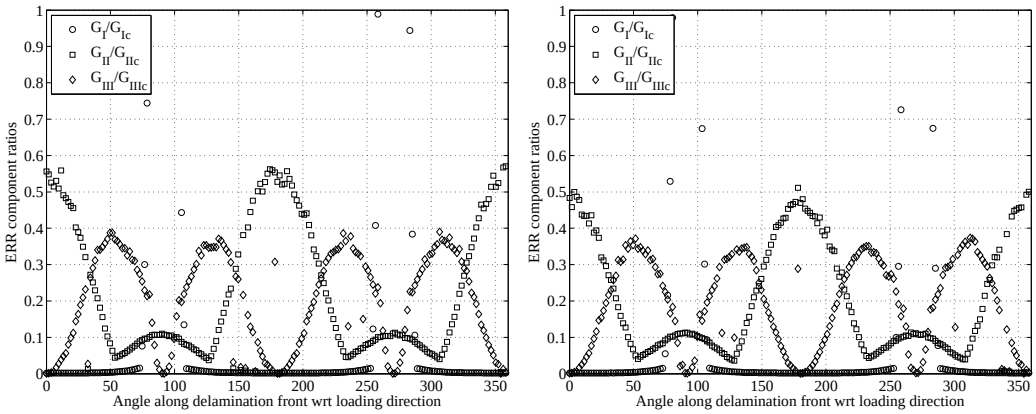

(a) Int7: VCCT

(b) Int7: VCCT+Hashin

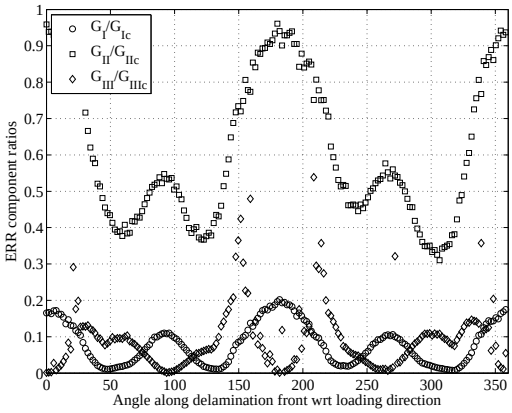

(c) Int8: VCCT

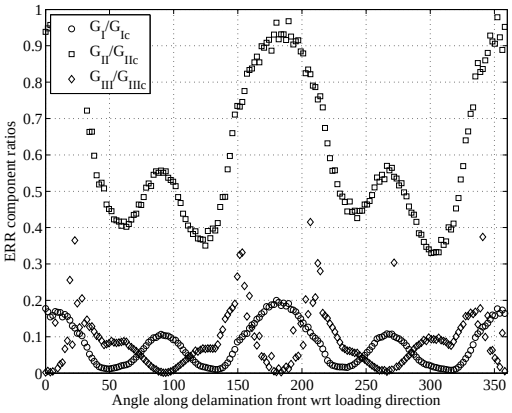

(d) Int8: VCCT+Hashin

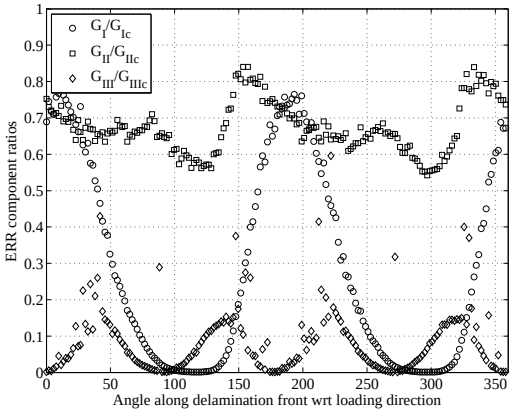

(e) Int9: VCCT

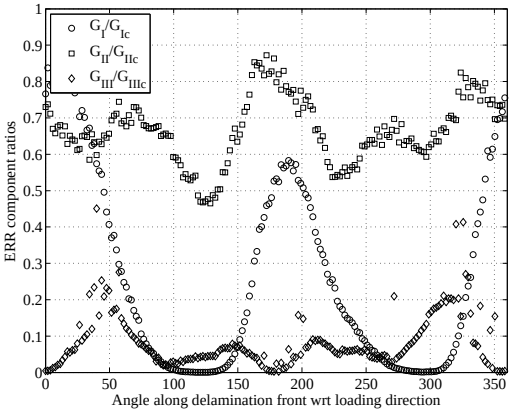

(f) Int9: VCCT+Hashin

Fig. 9.4: Components of energy release rate ratios along delamination front of Int7, Int8, and Int9.

.

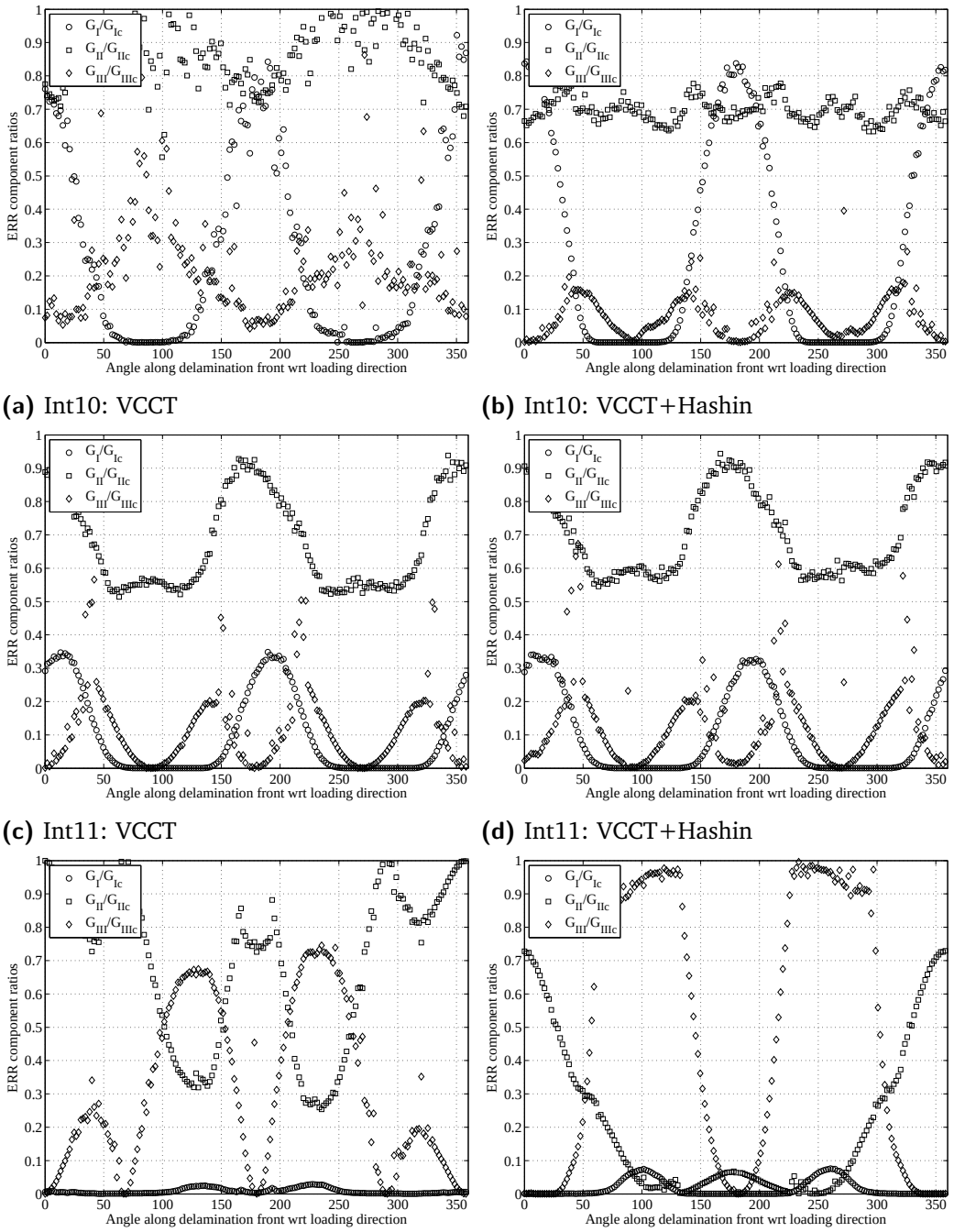

(a) Int10: VCCT **(b)** Int10: VCCT+Hashin

(c) Int11: VCCT **(d)** Int11: VCCT+Hashin

(e) Int12: VCCT **(f)** Int12: VCCT+Hashin

Fig. 9.5: Components of energy release rate ratios along delamination front of Int10, Int11, and Int12.

.

Bibliography

[1] Philippe H Geubelle and Jeffrey S Baylor. “Impact-induced delamination of composites: a 2D simulation”. In: *Composites Part B: Engineering* 29.5 (1998), pp. 589 –602 (cit. on p. 3).

[2] M. de Freitas, A. Silva, and L. Reis. “Numerical evaluation of failure mechanisms on composite specimens subjected to impact loading”. In: *Composites Part B: Engineering* 31.3 (2000), pp. 199 –207 (cit. on p. 3).

[3] D. J. Bull, S. M. Spearing, and I. Sinclair. “Investigation of the response to low velocity impact and quasi-static indentation loading of particle-toughened carbon-fibre composite materials”. In: *Composites Part A: Applied Science and Manufacturing* 74.0 (2015), pp. 38–46 (cit. on pp. 3, 107).

[4] F. Caputo, A. De Luca, and R. Sepe. “Numerical study of the structural behaviour of impacted composite laminates subjected to compression load”. In: *Composites Part B: Engineering* 79 (2015), pp. 456 –465 (cit. on p. 3).

[5] A. Wagih, P. Maimí, N. Blanco, and J. Costa. “A quasi-static indentation test to elucidate the sequence of damage events in low velocity impacts on composite laminates”. In: *Composites Part A: Applied Science and Manufacturing* 82 (2016), pp. 180 –189 (cit. on pp. 3, 9, 85, 103).

[6] Erdem Selver, Prasad Potluri, Paul Hogg, and Costas Soutis. “Impact damage tolerance of thermoset composites reinforced with hybrid commingled yarns”. In: *Composites Part B: Engineering* 91 (2016), pp. 522 –538 (cit. on p. 3).

[7] D. Guédra-Degeorges. “Recent advances to assess mono- and multi-delaminations behaviour of aerospace composites”. In: *Composites Science and Technology* 66.6 (2006). Advances in statics and dynamics of delamination Workshop on Advances in Modeling Delamination in Composite Materials and Structures, pp. 796–806 (cit. on p. 3).

[8] Hiroshi Suemasu, Wataru Sasaki, Takashi Ishikawa, and Yuichiro Aoki. “A numerical study on compressive behavior of composite plates with multiple circular delaminations considering delamination propagation”. In: *Composites Science and Technology* 68.12 (2008). Deformation and Fracture of Composites: Analytical, Numerical and Experimental Techniques, with regular papers, pp. 2562 –2567 (cit. on pp. 3, 46).

[9] Samuel Rivallant, Christophe Bouvet, and Natthawat Hongkarnjanakul. “Failure analysis of CFRP laminates subjected to compression after impact: FE simulation using discrete interface elements”. In: *Composites Part A: Applied Science and Manufacturing* 55 (2013), pp. 83 –93 (cit. on pp. 3, 12–14, 17, 26).

[10]D. J. Bull, S. M. Spearing, and I. Sinclair. “Observations of damage development from compression-after-impact experiments using ex situ micro-focus computed tomography”. In: *Composites Science and Technology* 97 (2014), pp. 106 –114 (cit. on pp. 3, 10, 11, 13–20, 23, 35).

[11]V.J. Hawyes, P.T. Curtis, and C. Soutis. “Effect of impact damage on the compressive response of composite laminates”. In: *Composites Part A: Applied Science and Manufacturing* 32.9 (2001), pp. 1263 –1270 (cit. on pp. 3, 25, 26).

[12]K. Ogi, H. S. Kim, T. Maruyama, and Y. Takao. “The influence of hygrothermal conditions on the damage processes in quasi-isotropic carbon/epoxy laminates”. In: *Composites Science and Technology* 59.16 (1999), pp. 2375 –2382 (cit. on pp. 3, 36).

[13]J. I. Cauich-Cupul, E. Pérez-Pacheco, A. Valadez-González, and P. J. Herrera-Franco. “Effect of moisture absorption on the micromechanical behavior of carbon fiber/epoxy matrix composites”. English. In: *Journal of Materials Science* 46.20 (2011), pp. 6664–6672 (cit. on pp. 3, 37).

[14]E. Pérez-Pacheco, J. I. Cauich-Cupul, A. Valadez-González, and P. J. Herrera-Franco. “Effect of moisture absorption on the mechanical behavior of carbon fiber/epoxy matrix composites”. English. In: *Journal of Materials Science* 48.5 (2013), pp. 1873–1882 (cit. on pp. 3, 37).

[15]C. S. Lopes, O. Seresta, Y. Coquet, et al. “Low-velocity impact damage on dispersed stacking sequence laminates. Part I: Experiments”. In: *Composites Science and Technology* 69.7–8 (2009), pp. 926–936 (cit. on pp. 3, 5, 34, 74).

[16]T. A. Sebaey, E. V. González, C. S. Lopes, N. Blanco, and J. Costa. “Damage resistance and damage tolerance of dispersed CFRP laminates: Design and optimization”. In: *Composite Structures* 95.0 (2013), pp. 569–576 (cit. on pp. 3, 5, 34, 74).

[17]T. A. Sebaey, E. V. González, C. S. Lopes, N. Blanco, and J. Costa. “Damage resistance and damage tolerance of dispersed CFRP laminates: Effect of ply clustering”. In: *Composite Structures* 106.0 (2013), pp. 96–103 (cit. on pp. 3, 5, 23, 24, 34, 85, 105, 111).

[18]T. A. Sebaey, E. V. González, C. S. Lopes, et al. “Damage resistance and damage tolerance of dispersed CFRP laminates: Effect of the mismatch angle between plies”. In: *Composite Structures* 101.0 (2013), pp. 255–264 (cit. on pp. 3–5, 23, 34, 105).

[19]Edgar Fuoss, Paul V. Straznicky, and Cheung Poon. “Effects of stacking sequence on the impact resistance in composite laminates–Part 1: parametric study”. In: *Composite Structures* 41.1 (1998), pp. 67 –77 (cit. on pp. 4, 73, 85).

[20]E.V. González, P. Maimí, P.P. Camanho, C.S. Lopes, and N. Blanco. “Effects of ply clustering in laminated composite plates under low-velocity impact loading”. In: *Composites Science and Technology* 71.6 (2011), pp. 805 –817 (cit. on pp. 4, 85).

[21]Silvia Hernández Rueda. “Curing, Defects and Mechanical Performance of Fiber-Reinforced Composites”. PhD thesis. Universidad Politécnica de Madrid, 2013 (cit. on pp. 4, 85).

[22]Raghunath P. Khetan and David C. Chang. “Surface Damage of Sheet Molding Compound Panels Subject to a Point Impact Loading”. In: *Journal of Composite Materials* 17.2 (1983), pp. 182–194 (cit. on p. 7).

[23]W.J. Cantwell and J. Morton. “Detection of impact damage in CFRP laminates”. In: *Composite Structures* 3.3 (1985), pp. 241 –257 (cit. on p. 7).

[24]Derek Hull and Yi Bing Shi. “Damage mechanism characterization in composite damage tolerance investigations”. In: *Composite Structures* 23.2 (1993), pp. 99 –120 (cit. on pp. 7, 9, 11, 12).

[25]Digby D Symons. “Characterisation of indentation damage in 0/90 lay-up T300/914 CFRP”. In: *Composites Science and Technology* 60.3 (2000), pp. 391 –401 (cit. on p. 7).

[26]F. Aymerich and W.J. Staszewski. “Impact damage detection in composite laminates using nonlinear acoustics”. In: *Composites Part A: Applied Science and Manufacturing* 41.9 (2010). Special Issue on 10th Deformation & Fracture of Composites Conference: Interfacial interactions in composites and other applications, pp. 1084 –1092 (cit. on p. 7).

[27]K.T. Tan, N. Watanabe, and Y. Iwahori. “X-ray radiography and micro-computed tomography examination of damage characteristics in stitched composites subjected to impact loading”. In: *Composites Part B: Engineering* 42.4 (2011), pp. 874 –884 (cit. on p. 7).

[28]Bo Yang, Yaoda Huang, and Long Cheng. “Defect detection and evaluation of ultrasonic infrared thermography for aerospace CFRP composites”. In: *Infrared Physics & Technology* 60 (2013), pp. 166 –173 (cit. on p. 7).

[29]K.T. Tan, A. Yoshimura, N. Watanabe, Y. Iwahori, and T. Ishikawa. “Effect of stitch density and stitch thread thickness on damage progression and failure characteristics of stitched composites under out-of-plane loading”. In: *Composites Science and Technology* 74 (2013), pp. 194 –204 (cit. on p. 7).

[30]D.J. Bull, L. Helfen, I. Sinclair, S.M. Spearing, and T. Baumbach. “A comparison of multi-scale 3D X-ray tomographic inspection techniques for assessing carbon fibre composite impact damage”. In: *Composites Science and Technology* 75 (2013), pp. 55 –61 (cit. on p. 7).

[31]Christian Garnier, Marie-Laetitia Pastor, Florent Eyma, and Bernard Lorrain. “The detection of aeronautical defects in situ on composite structures using Non Destructive Testing”. In: *Composite Structures* 93.5 (2011), pp. 1328 –1336 (cit. on p. 8).

[32]F. Aymerich and P. Priolo. “Characterization of fracture modes in stitched and unstitched cross-ply laminates subjected to low-velocity impact and compression after impact loading”. In: *International Journal of Impact Engineering* 35.7 (2008), pp. 591 –608 (cit. on pp. 8, 35).

[33]Tien-Wei Shyr and Yu-Hao Pan. “Impact resistance and damage characteristics of composite laminates”. In: *Composite Structures* 62.2 (2003), pp. 193 –203 (cit. on p. 9).

[34]Hyung Yun Choi, Hsi-Yung T. Wu, and Fu-Kuo Chang. “A New Approach toward Understanding Damage Mechanisms and Mechanics of Laminated Composites Due to Low-Velocity Impact: Part II—Analysis”. In: *Journal of Composite Materials* 25.8 (1991), pp. 1012–1038 (cit. on p. 8).

[35]M.O.W. Richardson and M.J. Wisheart. “Review of low-velocity impact properties of composite materials”. In: *Composites Part A: Applied Science and Manufacturing* 27.12 (1996), pp. 1123 –1131 (cit. on pp. 8, 11).

[36] Serge Abrate. *Impact on composite structures*. Cambridge university press, 1998 (cit. on p. 9).

[37] G. Zhou. "The use of experimentally-determined impact force as a damage measure in impact damage resistance and tolerance of composite structures". In: *Composite Structures* 42.4 (1998), pp. 375 –382 (cit. on p. 9).

[38] Ramesh Talreja. "Assessment of the fundamentals of failure theories for composite materials". In: *Composites Science and Technology* 105 (2014), pp. 190 –201 (cit. on p. 9).

[39] L.E. Asp, L.A. Berglund, and R. Talreja. "Prediction of matrix-initiated transverse failure in polymer composites". In: *Composites Science and Technology* 56.9 (1996), pp. 1089 –1097 (cit. on p. 9).

[40] L.E. Asp, L.A. Berglund, and R. Talreja. "A criterion for crack initiation in glassy polymers subjected to a composite-like stress state". In: *Composites Science and Technology* 56.11 (1996), pp. 1291 –1301 (cit. on p. 9).

[41] Peter O. Sjoblom, J. Timothy Hartness, and Tobey M. Cordell. "On Low-Velocity Impact Testing of Composite Materials". In: *Journal of Composite Materials* 22.1 (1988), pp. 30–52 (cit. on p. 9).

[42] G. Minak, M. Fotouhi, and M. Ahmadi. "6- Low-velocity impact on laminates". In: *Dynamic Deformation, Damage and Fracture in Composite Materials and Structures*. Ed. by Vadim V. Silberschmidt. Woodhead Publishing Series in Composites Science and Engineering. Woodhead Publishing, 2016, pp. 147 –165 (cit. on p. 10).

[43] D. Guédra-Degeorges. "Recent advances to assess mono- and multi-delaminations behaviour of aerospace composites". In: *Composites Science and Technology* 66.6 (2006), pp. 796 –806 (cit. on pp. 10, 11, 13, 16).

[44] C. Bouvet, S. Rivallant, and J.J. Barrau. "Low velocity impact modeling in composite laminates capturing permanent indentation". In: *Composites Science and Technology* 72.16 (2012), pp. 1977 –1988 (cit. on pp. 10–12, 105).

[45] F.J. Guild, P.J. Hogg, and J.C. Prichard. "A model for the reduction in compression strength of continuous fibre composites after impact damage". In: *Composites* 24.4 (1993), pp. 333 –339 (cit. on pp. 11, 26).

[46] A.F. Johnson, N. Toso-Pentecôte, and D. Schueler. "18 - Numerical modelling of impact and damage tolerance in aerospace composite structures". In: *Numerical Modelling of Failure in Advanced Composite Materials*. Ed. by Pedro P. Camanho and Stephen R. Hallett. Woodhead Publishing Series in Composites Science and Engineering. Woodhead Publishing, 2015, pp. 479 –506 (cit. on p. 11).

[47] S. Hong and D. Liu. "On the relationship between impact energy and delamination area". In: *Experimental Mechanics* 29.2 (1989), pp. 115–120 (cit. on p. 11).

[48] S.A. Hitchen and R.M.J. Kemp. "The effect of stacking sequence on impact damage in a carbon fibre/epoxy composite". In: *Composites* 26.3 (1995), pp. 207 –214 (cit. on pp. 11, 110).

[49] L. Reis and M. de Freitas. "Damage growth analysis of low velocity impacted composite panels". In: *Composite Structures* 38.1 (1997), pp. 509 –515 (cit. on pp. 11, 13, 14, 16).

[50]Y.-B. Shi and A.F. Yee. “Intraply crack and delamination interaction in laminate beams under transverse loading”. In: *Composite Structures* 29.3 (1994), pp. 287 –297 (cit. on pp. 11, 105).

[51]G. A. O. Davies and R. Olsson. “Impact on composite structures”. In: *The Aeronautical Journal* 108 (1089 Nov. 2004) (cit. on p. 11).

[52]E González. “Simulation of interlaminar and intralaminar damage in polymer-based composites for aeronautical applcations under impact loading”. PhD thesis. Universitat de Girona, 2010 (cit. on p. 12).

[53]Sandrine Petit, Christophe Bouvet, Alain Bergerot, and Jean-Jacques Barrau. “Impact and compression after impact experimental study of a composite laminate with a cork thermal shield”. In: *Composites Science and Technology* 67.15–16 (2007), pp. 3286 –3299 (cit. on pp. 12, 23).

[54]A. Elias, F. Laurin, M. Kaminski, and L. Gornet. “Experimental and numerical investigations of low energy/velocity impact damage generated in 3D woven composite with polymer matrix”. In: *Composite Structures* 159 (2017), pp. 228 –239 (cit. on p. 12).

[55]J.-H. Kim, F. Pierron, M.R. Wisnom, and S. Avril. “Local stiffness reduction in impacted composite plates from full-field measurements”. In: *Composites Part A: Applied Science and Manufacturing* 40.12 (2009). Special Issue: CompTest 2008, pp. 1961 –1974 (cit. on p. 12).

[56]Samuel Rivallant, Christophe Bouvet, Elias Abi Abdallah, Bernhard Broll, and Jean-Jacques Barrau. “Experimental analysis of CFRP laminates subjected to compression after impact: The role of impact-induced cracks in failure”. In: *Composite Structures* 111 (2014), pp. 147 –157 (cit. on pp. 12, 14–17).

[57]B. Vieille, V.M. Casado, and C. Bouvet. “Influence of matrix toughness and ductility on the compression-after-impact behavior of woven-ply thermoplastic- and thermosetting-composites: A comparative study”. In: *Composite Structures* 110 (2014), pp. 207 –218 (cit. on pp. 12, 27).

[58]Bataxi, Xi Chen, Zhefeng Yu, Hai Wang, and Cees Bil. “Strain Monitoring on Damaged Composite Laminates Using Digital Image Correlation”. In: *Procedia Engineering* 99 (2015), pp. 353 –360 (cit. on p. 12).

[59]V Arumugam, A Adhithya Plato Sidharth, and C Santulli. “Failure modes characterization of impacted carbon fibre reinforced plastics laminates under compression loading using acoustic emission”. In: *Journal of Composite Materials* 48.28 (2014), pp. 3457–3468 (cit. on pp. 12, 14).

[60]V. Arumugam, A. Adhithya Plato Sidharth, and C. Santulli. “Characterization of failure modes in compression-after impact of glass–epoxy composite laminates using acoustic emission monitoring”. In: *Journal of the Brazilian Society of Mechanical Sciences and Engineering* 37.5 (2015), pp. 1445–1455 (cit. on pp. 12, 14).

[61]J. Jefferson Andrew, V. Arumugam, D.J. Bull, and H.N. Dhakal. “Residual strength and damage characterization of repaired glass/epoxy composite laminates using A.E. and D.I.C”. In: *Composite Structures* 152 (2016), pp. 124 –139 (cit. on p. 12).

[62]S. Sanchez-Saez, E. Barbero, R. Zaera, and C. Navarro. “Compression after impact of thin composite laminates”. In: *Composites Science and Technology* 65.13 (2005), pp. 1911 –1919 (cit. on pp. 13, 16).

[63] M. de Freitas and L. Reis. “Failure mechanisms on composite specimens subjected to compression after impact”. In: *Composite Structures* 42.4 (1998). International Workshop on Experimental Techniques in the Analysis of Composite Structures, pp. 365 –373 (cit. on p. 13).

[64] E.V. González, P. Maimí, P.P. Camanho, A. Turon, and J.A. Mayugo. “Simulation of drop-weight impact and compression after impact tests on composite laminates”. In: *Composite Structures* 94.11 (2012), pp. 3364 –3378 (cit. on pp. 13, 26).

[65] Wei Tan, Brian G. Falzon, Louis N.S. Chiu, and Mark Price. “Predicting low velocity impact damage and Compression-After-Impact (CAI) behaviour of composite laminates”. In: *Composites Part A: Applied Science and Manufacturing* 71 (2015), pp. 212 –226 (cit. on pp. 13–15, 17, 21, 22, 26).

[66] J. T. Ruan, F. Aymerich, J. W. Tong, and Z. Y. Wang. “Optical Evaluation on Delamination Buckling of Composite Laminate with Impact Damage”. In: *Advanced Composite Materials* 2014.1 (2014), pp. 1–9 (cit. on p. 14).

[67] F.A. Habib. “A new method for evaluating the residual compression strength of composites after impact”. In: *Composite Structures* 53.3 (2001), pp. 309 –316 (cit. on p. 16).

[68] H. Chai, W. G. Knauss, and C. D. Babcock. “Observation of damage growth in compressively loaded laminates”. In: *Experimental Mechanics* 23.3 (1983), pp. 329–337 (cit. on p. 16).

[69] Hao Yan, Caglar Oskay, Arun Krishnan, and Luoyu Roy Xu. “Compression-after-impact response of woven fiber-reinforced composites”. In: *Composites Science and Technology* 70.14 (2010), pp. 2128 –2136 (cit. on pp. 16, 17).

[70] C. Soutis and P.T. Curtis. “Prediction of the post-impact compressive strength of CFRP laminated composites”. In: *Composites Science and Technology* 56.6 (1996), pp. 677 –684 (cit. on pp. 16, 25, 26).

[71] Chen Puhui, Shen Zhen, and Wang Junyang. “A New Method for Compression After Impact Strength Prediction of Composite Laminates”. In: *Journal of Composite Materials* 36.5 (2002), pp. 589–610 (cit. on pp. 16, 25, 26).

[72] M R Wisnom. “The role of delamination in failure of fibre-reinforced composites”. In: *Philosophical Transactions of the Royal Society of London A: Mathematical, Physical and Engineering Sciences* 370.1965 (2012), pp. 1850–1870 (cit. on p. 16).

[73] M.J. Pavier and M.P. Clarke. “Experimental techniques for the investigation of the effects of impact damage on carbon-fibre composites”. In: *Composites Science and Technology* 55.2 (1995), pp. 157 –169 (cit. on p. 16).

[74] D.D.R. Cartié and P.E. Irving. “Effect of resin and fibre properties on impact and compression after impact performance of CFRP”. In: *Composites Part A: Applied Science and Manufacturing* 33.4 (2002), pp. 483 –493 (cit. on pp. 20, 23, 29–31).

[75] G. A. Schoeppner and S. Abrate. “Delamination threshold loads for low velocity impact on composite laminates”. In: *Composites Part A: Applied Science and Manufacturing* 31.9 (2000), pp. 903–915 (cit. on p. 20).

[76] Puhui Chen, Zhen Shen, Junjie Xiong, et al. “Failure mechanisms of laminated composites subjected to static indentation”. In: *Composite Structures* 75.1–4 (2006). Thirteenth International Conference on Composite StructuresICCS/13Thirteenth International Conference on Composite Structures, pp. 489 –495 (cit. on p. 20).

[77] Y. Xiong, C. Poon, P.V. Straznicky, and H. Vietinghoff. “A prediction method for the compressive strength of impact damaged composite laminates”. In: *Composite Structures* 30.4 (1995), pp. 357 –367 (cit. on p. 25).

[78] Sergei Georgievich Lekhnitskii. *Anisotropic plates*. Tech. rep. DTIC Document, 1968 (cit. on p. 25).

[79] J.M. Whitney and R.J. Nuismer. “Stress Fracture Criteria for Laminated Composites Containing Stress Concentrations”. In: *Journal of Composite Materials* 8.3 (1974), pp. 253–265 (cit. on p. 25).

[80] B. Qi and I. Herszberg. “An engineering approach for predicting residual strength of carbon/epoxy laminates after impact and hygrothermal cycling”. In: *Composite Structures* 47.1–4 (1999). Tenth International Conference on Composite Structures, pp. 483 –490 (cit. on p. 25).

[81] O.A Khondker, I Herszberg, and H Hamada. “Measurements and prediction of the compression-after-impact strength of glass knitted textile composites”. In: *Composites Part A: Applied Science and Manufacturing* 35.2 (2004), pp. 145 –157 (cit. on pp. 25, 26).

[82] Puhui Chen, Zhen Shen, and Jun Yang Wang. “Prediction of the strength of notched fiber-dominated composite laminates”. In: *Composites Science and Technology* 61.9 (2001), pp. 1311 –1321 (cit. on p. 26).

[83] Bokwon Lee and Bhavani V. Sankar. “Lay-up independent fracture criterion for notched laminated composites”. In: *Composites Science and Technology* 66.14 (2006). Special Issue in Honour of Professor C.T. Sun, pp. 2491 –2499 (cit. on p. 26).

[84] J.C. Prichard and P.J. Hogg. “The role of impact damage in post-impact compression testing”. In: *Composites* 21.6 (1990), pp. 503 –511 (cit. on pp. 26, 31).

[85] Jerry G. Williams, Melvin S. Anderson, Marvin D. Rhodes, James H. Starnes, and W. Jefferson Stroud. “Recent Developments in the Design, Testing and Impact-Damage Tolerance of Stiffened Composite Panels”. In: *Fibrous Composites in Structural Design*. Ed. by Edward M. Lenoe, Donald W. Oplinger, and John J. Burke. Boston, MA: Springer US, 1980, pp. 259–291 (cit. on p. 27).

[86] Emile Greenhalgh and Matthew Hiley. “The assessment of novel materials and processes for the impact tolerant design of stiffened composite aerospace structures”. In: *Composites Part A: Applied Science and Manufacturing* 34.2 (2003), pp. 151 –161 (cit. on p. 27).

[87] Youhong Tang, Lin Ye, Zhong Zhang, and Klaus Friedrich. “Interlaminar fracture toughness and CAI strength of fibre-reinforced composites with nanoparticles – A review”. In: *Composites Science and Technology* 86 (2013), pp. 26 –37 (cit. on p. 27).

[88] N.H. Nash, T.M. Young, P.T. McGrail, and W.F. Stanley. “Inclusion of a thermoplastic phase to improve impact and post-impact performances of carbon fibre reinforced thermosetting composites — A review”. In: *Materials & Design* 85 (2015), pp. 582 –597 (cit. on p. 27).

[89] Dodd H Grande, Larry B Ilcewicz, William B Avery, and Willard D Bascom. "Effects of intra-and inter-laminar resin content on the mechanical properties of toughened composite materials". In: (1991) (cit. on p. 31).

[90] Takashi Ishikawa, Sunao Sugimoto, Masamichi Matsushima, and Yoichi Hayashi. "Some experimental findings in compression-after-impact (CAI) tests of CF/PEEK (APC-2) and conventional CF/epoxy flat plates". In: *Composites Science and Technology* 55.4 (1995), pp. 349 –363 (cit. on p. 31).

[91] R. Butler, D.P. Almond, G.W. Hunt, B. Hu, and N. Gathercole. "Compressive fatigue limit of impact damaged composite laminates". In: *Composites Part A: Applied Science and Manufacturing* 38.4 (2007). Selected Papers from the Joint 8th International Conference on Deformation and Fracture of Composites (DFC-8) and Experimental Techniques and Design in Composite Materials (ETDCM-7) held at the University of Sheffield, UK, pp. 1211 –1215 (cit. on pp. 32, 33, 117).

[92] Andrew T. Rhead, Richard Butler, and Giles W. Hunt. "Post-buckled propagation model for compressive fatigue of impact damaged laminates". In: *International Journal of Solids and Structures* 45.16 (2008), pp. 4349 –4361 (cit. on pp. 32, 33).

[93] Andrew T. Rhead and Richard Butler. "Compressive static strength model for impact damaged laminates". In: *Composites Science and Technology* 69.14 (2009). The Sixteenth International Conference on Composite Materials with Regular Papers, pp. 2301 –2307 (cit. on pp. 32–34).

[94] Neil Baker and Richard Butler. "Compression after impact modeling of damage tolerant composite laminates". In: *51st AIAA/ASME/ASCE/AHS/ASC Structures, Structural Dynamics, and Materials Conference 18th AIAA/ASME/AHS Adaptive Structures Conference 12th*. 2010, p. 2868 (cit. on pp. 32, 33, 117).

[95] Andrew T Rhead, Richard Butler, and Neil Baker. "Analysis and compression testing of laminates optimised for damage tolerance". In: *Applied Composite Materials* 18.1 (2011), pp. 85–100 (cit. on pp. 32, 33, 35, 110, 117).

[96] Richard Butler, Andrew T. Rhead, Wenli Liu, and Nikolaos Kontis. "Compressive strength of delaminated aerospace composites". In: 370.1965 (2012), pp. 1759–1779 (cit. on p. 32).

[97] Herzl Chai, Charles D. Babcock, and Wolfgang G. Knauss. "One dimensional modelling of failure in laminated plates by delamination buckling". In: *International Journal of Solids and Structures* 17.11 (1981), pp. 1069 –1083 (cit. on pp. 32, 44).

[98] J. G. Williams. "On the calculation of energy release rates for cracked laminates". In: *International Journal of Fracture* 36.2 (1988), pp. 101–119 (cit. on p. 32).

[99] J.W. Hutchinson and Z. Suo. "Mixed Mode Cracking in Layered Materials". In: *Advances in Applied Mechanics*. Ed. by John W. Hutchinson and Theodore Y. Wu. Vol. 29. Advances in Applied Mechanics. Elsevier, 1991, pp. 63 –191 (cit. on p. 32).

[100] Shun-Fa Hwang and Guu-Huann Liu. "Buckling behavior of composite laminates with multiple delaminations under uniaxial compression". In: *Composite Structures* 53.2 (2001), pp. 235 –243 (cit. on pp. 32, 34, 42, 43, 46).

[101] L.Gunnar Melin and Joakim Schön. "Buckling behaviour and delamination growth in impacted composite specimens under fatigue load: an experimental study". In: *Composites Science and Technology* 61.13 (2001), pp. 1841 –1852 (cit. on pp. 32, 34).

[102]F. W. Williams, M. S. Anderson, D. Kennedy, R. Butler, and G. Aston. *User manual for VICONOPT: An exact analysis and optimum design program covering the buckling and vibration of prismatic assemblies of flat in-plane loaded, anisotropic plates, with approximations for discrete supports, and transverse stiffeners*. Tech. rep. NASA, 1990 (cit. on p. 32).

[103]Neil Baker, Richard Butler, and Christopher B. York. "Damage tolerance of fully orthotropic laminates in compression". In: *Composites Science and Technology* 72.10 (2012), pp. 1083 –1089 (cit. on p. 33).

[104]X. Zhang, L. Hounslow, and M. Grassi. "Improvement of low-velocity impact and compression-after-impact performance by z-fibre pinning". In: *Composites Science and Technology* 66.15 (2006), pp. 2785 –2794 (cit. on p. 35).

[105]A.P. Mouritz and B.N. Cox. "A mechanistic interpretation of the comparative in-plane mechanical properties of 3D woven, stitched and pinned composites". In: *Composites Part A: Applied Science and Manufacturing* 41.6 (2010), pp. 709 –728 (cit. on p. 35).

[106]K.T. Tan, N. Watanabe, Y. Iwahori, and T. Ishikawa. "Effect of stitch density and stitch thread thickness on compression after impact strength and response of stitched composites". In: *Composites Science and Technology* 72.5 (2012), pp. 587 –598 (cit. on p. 35).

[107]Gary L. Farley, Barry T. Smith, and Janice Maiden. "Compression Response of Thick Layer Composite Laminates with Through-the-Thickness Reinforcement". In: *Journal of Reinforced Plastics and Composites* 11.7 (1992), pp. 787–810 (cit. on p. 35).

[108]Gary L. Farley and Larry C. Dickinson. "Removal of Surface Loop from Stitched Composites Can Improve Compression and Compression-after-Impact Strengths". In: *Journal of Reinforced Plastics and Composites* 11.6 (1992), pp. 633–642 (cit. on p. 35).

[109]Cheng Xiaoquan, Ali M. Al-Mansour, Li Zhengneng, and Kou Chenghe. "Compression Strength of Stitched Laminates after Low-velocity Impact". In: *Journal of Reinforced Plastics and Composites* 24.9 (2005), pp. 935–947 (cit. on p. 35).

[110]Joon-Hyung Byun, Sung-Wook Song, Chang-Hoon Lee, Moon-Kwang Um, and Byung-Sun Hwang. "Impact properties of laminated composites with stitching fibers". In: *Composite Structures* 76.1–2 (2006). Fifteenth International Conference on Composite MaterialsICCM-15Fifteenth International Conference on Composite Materials, pp. 21 –27 (cit. on p. 35).

[111]P Mattheij, K Gliesche, and D Feltin. "3D reinforced stitched carbon/epoxy laminates made by tailored fibre placement". In: *Composites Part A: Applied Science and Manufacturing* 31.6 (2000), pp. 571 –581 (cit. on p. 35).

[112]Uwe Beier, Frank Fischer, Jan K.W. Sandler, et al. "Mechanical performance of carbon fibre-reinforced composites based on stitched preforms". In: *Composites Part A: Applied Science and Manufacturing* 38.7 (2007), pp. 1655 –1663 (cit. on p. 35).

[113]Uwe Beier, Felipe Wolff-Fabris, Frank Fischer, et al. "Mechanical performance of carbon fibre-reinforced composites based on preforms stitched with innovative low-melting temperature and matrix soluble thermoplastic yarns". In: *Composites Part A: Applied Science and Manufacturing* 39.9 (2008), pp. 1572 –1581 (cit. on p. 35).

[114] Uwe Beier, Jan K.W. Sandler, Volker Altstädt, Hermann Spanner, and Christian Weimer. "Mechanical performance of carbon fibre-reinforced composites based on stitched and bindered preforms". In: *Composites Part A: Applied Science and Manufacturing* 40.11 (2009), pp. 1756 –1763 (cit. on p. 35).

[115] W.J. Cantwell, P.T. Curtis, and J. Morton. "An assessment of the impact performance of CFRP reinforced with high-strain carbon fibres". In: *Composites Science and Technology* 25.2 (1986), pp. 133 –148 (cit. on p. 35).

[116] Andrew T. Rhead, Shi Hua, and Richard Butler. "Damage resistance and damage tolerance of hybrid carbon-glass laminates". In: *Composites Part A: Applied Science and Manufacturing* 76 (2015), pp. 224 –232 (cit. on p. 35).

[117] S.A. Hitchen and R.M.J. Kemp. "Development of novel cost effective hybrid ply carbon-fibre composites". In: *Composites Science and Technology* 56.9 (1996), pp. 1047 –1054 (cit. on p. 35).

[118] E.V. González, P. Maimí, J.R. Sainz de Aja, P. Cruz, and P.P. Camanho. "Effects of interply hybridization on the damage resistance and tolerance of composite laminates". In: *Composite Structures* 108 (2014), pp. 319 –331 (cit. on p. 35).

[119] Marcel Siegfried, Carmen Tola, Michael Claes, et al. "Impact and residual after impact properties of carbon fiber/epoxy composites modified with carbon nanotubes". In: *Composite Structures* 111 (2014), pp. 488 –496 (cit. on p. 36).

[120] V. Kostopoulos, A. Baltopoulos, P. Karapappas, A. Vavouliotis, and A. Paipetis. "Impact and after-impact properties of carbon fibre reinforced composites enhanced with multi-wall carbon nanotubes". In: *Composites Science and Technology* 70.4 (2010), pp. 553 –563 (cit. on p. 36).

[121] Hiroshi Saito, Mitsuhiro Morita, Kazumasa Kawabe, et al. "Effect of ply-thickness on impact damage morphology in CFRP laminates". In: 30.13 (2011), pp. 1097–1106 (cit. on pp. 36, 117).

[122] T.A. Sebaey and E. Mahdi. "Using thin-plies to improve the damage resistance and tolerance of aeronautical CFRP composites". In: *Composites Part A: Applied Science and Manufacturing* 86 (2016), pp. 31 –38 (cit. on p. 36).

[123] Xinguang Xu, Zhenggang Zhou, Yanwei Hei, et al. "Improving compression-after-impact performance of carbon–fiber composites by CNTs/thermoplastic hybrid film interlayer". In: *Composites Science and Technology* 95.Supplement C (2014), pp. 75 –81 (cit. on p. 36).

[124] S.M. García-Rodríguez, J. Costa, V. Singery, I. Boada, and J.A. Mayugo. "The effect interleaving has on thin-ply non-crimp fabric laminate impact response: X-ray tomography investigation". In: *Composites Part A: Applied Science and Manufacturing* xxxxx.xxxxx (2017). Under Review, p. xxxxx (cit. on p. 36).

[125] Innocent Kafodya, Guijun Xian, and Hui Li. "Durability study of pultruded CFRP plates immersed in water and seawater under sustained bending: Water uptake and effects on the mechanical properties". In: *Composites Part B: Engineering* 70 (2015), pp. 138 –148 (cit. on p. 37).

[126]Krystyna Imielińska and Laurent Guillaumat. “The effect of water immersion ageing on low-velocity impact behaviour of woven aramid–glass fibre/epoxy composites”. In: *Composites Science and Technology* 64.13–14 (2004), pp. 2271 –2278 (cit. on pp. 37, 86, 106).

[127]Yuichiro Aoki, Ken Yamada, and Takashi Ishikawa. “Effect of hygrothermal condition on compression after impact strength of CFRP laminates”. In: *Composites Science and Technology* 68.6 (2008), pp. 1376–1383 (cit. on pp. 37, 85, 86, 106).

[128]Yucheng Zhong and Sunil Chandrakant Joshi. “t of”. In: *Materials and Design* 65 (2015), pp. 254 –264 (cit. on pp. 37, 85).

[129]R. Craven, L. Iannucci, and R. Olsson. “Delamination buckling: A finite element study with realistic delamination shapes, multiple delaminations and fibre fracture cracks”. In: *Composites Part A: Applied Science and Manufacturing* 41.5 (2010), pp. 684 –692 (cit. on pp. 37, 46).

[130]Vít Obdržalék. “Simulation of interlaminar and intralaminar damage in polymer-based composites for aeronautical applcations under impact loading”. PhD thesis. Brno University of Technology, 2010 (cit. on pp. 40, 41).

[131]Jaehong Lee, Zafer Gurdal, and OH GRIFFIN JR. “Layer-wise approach for the bifurcation problem in laminated composites with delaminations”. In: *AIAA journal* 31.2 (1993), pp. 331–338 (cit. on pp. 41, 43, 46).

[132]Meng-Kao Yeh and Chung-Ming Tan. “Buckling of Elliptically Delaminated Composite Plates”. In: *Journal of Composite Materials* 28.1 (1994), pp. 36–52 (cit. on pp. 41, 42).

[133]Shun-Fa Hwang and Ching-Ping Mao. “The delamination buckling of single-fibre system and interply hybrid composites”. In: *Composite Structures* 46.3 (1999), pp. 279 –287 (cit. on p. 41).

[134]Ning Hu, Hisao Fukunaga, Hideki Sekine, and Kouchakzadeh Mohammad Ali. “Compressive buckling of laminates with an embedded delamination”. In: *Composites Science and Technology* 59.8 (1999), pp. 1247 –1260 (cit. on pp. 41, 42, 117).

[135]P. Gaudenzi, P. Perugini, and A. Riccio. “Post-buckling behavior of composite panels in the presence of unstable delaminations”. In: *Composite Structures* 51.3 (2001), pp. 301 –309 (cit. on pp. 41, 45).

[136]V. Obdržálek and J. Vrbka. “On buckling of a plate with mulitple delaminations”. In: *Engineering Mechanics* 17.1 (2010), pp. 37 –47 (cit. on pp. 41, 42).

[137]H. Hosseini-Toudeshky, S. Hosseini, and B. Mohammadi. “Buckling and Delamination Growth Analysis of Composite Laminates Containing Embedded Delaminations”. In: *Applied Composite Materials* 17.2 (2010), pp. 95–109 (cit. on pp. 41, 43).

[138]V. Obdržálek and J. Vrbka. “On the applicability of simple shapes of delaminations in buckling analyses”. In: *Composites Part B: Engineering* 42.3 (2011), pp. 538 –545 (cit. on pp. 41, 42, 45).

[139]Azam Tafreshi and Tobias Oswald. “Global buckling behaviour and local damage propagation in composite plates with embedded delaminations”. In: *International Journal of Pressure Vessels and Piping* 80.1 (2003), pp. 9 –20 (cit. on pp. 42, 43, 45, 117).

[140] Shun-Fa Hwang and Guu-Huann Liu. “Experimental Study for Buckling and Postbuckling Behaviors of Composite Laminates with Multiple Delaminations”. In: *Journal of Reinforced Plastics and Composites* 21.4 (2002), pp. 333–349 (cit. on pp. 42, 46).

[141] Dae-Yong Park and Sang-Youl Lee. “Parametric effects on embedded delamination buckling in composite structures using the EAS three-dimensional element”. In: *Composites Part B: Engineering* 43.4 (2012), pp. 1800 –1812 (cit. on p. 42).

[142] Bijan Mohammadi and Farhad Shahabi. “On computational modeling of postbuckling behavior of composite laminates containing single and multiple through-the-width delaminations using interface elements with cohesive law”. In: *Engineering Fracture Mechanics* 152 (2016), pp. 88 –104 (cit. on pp. 43, 45).

[143] John D Whitcomb. “Finite element analysis of instability related delamination growth”. In: *Journal of Composite Materials* 15.5 (1981), pp. 403–426 (cit. on p. 44).

[144] John D Whitcomb. *Analysis of instability-related growth of a through-width delamination*. Tech. rep. NASA, 1984 (cit. on p. 44).

[145] Herzl Chai and Charles D. Babcock. “Two-Dimensional Modelling of Compressive Failure in Delaminated Laminates”. In: *Journal of Composite Materials* 19.1 (1985), pp. 67–98 (cit. on p. 44).

[146] John D. Whitcomb and K.N. Shivakumar. “Strain-Energy Release Rate Analysis of Plates with Postbuckled Delaminations”. In: *Journal of Composite Materials* 23.7 (1989), pp. 714–734 (cit. on p. 44).

[147] John D. Whitcomb. “Three-Dimensional Analysis of a Postbuckled Embedded Delamination”. In: *Journal of Composite Materials* 23.9 (1989), pp. 862–889 (cit. on p. 44).

[148] John D. Whitcomb. “Analysis of a Laminate with a Postbuckled Embedded Delamination, Including Contact Effects”. In: *Journal of Composite Materials* 26.10 (1992), pp. 1523–1535 (cit. on pp. 44, 45).

[149] Jaehong Lee, O.H. Griffin, and Z. Gürdal. “Buckling and postbuckling of circular plates containing concentric penny-shaped delaminations”. In: *Computers & Structures* 56.6 (1995), pp. 1053 –1063 (cit. on p. 45).

[150] A. Riccio, P. Perugini, and F. Scaramuzzino. “Modelling compression behaviour of delaminated composite panels”. In: *Computers & Structures* 78.1–3 (2000), pp. 73 –81 (cit. on p. 45).

[151] Y. Zhang and S. Wang. “Buckling, post-buckling and delamination propagation in debonded composite laminates: Part 1: Theoretical development”. In: *Composite Structures* 88.1 (2009), pp. 121 –130 (cit. on p. 45).

[152] S. Wang and Y. Zhang. “Buckling, post-buckling and delamination propagation in debonded composite laminates Part 2: Numerical applications”. In: *Composite Structures* 88.1 (2009), pp. 131 –146 (cit. on p. 45).

[153] Zafer Kutlu and Fu-Kuo Chang. “Composite panels containing multiple through-the-width delaminations and subjected to compression. Part I: Analysis”. In: *Composite Structures* 31.4 (1995), pp. 273 –296 (cit. on p. 45).

[154] Zafer Kutlu and Fu-Kuo Chang. “Composite panels containing multiple through-the-width delaminations and subjected to compression. Part II: Experiments & verification”. In: *Composite Structures* 31.4 (1995), pp. 297 –314 (cit. on p. 45).

[155] Y.J Lee, C.H. Lee, and W.S. Fu. “Study on the compressive strength of laminated composite with through-the-width delamination”. In: *Composite Structures* 41.3 (1998), pp. 229 –241 (cit. on p. 45).

[156] Aniello Riccio and Elisa Pietropaoli. “Modeling Damage Propagation in Composite Plates with Embedded Delamination under Compressive Load”. In: *Journal of Composite Materials* 42.13 (2008), pp. 1309–1335 (cit. on p. 45).

[157] Woo-Min Kyoung, Chun-Gon Kim, and Chang-Sun Hong. “Buckling and postbuckling behavior of composite cross-ply laminates with multiple delaminations”. In: *Composite Structures* 43.4 (1998), pp. 257 –274 (cit. on p. 46).

[158] Shun-Fa Hwang and Shu-Mei Huang. “Postbuckling behavior of composite laminates with two delaminations under uniaxial compression”. In: *Composite Structures* 68.2 (2005), pp. 157 –165 (cit. on p. 46).

[159] Züleyha Aslan and Mustafa Şahin. “Buckling behavior and compressive failure of composite laminates containing multiple large delaminations”. In: *Composite Structures* 89.3 (2009), pp. 382 –390 (cit. on p. 46).

[160] Züleyha Aslan and Fatih Daricik. “Effects of multiple delaminations on the compressive, tensile, flexural, and buckling behaviour of E-glass/epoxy composites”. In: *Composites Part B: Engineering* 100 (2016), pp. 186 –196 (cit. on p. 46).

[161] Hiroshi Suemasu, Wataru Sasaki, Yuuichiro Aoki, and Takashi Ishikawa. “Compressive behavior of impact damaged composite laminates”. In: *In Proc. 16th Int. Conf. on Composite Materials, Kyoto, Japan 8â 13 July 2007*. 2007 (cit. on p. 46).

[162] M.J. Pavier and M.P Clarke. “Finite element prediction of the post-impact compressive strength of fibre composites”. In: *Composite Structures* 36.1 (1996), pp. 141 –153 (cit. on p. 46).

[163] L. Marín, E.V. González, P. Maimí, D. Trias, and P.P. Camanho. “Hygrothermal effects on the translaminar fracture toughness of cross-ply carbon/epoxy laminates: Failure mechanisms”. In: *Composites Science and Technology* 122 (2016), pp. 130 –139 (cit. on p. 51).

[164] *Standard Test Method for Measuring the Damage Resistance of a Fiber-Reinforced Polymer Matrix Composite to a Drop-Weight Impact Event*. Standard. 2012 (cit. on pp. 52, 53, 55, 62, 73, 82).

[165] A. Wagih, P. Maimí, E.V. González, et al. “Damage sequence in thin-ply composite laminates under out-of-plane loading”. In: *Composites Part A: Applied Science and Manufacturing* 87 (2016), pp. 66 –77 (cit. on pp. 53, 55).

[166] *Standard Test Method for Compressive Residual Strength Properties of Damaged Polymer Matrix Composite Plates*. Standard. 2012 (cit. on pp. 56, 62).

[167] T.A Sebaey. “Characterization and optimization of dispersed composite laminates for damage resistant aeronautical structures”. PhD thesis. Universitat de Girona, 2012 (cit. on p. 57).

[168] *Aerospace series–Fibre reinforced plastics–Determination of the effect of exposure to humid atmosphere on physical and mechanical characteristics*. Standard. 1998 (cit. on p. 61).

[169] James R Reeder, Kyongchan Song, Prasad Chunchu, and Damodar R Ambur. "Postbuckling and growth of delaminations in composite plates subjected to axial compression". In: *The 43rd AIAA/ASME/ASCE/AHS/ASC Structures, Structural Dynamics, and Materials Conference*. 2002 (cit. on pp. 66–68, 125).

[170] Andrew T. Rhead and Richard Butler. "Compressive static strength model for impact damaged laminates". In: *Composites Science and Technology* 69.14 (2009). The Sixteenth International Conference on Composite Materials with Regular Papers, pp. 2301–2307 (cit. on p. 73).

[171] Andrew T. Rhead, Richard Butler, and Neil Baker. "Analysis and Compression Testing of Laminates Optimised for Damage Tolerance". English. In: *Applied Composite Materials* 18.1 (2011), pp. 85–100 (cit. on p. 73).

[172] T. A. Sebaey, E. V. González, C. S. Lopes, N. Blanco, and J. Costa. "Damage resistance and damage tolerance of dispersed CFRP laminates: The bending stiffness effect". In: *Composite Structures* 106.0 (2013), pp. 30–32 (cit. on p. 75).

[173] Robin Olsson. "Analytical prediction of large mass impact damage in composite laminates". In: *Composites Part A: Applied Science and Manufacturing* 32.9 (2001), pp. 1207–1215 (cit. on p. 75).

[174] P. Berbinau, C. Soutis, P. Goutas, and P. T. Curtis. "Effect of off-axis ply orientation on 0°-fibre microbuckling". In: *Composites Part A: Applied Science and Manufacturing* 30.10 (1999), pp. 1197 –1207 (cit. on p. 85).

[175] A. Kabiri Ataabadi, H. Hosseini-Toudeshky, and S. Ziaei Rad. "Experimental and analytical study on fiber-kinking failure mode of laminated composites". In: *Composites Part B: Engineering* 61 (2014), pp. 84 –93 (cit. on p. 85).

[176] Pedro P. Camanho, Carlos G. Dávila, Silvestre T. Pinho, Lorenzo Iannucci, and Paul Robinson. "Prediction of in situ strengths and matrix cracking in composites under transverse tension and in-plane shear". In: *Composites Part A: Applied Science and Manufacturing* 37.2 (2006). CompTest 2004, pp. 165–176 (cit. on p. 85).

[177] T. A. Sebaey, J. Costa, P. Maimí, et al. "Measurement of the in situ transverse tensile strength of composite plies by means of the real time monitoring of microcracking". In: *Composites Part B: Engineering* 65.0 (2014). Damage Mechanics, pp. 40–46 (cit. on pp. 85, 107).

[178] Wenqiong Tu and Marek-Jerzy Pindera. "Damage evolution in cross-ply laminates revisited via cohesive zone model and finite-volume homogenization". In: *Composites Part B: Engineering* 86 (2016), pp. 40 –60 (cit. on p. 85).

[179] N. Jagannathan, S. Gururaja, and C.M. Manjunatha. "Probabilistic strength based matrix crack evolution in multi-directional composite laminates". In: *Composites Part B: Engineering* 87 (2016), pp. 263 –273 (cit. on p. 85).

[180] I.G. García, B.J. Carter, A.R. Ingraffea, and V. Mantič. "A numerical study of transverse cracking in cross-ply laminates by 3D finite fracture mechanics". In: *Composites Part B: Engineering* 95 (2016), pp. 475 –487 (cit. on p. 85).

[181]Earnest F. Dost, Larry B. Ilcewicz, William B. Avery, and Brian R. Coxon. “Effects of Stacking Sequence on Impact Damage Resistance and Residual Strength for Quasi-Isotropic Laminates”. In: *Composite materials: Fatigue and fracture. Vol. 3 (A92-39001 16-39)*. Ed. by O’Brien T K. Philadelphia, PA, American Society for Testing and Materials: ASTM, 1991, pp. 476–500 (cit. on p. 85).

[182]Perttu Hintikka, Markus Wallin, and Olli Saarela. “The effect of moisture on the interlaminar fracture toughness of CFRP laminate”. In: *27th International Congress of the Aeronautical Sciences. Nice, France. 19-24 September*. 2010, pp. 1–8 (cit. on pp. 85, 106).

[183]E. Abisset, F. Daghia, X.C. Sun, M.R. Wisnom, and S.R. Hallett. “Interaction of inter- and intralaminar damage in scaled quasi-static indentation tests: Part 1 – Experiments”. In: *Composite Structures* 136 (2016), pp. 712 –726 (cit. on p. 103).

[184]Hiroshi Suemasu and Osamu Majima. “Multiple Delaminations and their Severity in Circular Axisymmetric Plates Subjected to Transverse Loading”. In: *Journal of Composite Materials* 30.4 (1996), pp. 441–453 (cit. on p. 105).

[185]Tomohiro Yokozeki, Takahira Aoki, Toshio Ogasawara, and Takashi Ishikawa. “Effects of layup angle and ply thickness on matrix crack interaction in contiguous plies of composite laminates”. In: *Composites Part A: Applied Science and Manufacturing* 36.9 (2005), pp. 1229 –1235 (cit. on p. 105).

[186]S. Zheng and C.T. Sun. “Delamination interaction in laminated structures”. In: *Engineering Fracture Mechanics* 59.2 (1998), pp. 225 –240 (cit. on pp. 105, 106).

[187]L. Zubillaga, A. Turon, J. Renart, J. Costa, and P. Linde. “An experimental study on matrix crack induced delamination in composite laminates”. In: *Composite Structures* 127 (2015), pp. 10 –17 (cit. on p. 106).

[188]Robin Olsson, Mauricio V. Donadon, and Brian G. Falzon. “Delamination threshold load for dynamic impact on plates”. In: *International Journal of Solids and Structures* 43.10 (2006), pp. 3124 –3141 (cit. on p. 106).

[189]A.J. Smiley and R.B. Pipes. “Rate Effects on Mode I Interlaminar Fracture Toughness in Composite Materials”. In: *Journal of Composite Materials* 21.7 (1987), pp. 670–687 (cit. on p. 107).

[190]A.J. Smiley and R.B. Pipes. “Rate sensitivity of mode II interlaminar fracture toughness in graphite/epoxy and graphite/PEEK composite materials”. In: *Composites Science and Technology* 29.1 (1987), pp. 1 –15 (cit. on p. 107).

[191]S.A. Laman, M.R. Groleau, and M. Vedula. “Use of Controlled Interply Delaminations to Study the Damage Tolerance of Composites”. In: *24th Int. SAMPE Technical Conf*. 1992, 821–833 (cit. on p. 116).

[192]Giles W Hunt, Beilei Hu, Richard Butler, Darryl P Almond, and JE Wright. “Nonlinear modeling of delaminated struts”. In: *AIAA journal* 42.11 (2004), pp. 2364–2372 (cit. on p. 117).